ORNL-TM-1270

Contract No. W-7405-eng-26

FUELS AND MATERIALS DEVELOPMENT PROGRAM QUARTERLY PROGRESS REPORT FOR PERIOD ENDING SEPTEMBER 30, 1965

Compiled by

P. Patriarca

UNCLASSIFIED

DECEMBER 1965

OAK RIDGE NATIONAL LABORATORY
Oak Ridge, Tennessee
operated by
UNION CARBIDE CORPORATION
for the
U. S. ATOMIC ENERGY COMMISSION

DISCLAIMER

FOREWORD

This is the sixth quarterly progress report describing work performed at the Oak Ridge National Laboratory for the Fuels and Materials Branch, Division of Reactor Development and Technology, U. S. Atomic Energy Commission. The specific programs covered are as follows:

Part I. Metals and Ceramics Division

Program Title	Person in Charge	Principal Investigator(s)
Controlled Precipitation in Nuclear Materials	W. O. Harms	J. L. Scott J. P. Hammond
Fuel Element Development	G. M. Adamson, Jr.	C. F. Leitten, Jr.
Nondestructive Test Development	D. A. Douglas, Jr.	R. W. McClung
Zirconium Metallurgy	C. J. McHargue	M. L. Picklesimer

Part II. Reactor Chemistry Division

Fission-Gas Release and Physical Properties of Fuel Materials During Irradiation	O. Sisman	R. M. Carroll M. F. Osborne

Part III. Solid State Division

Irradiation Effects on Alloys and Structural Materials	D. S. Billington	M. S. Wechsler

TABLE OF CONTENTS

SUMMARY

1. Controlled Precipitation in Nuclear Materials

This program has been expanded to include studies on property enhancement by controlled precipitation in metal-base as well as in ceramic systems.

Titanium-doped Al_2O_3 single crystals were prepared by flame-fusion growth using mixed powders as feed material and by diffusion of titanium into pure Al_2O_3 crystals at 1700°C in hydrogen. Conditions were established for growth of crack-free crystals containing 0.1 wt % TiO_2. As-grown crystals exhibit a characteristic blue color indicating the presence of Ti^{3+}. After annealing in air at 1700°C, the crystals become colorless and precipitation occurs on slow cooling or after quenching and aging at 1300°C in air.

Aluminum alloys supersaturated with 2 to 3 at. % of cerium, yttrium, or beryllium were obtained for subsequent fabrication and heat treatment to produce dispersion-hardened alloys with improved mechanical properties through controlled precipitation of stable intermetallic phases. A similar technique for dispersion strengthening of thorium metal using powders supersaturated with respect to beryllium was investigated. Additional work on strengthening of thorium has included internal boronation of thorium-zirconium alloys prepared by two processes to form stable precipitates of ZrB_2.

2. Fuel Element Development

During this period, our original conversion studies on UF_6 to UO_2 were expanded to included the conversion of UCl_4 to UO_2 as well as the direct synthesis of other uranium compounds from UF_6 gas by a vapor-phase lithium reduction.

Both these later conversion schemes were proven thermodynamically feasible. Our investigations show that UCl_4 can be directly converted to uranium oxide as both a solid deposit or as fine powder depending on the

reduction parameters. Cursory experiments on the reduction of UF_6 by lithium have yielded encouraging results which indicate that compounds such as UC and UN may be synthesized directly from gaseous UF_6.

Refractory-metal cladding materials have been fabricated by the coreduction of tungsten and rhenium hexafluoride by hydrogen to produce tungsten-rhenium alloys over a wide range of composition. We have again continued investigating means of producing uniform homogeneity in these alloy depositions. Using a large deposition chamber, we recently deposited smooth-wall, homogeneous tubing of the W–25% Re alloy. The deposits were approximately 8 in. long.

3. Nondestructive Test Development

We are developing new techniques and equipment for the nondestructive evaluation of materials and components. The major emphasis has been on eddy-current, ultrasonic, and penetrating-radiation methods.

The mathematical approach using a computer to analyze variations in electromagnetic field parameters has been applied to the calculation of coil impedance. A prototype beat-frequency instrument has been developed for measurement of electrical conductivity.

The ultrasonic program has continued to work on techniques for nonbond evaluation in hot cells on tubular fuel elements. Tantalum has been tested as a tool for electro-discharge machining of reference notches. A new ultrasonic probe has been developed which combines advantages of both contact and immersion testing.

We have continued our scintillation gaging work with further calibration on our fuel rod scanner and beginning work on the use of light pipes for coupling scintillation crystals to photomultiplier tubes. A single-channel, gamma-scintillation spectrometer has been assembled and is being calibrated for ^{235}U assay in core blanks.

4. Zirconium Metallurgy

Additional studies of stress orientation of hydrides in Zircaloy-2 have included the effects of thermal cycling under elastic stress to as

many as 20 cycles. Only small changes in hydride orientation with number of thermal cycles have been observed. Additional specimens are being examined for confirmation.

Yield strengths and strain anisotropy constants are being determined in compression on all available lots of Zircaloy-2, representing some 20 different textures. Tensile data have been collected and reported previously. The data will be used to attempt the development of an empirical correlation between yield strengths in tension and compression, strain anisotropy constants in tension and compression, and pole figure parameters. A preliminary correlation of strain anisotropy constants in tension and compression is presented.

The data collected in a study of strain behavior in Zircaloy-2 sheet-type tensile specimens having a very strong and known texture have been summarized. The data confirm our previous conclusion that suitable strain anisotropy constants for characterization of the three-dimensional anisotropy of Zircaloy-2 cannot be obtained from sheet-type specimens.

A method for rapid construction of ball models of crystallographic planes has been developed. It utilizes the flux of permanent magnets to hold ferromagnetic steel balls in place on plastic petri dishes. Models containing up to 5000 balls are quickly built. Defects of various kinds, including stacking faults and dislocations, are readily built into the model. A method of deforming such a defected model is being developed to examine the feasibility of observing atom movements when such defects move through the lattice. Twin models are also readily built and show graphically the strain present and the shuffling of atoms in the twin interface. The models permit a three-dimensional examination of the atom arrangements on various crystallographic planes that cannot be approached by any other technique.

A single crystal of zirconium has been compressed along the basal pole to examine the twins present and to permit checking of the several methods of determining twin and grain orientations in polycrystalline material. The new technique of orienting grains by polarized light

microscopy of a single surface has been proven by comparison with other accepted techniques.

Thermally formed oxide films on zirconium have been partially dissolved by vacuum annealing. The optical absorption observed in both the as-formed and vacuum-annealed thermal films is of the same kind as observed in partially dissolved, anodically formed films. This indicates that the defect structures are of the same kind.

Large grains have been grown in sponge zirconium and iodide zirconium strip by strain-annealing material having original grain sizes less than 10 μ in diameter. This method will provide another technique for growing large-grained stock of zirconium alloys.

New measurements of the oxidation patterns developed on single-crystal spheres of zirconium oxidized in air at 360 and 400°C have shown that the rates of oxidation can differ by a factor as large as 3 on crystallographic planes within a few degrees of each other. The oxidation furnace permits continuous examination of the specimen surface over at least one crystallographic triangle without disturbing the test.

An electropolishing solution has been found to attack the matrix zirconium around precipitated hydrides, but the attack is not believed to be due to local cell action. The same solution used at a lower voltage produces etch pits which are believed to be located at dislocations. The technique is not yet under sufficient control to provide quantitative data on dislocation densities.

5. Fission-Gas Release and Physical Properties of Fuel Materials During Irradiation

Thin-disk specimens of UO_2 are being irradiated for the purpose of developing a model for fission-gas release. In these experiments the specimen may be irradiated at different flux levels and independently controlled temperatures. Fission gas is removed by a sweep gas and the release rate from the UO_2 specimen is determined by sampling the sweep system.

The release rate of fission gas was observed to be temperature dependent above about 600°C and almost independent of temperature at

lower temperatures. According to classical theory this would correspond to a recoil release at low temperatures and a combination recoil-diffusion release at higher temperatures. However, we have found many results that could not be explained by, and which contradicted, classical theory. We have, therefore, postulated a new theory where the rate of escape of fission gas from UO_2 is controlled by the number of defect traps in the UO_2 structure. Defects are created by fission and may also be inherent flaws, such as grain boundaries and pores. Tests demonstrated that grain boundaries behaved as traps.

A mathematical model was developed for the steady-state mother-daughter migration with trapping. To fully evaluate the mathematical model, the experiment was modified to operate in a dynamic as well as a steady-state mode. By dynamic operation, we mean that either the fission rate or the temperature of the specimen is oscillated with a selected axis, frequency, and amplitude of oscillation. Only sine wave shapes have been used thus far.

6. Irradiation Effects on Alloys and Structural Materials

The two aspects of radiation damage to materials that are of interest to the Radiation Metallurgy Section of the Solid State Division at ORNL are the effects of radiation on diffusion-controlled reactions in alloys and on plastic deformation and fracture. The recent progress in these areas is described below. New facilities that have been installed or are being constructed and designed are also discussed.

Since many reactor materials are in a metastable state when they are inserted in service in radiation environments, it is important to determine how metallurgical processes are affected by the radiation. One such process under investigation is the precipitation of nitrides in alpha iron; low-frequency internal friction is used as a measure of the amount of nitrogen in solid solution. The rate of precipitation is enhanced by neutron irradiation, but not by electron irradiation. However, if the electron dose is large enough, some evidence for the trapping of nitrogen atoms by radiation-produced defects is seen.

Segregation is another type of metallurgical reaction that is being studied. A Ni–40 wt % Cu alloy was given a series of isothermal anneals following irradiation at −180°C to a dose of about 1×10^{17} neutrons/cm^2 (E > 1 Mev). The activation energy for the radiation-enhanced segregation reaction was found to increase during the process, although from 23 to 192°C the energy was fairly constant at 1.2 to 1.3 ev. For a singly activated process, this energy is shown to correspond to the energy for motion of the diffusion-enhancing defect.

Radiation hardening in iron is being investigated by stress relaxation techniques, which yield information concerning the stress dependence of dislocation velocity and the dislocation density. The stress dependence of dislocation velocity for electron and neutron irradiated iron was quite similar to that for unirradiated material. However, the threshold stress for macroscopic dislocation motion was increased significantly as a result of the irradiation. This factor, rather than the decrease in mobile dislocation density, was chiefly responsible for the radiation hardening in this material.

Measurements of the tensile properties of irradiated iron are also under way. One object of this work is to determine whether or not the changes in mechanical properties are affected by the rate at which the radiation exposure is applied (i.e. by the dose rate or instantaneous flux). This question has an important practical connotation since reactor pressure vessels are exposed to low-flux irradiations for long periods, whereas materials testing work is usually performed under high flux–short time conditions. No dose rate effect was observed for samples given a dose of 1.5×10^{18} neutrons/cm^2 (E > 2.9 Mev) over a range of fluxes and from 4 to 70×10^{11} neutrons cm^{-2} sec^{-1}. However, this is just an interim result, since irradiations that will greatly extend the range of fluxes are under way. Experiments on the strain rate dependence of the yield stress show that the yield stress asymptotically approaches the threshold stress (determined from stress relaxation experiments) as the strain rate is decreased.

Since the last reporting period, a study of plastic deformation in single crystals of niobium has been undertaken. Measurements of lattice

rotation during tensile deformation by direct x-ray determination have indicated a considerable amount of latent hardening on the secondary slip system. Also, the departure of the orientation of the tensile axis from that predicted for single slip was correlated with the appearance of the slip bands on the surface and an increased rate of work hardening. One neutron irradiation has been carried out, and characteristic changes in strength and ductility have been observed. In addition, efforts to reveal mobile dislocations in niobium by etch-pitting techniques have been successful. These techniques are now being applied to the direct measurement of dislocation velocities.

Smooth and notched sheet tensile samples of types 330 and 270 nickel and type 410 stainless steel have been irradiated to about 10^{21} neutrons/cm^2 in the ORR, and the results of two types of annealing experiments are described. For notched samples of type 330 nickel containing 0.03 wt % C, a large increase in strength was observed upon annealing to 427°C. A smaller increase in strength was also observed for smooth samples, but this irradiation-anneal hardening was not exhibited by any of the other alloys.

The status of the pressure vessel surveillance programs for the EGCR, SM-1, and HFIR reactors is given.

A number of additions and improvements in facilities have been made or are under way. The Charpy impact machine for use in the hot cells has been rebuilt to conform to AMRA and ASTM standards, and improvements in the remote temperature conditioning and positioning of samples have been made. Also, a new irradiation facility has been installed in the Bulk Shielding Reactor (BSR) and a number of flux measurements using Co, Np, U, Ni, and Fe have been carried out. The neutron spectrum was found to conform quite closely to a fission spectrum at energies between 0.6 and 2.9 Mev. The construction of a liquid-nitrogen-cooled cryostat for the BSR is now almost completed (not described in this report). Finally, the criticality study for a proposed neutron-converter, fission-flux, irradiation facility for the BSR has not revealed any undue safety hazard from the standpoint of criticality, and detailed engineering design work on the facility is about to begin.

PART I

METALS AND CERAMICS DIVISION

1. CONTROLLED PRECIPITATION IN NUCLEAR MATERIALS

J. L. Scott J. P. Hammond

This program was introduced in the previous report[1] and has been expanded to include studies on property enhancement by controlled precipitation in metal-base as well as in ceramic systems. The overall objective of the program remains the same, that is, to investigate means for improving the performance of both fissionable and nonfissionable materials by optimizing the microstructure through controlled precipitation of stable, dispersed phases.

Effect of Dispersed Precipitates on the Properties of Ceramic Materials

Precipitation Studies in Alumina — D. I. Matkin[2]

The objective of this study is to evaluate the effect of whisker-shaped precipitates on crack propagation in alumina. The immediate aim is to produce, by suitable heat treatment, a homogeneous distribution of precipitates in titanium-doped single crystals of Al_2O_3.

Difficulty has been encountered in obtaining single crystals of Al_2O_3 doped with titanium that are free of large defects. The doped crystals grown by flame fusion and obtained from a variety of sources have been observed to contain bubbles.[3] In view of this difficulty, attempts have been made to diffuse titanium into pure Al_2O_3 single crystals that are free of bubbles. The pure crystal specimens were placed in contact with titanium dioxide powder in a tungsten boat and

---

[1]W. O. Harms, Fuels and Materials Development Program Quart. Progr. Rept. June 30, 1965, ORNL-TM-1200, pp. 44–47.

[2]On loan from AERE, Harwell, England.

[3]D. I. Matkin, Fuels and Materials Development Program Quart Progr. Rept. June 30, 1965, ORNL-TM-1200, p. 45.

annealed at 1700°C in an atmosphere of hydrogen for several days. Laser "microprobe" spectrographic analysis indicated that titanium had diffused to a depth of several millimeters and to a concentration of approximately 500 ppm; however, the distribution was not homogeneous.

As-received titanium-doped Al_2O_3 crystals grown by flame fusion have a characteristic blue color, which apparently indicates the presence of Ti^{3+}. After annealing in air at 1700°C, the crystals become colorless and precipitation occurs if the crystals are cooled slowly, or if they are quenched and aged at 1300°C in air.

Growth of Titanium-Doped Al_2O_3 Single Crystals — D. I. Matkin,[2] J. Y. Chang,[4] G. W. Clark

Techniques were developed for growing titanium-doped Al_2O_3 single crystals by flame fusion. The flame fusion apparatus used is shown in Fig. 1.1. This apparatus features a multiple-tube burner[5] that was designed to give a more uniform mixture of oxygen and hydrogen, thereby increasing the temperature and reducing the temperature gradient across the diameter of the flame.

Initially the feed powder for growing doped crystals was prepared by dry blending Linde Al_2O_3 "boule" powder and Linde TiO_2 "boule" powder. However, with the small concentrations of TiO_2 involved, the mixture obtained was not homogeneous. The powders are now blended by slurry-mixing with ethyl alcohol, followed by drying and sieving.

The temperature of the furnace is reduced gradually at the end of a growth run to prevent the cracking of the boule upon cooling due to internal stresses. It is necessary to further stress relieve a crystal that has been carefully cooled to room temperature by annealing in air at temperatures in excess of 1700°C.

Optimum growth conditions were established for growing pure Al_2O_3 crystals and then, using slightly different conditions, Al_2O_3 crystals

---

[4]Consultant, Department of Chemical and Metallurgical Engineering, University of Tennessee.

[5]R. A. Lefever and G. W. Clark, Rev. Sci. Instr. 33, 769, (1962).

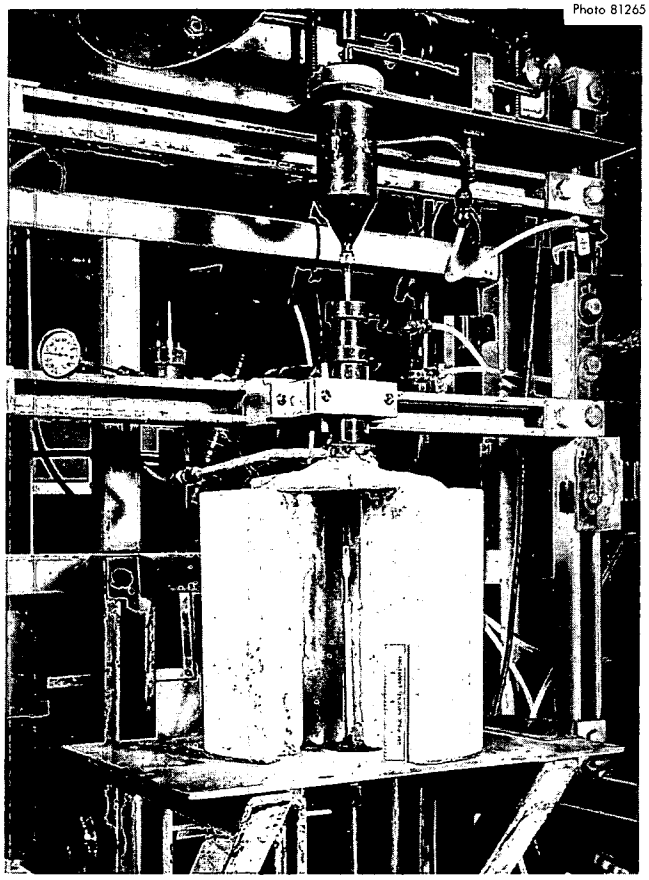

Fig. 1.1. Flame Fusion Apparatus for Growing Al_2O_3 Single Crystals. The furnace muffle has been opened to show an as-grown Al_2O_3 crystal in position.

containing 0.1 wt % TiO_2, 1/4 in. in diameter and 1 in. long, have been successfully grown, free of cracks. These doped crystals still contain bubbles, as discussed in the previous section, and modifications in growth conditions are being studied in an effort to improve the quality of the crystals.

Dispersion Strengthening of Metals by Controlled Precipitation

J. P. Hammond

Aluminum Alloys

Extensive development is under way in this country and abroad to improve the quality of SAP-type alloys (aluminum alloys dispersion hardened with Al_2O_3) for heavy-water-moderated, organic-cooled

reactors.[6,7] Deficiencies in present SAP alloys are their lack of uniformity in mechanical properties and low fracture ductility under constant stress at moderately elevated temperature.[7,8] The behavior of SAP-type alloys in this regard should improve with better control over the size and distribution of the oxide dispersant.

Because the SLIS method[9] of introducing dispersion hardening offers excellent control over fineness and uniformity of dispersion, alloys prepared by this means are being examined as a possible backup material for the more conventionally prepared SAP alloys. The term SLIS refers to the use of a dispersion-forming additive which is soluble in the alloy in its liquid state and insoluble in the solid state. After melting, the alloy is poured as a fine stream from its crucible, whereupon it is blown as atomized particles against a rotating quenching disk. Process parameters are selected to assure quenching from the molten state and at a sufficient rate to freeze the solute atoms in the matrix lattice. By selecting solute elements of low solubility and diffusivity in the matrix, thermal stability of the fine particles that precipitate during fabrication or aging is attained. All operations are conducted under the protection of an inert atmosphere.

Arrangements have been made to obtain 5-lb batches of a number of aluminum alloys prepared by the SLIS process.[9] These alloys contain from 2 to 3 at. % of cerium, yttrium, or beryllium, each of which appears to meet the solute requirements for effective precipitation by the SLIS method.

---

[6]E. C. Supan, Fabrication of Hexagonal APM Process Tubes for Organic-Cooled Reactor Application, NAA-SR-MEMO-8121 (Jan. 11, (1963).

[7]D. Gualandi and P. Jehenson, "Powder Metallurgy of Al-Al_2O_3 Composites (SAP) for Nuclear Applications," paper presented at the 1965 International Powder Metallurgy Conference, New York, June 14–17, 1965.

[8]D. G. Boxall et al., Development of Fuel and Coolant Tubes for a Reactor Cooled by Organic Liquid, AECL-2023. Paper presented at the 3rd United Nations International Conference on the Peaceful Uses of Atomic Energy, Geneva, Switzerland, August 31–September 9, 1964.

[9]A. R. Kaufman and W. C. Muller, Development of Zirconium-Base Alloys Strengthened by SLIS Technique, NMI-1263 (Jan. 15, 1965).

Thorium Alloys

Endeavors to dispersion harden thorium metal with ThO_2 by a method based on ballmilling for thorium powder refinement and blending in the dispersant have met with moderate success.[10] Structures near optimum in fineness of dispersion were obtained and creep strength at 800°C in isolated instances was slightly superior to any reported for thorium alloys. However, the procedure appeared costly and difficult to control. Consequently two additional processes for dispersion strengthening are presently under study.

The first involves the SLIS process described in the previous section. It has been demonstrated that thorium-beryllium alloy powders can be prepared by this process,[9] and excellent results have been obtained for both a Th–1.3 wt % Be and a Th–0.6 wt % Be alloy. The latter powder was successfully fabricated into 1-in.-diam rod by upset-extruding at 600°C with a 9 to 1 reduction ratio.

The second process under consideration involves internal boronation through addition of elemental boron to thorium-zirconium alloy powder and subsequent precipitation of ZrB_2 during elevated-temperature fabrication. We have demonstrated that solid-solution alloys of zirconium in thorium can be hardened substantially by this method. An economically attractive processing scheme would involve preparation of the alloy powder from coprecipitated $ThO_2 \cdot ZrO_2$ by conventional bomb reduction, blending in the boron, and consolidating by hot upset extrusion. In the developmental stages we are using both bomb-reduced powders and powders prepared by hydriding and dehydriding of arc-melted alloys. Material prepared by the latter method lends itself to more definitive evaluation of potentially important process variables because of its higher quality with respect to homogeneity and control of composition and particle size.

---

[10] J. A. Burka and J. P. Hammond, Metals and Ceramics Div. Ann. Progr. Rept. June 30, 1964, ORNL-3670, pp. 249–50.

Three alloy powder compositions have been prepared by the hydride-dehydride route and two by bomb reduction. The nominal compositions, in weight percent, are given below.

Hydride Route	Bomb Reduction
Th–4.65 Zr	Th–3.18 Zr
Th–5 U–4.65 Zr	Th–4.59 Zr
Th–2.25 Zr	

These powders, except for the bomb-reduced batch containing 4.59 wt % Zr, were blended with sufficient boron to quantitatively form ZrB_2. One-in.-diam. pellets were prepared from each batch by hot pressing in graphite dies at 1000°C and a pressure of 4000 psi. All pellets were incorporated in 3-in.-diam billet shells of AISI 1020 steel, with an intervening nickel can as a reaction barrier, for extrusion.

2. FUEL ELEMENT DEVELOPMENT

G. M. Adamson, Jr.

The Fuel Element Development Program continues to be directed toward development of new or improved fabrication techniques for both fuels and cladding materials.

We have demonstrated the chemical feasibility of a one-step thermochemical conversion reaction for either UF_6 or UCl_4 to UO_2. The product in each case may be obtained in the form of a powder or solid. Submicron UO_2 powder produced from UF_6 is currently being evaluated for fabrication behavior.

Preliminary studies of direct reduction of UF_6 with lithium vapor indicate uranium metal may be obtained thus giving a potential method for reduction of a uranium halide to UC, UN or U(CN) mixtures.

Greater control has been obtained in producing homogeneous tungsten-rhenium deposits by modifying the deposition apparatus. Two approaches have been taken to the problem. An external coating apparatus that allows a large gas volume in relation to the substrate has given uniform composition deposits over the full specimen length, while an apparatus designed to provide complete reduction of the gas in a highly localized moving hot zone also gives uniform composition.

Deposition of Uranium Dioxide by Hydroreduction of Uranium Hexafluoride

R. L. Heestand C. F. Leitten, Jr.

Experiments in synthesizing uranium dioxide powder from uranium hexafluoride, hydrogen, and steam were continued due to increasing interest in fabrication behavior of the material. Since particle sizes less than 200 A are usually produced, it is anticipated that the high available surface energy will enhance sintering.

To obtain material for evaluation, eight runs using 25 cm^3/min UF_6, 0.776 cm^3/min H_2O, and 1000 cm^3/min H_2 at 5 torr and 1300°C were made yielding approximately 250 g of powder. It was found that oxygen-to-uranium ratios on the black powder as removed from the

reaction tube ranges between 2.074 to 2.097 with fluorine contents being approximately 5%. It is assumed that the high fluorine content is related to the high surface area of the powder (size approximately 60 to 200 A).

After removal from the reaction tube, the powder was fired in wet hydrogen at 1000°C for 4 hr, giving an oxygen-to-uranium ratio of 2.005 and a fluorine content ranging from 150 to 400 ppm. One hundred twenty grams of powder were shipped to Battelle Northwest for evaluation while the remainder will be used for evaluation at ORNL. A pellet cold pressed and sintered 2 hr at 1700°C in hydrogen was found to have a density of 93%. Studies on the powder to optimize sintering will be continued.

Direct Thermochemical Conversion of UCl_4 to UO_2

F. H. Patterson W. C. Robinson, Jr.
C. F. Leitten, Jr.

As previously reported,[1,2] thermodynamic considerations predict the feasibility of producing UO_2 by the direct reaction of UCl_4 with oxygen and the subsequent reduction of the intermediate reaction product by wet hydrogen.

Experimental facilities necessary for this investigation were constructed of quartz within an exhaust hood. To facilitate material handling, an "on stream" chlorinator was used to prepare the desired UCl_4 gas. Sufficient quantities of this gas were produced in this system by passing 280 cm^3/min chlorine over cleaned uranium metal sheet at 550°C with a system pressure of 2 torr. About 50 cm^3/min Ar was added to the chlorine to help transport the resultant chlorides into the reaction zone of the system.

---

[1]F. H. Patterson, W. C. Robinson, Jr., and C. F. Leitten, Jr., Fuels and Materials Development Program Quart. Progr. Rept., Mar. 31, 1965, ORNL-TM-1100, pp. 3–4.

[2]F. H. Patterson, W. C. Robinson, Jr., and C. F. Leitten, Jr., Fuels and Materials Development Program Quart. Progr. Rept., June 30, 1965, ORNL-TM-1200, p. 4.

In the reaction zone, 540 cm^3/min O_2 was injected directly into the incoming UCl_4 gas stream followed by the injection of 300 cm^3/min H_2 downstream to produce the uranium oxide deposit. A series of depositions was carried out over the temperature range 660 to 950°C at a constant system pressure of 2 torr to establish the feasibility of depositing both free-standing solids and submicron-size powder. Above 800°C, the product, a mixture of UO_2 and U_3O_8, was deposited as a solid on the walls of the reaction tube. Analysis of this material afforded an oxygen-to-uranium ratio of approximately 2.5 and 50 ppm residual chlorine. Below 800°C, the reaction product was partly solid with some loose submicron-size powder also being present. Analysis by x-ray diffraction identified this material as U_3O_8 with some traces of UO_2. This powder was converted to stoichiometric UO_2 by firing in wet hydrogen at 1000°C.

Gas flows will be scaled up in the existing system to demonstrate the feasibility of producing heavier free-standing solid deposits of UO_2 and larger quantities of submicron-size powder for further characterization.

Deposition of Uranium Compounds by Lithium Reduction of UF_6

W. C. Robinson, Jr. C. F. Leitten, Jr.

After resolution of previous vacuum difficulties,[3] experiments were performed to verify the feasibility of the reaction

$$UF_6(g) + 6\ Li(g) \rightleftarrows U(s) + 6\ LiF(g) \quad . \qquad (1)$$

Previous thermodynamic calculations[4] indicated that this reaction should be feasible. Once feasibility of this reaction is

---

[3]W. C. Robinson, Jr. and C. F. Leitten, Jr., Fuels and Materials Development Program Quart. Progr. Rept., June 30, 1965, ORNL-TM-1200, p.5.

[4]W. C. Robinson, Jr. and C F. Leitten, Jr. Fuels and Materials Development Program Quart. Progr. Rept., March 31, 1965, ORNL-TM-1100, pp. 4–5.

established, CH_4 will be introduced into the entering gas streams in an effort to deposit uranium carbide.

The lithium was inserted into the apparatus and the lithium chamber heated to 700°C. A pressure of 1 torr was established in the deposition chamber, and the lithium vapor was allowed to flow from the lithium chamber into the deposition chamber. The deposition chamber was maintained at 1000°C in the reaction zone and had a water-cooled end. When lithium began to condense in the cold end of the deposition chamber, a flow of 15 to 20 cm^3/min UF_6 was introduced into the reaction zone. This procedure was followed for two experiments. In both experiments, the UF_6 injector became plugged. Examination revealed that a metallic deposit had formed in the UF_6 injector and finally closed off the tip. This deposit has been identified as uranium metal and is now undergoing analysis for lithium and fluorine content.

These experiments establish the feasibility of reaction (1), but equipment modifications must be made to prevent the UF_6 reduction at the gas injector tip.

Deposition of Tungsten Alloys

J. I. Federer C. F. Leitten, Jr.

Improvements in uniformity of composition and thickness of tungsten-rhenium deposits have been accomplished by a moving hot-zone technique.[5] A characteristic feature of these deposits has been circumferential ridges of varying height, width, and spacing. In a nominally 20-mil-thick deposit the ridges are about 20 mils high, 20 to 40 mils wide, and spaced 1/16 to 1/4 in. apart. The microstructure of a ridge growth, shown in Fig. 2.1, is similar to that of nodular growths sometimes found in tungsten deposits.[6] Grown-in porosity occurs along the grain interfaces.

---

[5]J. I. Federer and C. F. Leitten, Jr., Fuels and Materials Development Program Quart. Progr. Rept., June 30, 1965, ORNL-TM-1200, pp. 5–9.

[6]F. H. Patterson and C. F. Leitten, Jr., High-Temperature Materials Program Quart. Progr. Rept., Jan. 31, 1965, ORNL-TM-1050, pp. 98–99. CLASSIFIED.

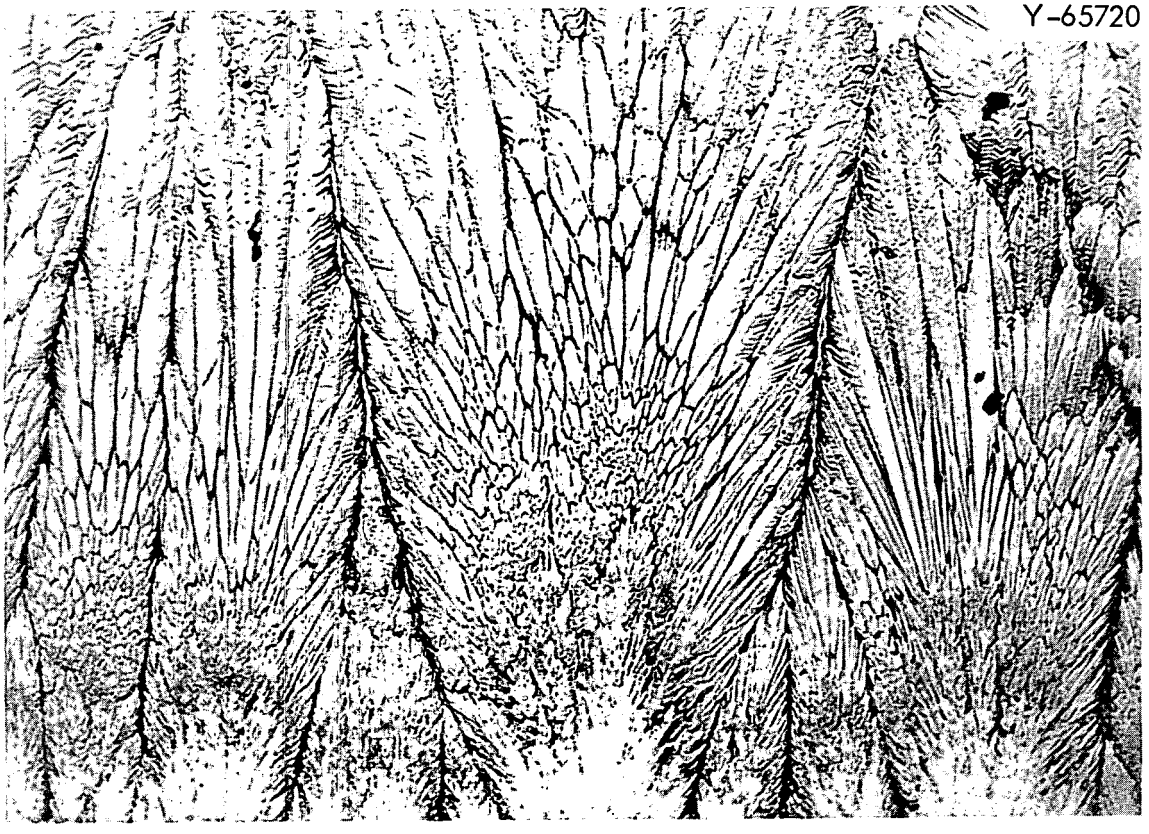

Fig. 2.1. Microstructure of a Ridge Growth in a Tungsten-Rhenium Deposit Prepared with a Moving Hot Zone. Etchant: 50% NH_4OH–50% H_2O_2. 250X.

These ridges were tentatively attributed to sharp thermal gradients within the hot zone of the deposition tube which was heated by induction. However, the use of a susceptor to heat the tube by direct radiation did not eliminate the ridges. Examination of numerous deposits prepared in a moving hot zone indicated that the ridges began to form on the inlet side of the hot zone, a region having a sharp thermal gradient. This was confirmed in two separate experiments. A deposit was allowed to form on the inner wall of a stainless steel deposition tube heated by radiation from a susceptor. The deposition conditions were similar to those used previously,[5] except that the hot zone was stationary. Upon examination of the deposit, ridges were found on the inlet side of the hot zone. In another experiment, the deposit formed on the outer wall of a deposition tube contained within a quartz tube so that observations could be made during deposition. Again, the first ridge formed on the inlet side of the hot zone and grew upon passing through the hot zone.

Sufficient experiments have now been conducted to show that the moving hot-zone technique has potential for preparing tungsten-rhenium deposits having uniformity of composition and thickness; but unless the ridges can be eliminated or greatly minimized, the deposits will be unsatisfactory for many applications.

Another technique being investigated for preparing tungsten-rhenium deposits consists of deposition on the outer surface of a mandrel which is contained in a relatively large mixing chamber as shown schematically in Fig. 2.2. The chamber is about 4 in. in outside diameter and 12 in. long and is fitted with end flanges. The 3/4-in.-OD deposition mandrel extends through the flanges and is heated internally. A gas-inlet port is provided in one end flange and an exhaust port in the other. The inlet gases and the by-product gas, HF, expand into the mixing chamber, thus providing a more uniform gas mixture for reaction at the mandrel surface than is possible in the case of internal deposition in a relatively long and narrow tube. A deposit was prepared at 600°C, 10-torr pressure, and gas flow rates of 2000, 60, and 20 cm^3/min of H_2, WF_6, and ReF_6, respectively. A metal recovery of 78% was obtained, and the rhenium content along the length of the deposit is given below.

Distance from gas inlet (in.)	Rhenium content (%)
2	26.2
3	26.1
4	26.4
5	25.3
6	25.5
7	23.4
8	25.2
9	25.3
10	23.3

The deposit had a smooth surface texture with only a few growth cones or nodules. The microstructure, shown in Fig. 2.3, was unlike

ORNL-DWG 65-11272

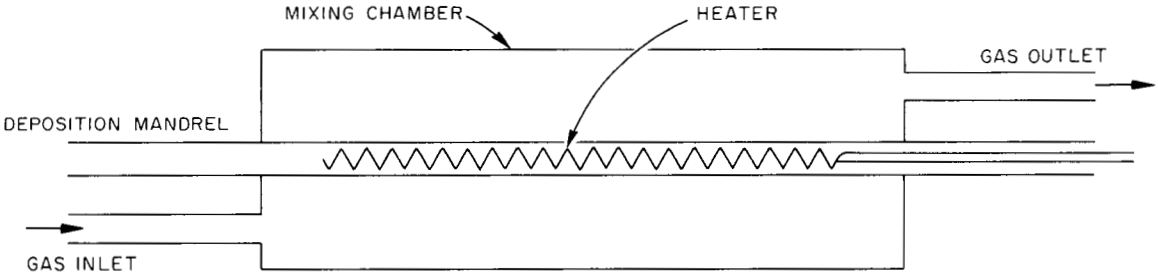

Fig. 2.2. Schematic of Apparatus for Deposition on the Outer Surface of a Mandrel.

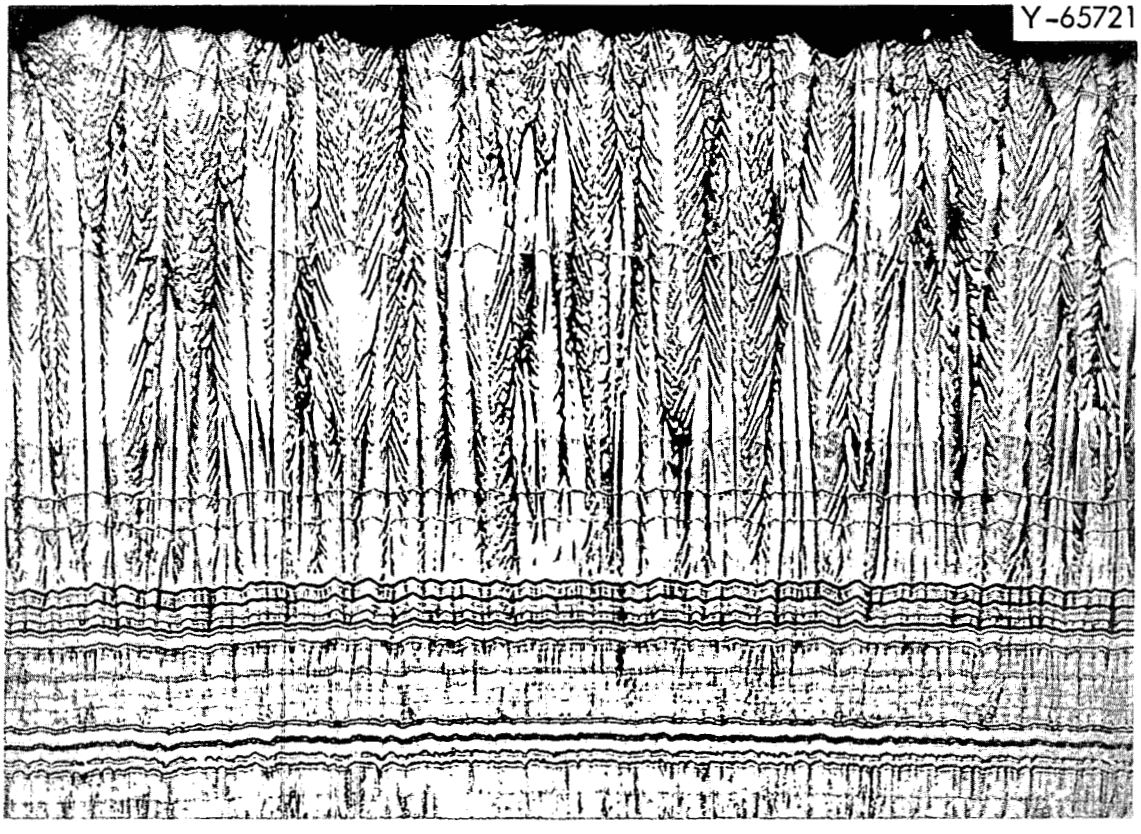

Fig. 2.3. Layered Structure in a Tungsten-Rhenium Deposit Prepared in an External Coating Apparatus. Etchant: 50% NH_4OH–50% H_2O_2. 250X.

the columnar structures in deposits prepared by other techniques. The layered structure shown in Fig. 2.3 is similar to the structure found in tungsten-rhenium deposits prepared by thermal decomposition of tungsten and rhenium chlorides at about 1200°C.[7] Layering is a phenomenon associated with alloy deposition and, possibly, can be minimized by adjusting the deposition parameters. Further experiments are planned to evaluate the technique.

The deposition of fine-grained, rather than the usual columnar-grained, tungsten was not pursued during this report period because major emphasis was placed on problems of tungsten-rhenium deposition. The microstructure of a deposit to which vanadium was added as an alloying constituent[5] is shown in Fig. 2.4. The grain structure of this material,

[7]Richard Kaplan, San Fernando Laboratory, private communication.

Fig. 2.4. Grain Structure of a Tungsten Deposit Containing 880 ppm V. Etchant: 50% NH_4OH–50% H_2O_2. 200×.

which contained 880 ppm V, was neither columnar nor equiaxed. The grains were elongated in the growth direction, upwards (as can be seen in Fig. 2.4), but did not extend completely through the deposit. The two dark lines near the bottom of Fig. 2.4 may be entrapped VF_3, which was identified as a microconstituent in other regions of the deposit.

Future experiments will utilize the external coating apparatus in an effort to achieve a more uniform distribution of the alloying constituents. Plans also include the introduction of controlled amounts of oxygen and carbon to the alloys.

3. NONDESTRUCTIVE TEST DEVELOPMENT

R. W. McClung

Our program is intended to develop new and improved methods of evaluating reactor materials and components. To achieve this we have studied various physical phenomena, developed instrumentation and other equipment, devised application techniques, and designed and fabricated reference standards. Among the methods being actively pursued are electromagnetics (with major emphasis on eddy currents), ultrasonics, and penetrating radiation. In addition to our programs oriented toward the development of methods, we are studying these and other methods for evaluation of problem materials and developing techniques for remote inspection.

Electromagnetic Test Methods

C. V. Dodd

Analytical Studies

We have continued research and development on electromagnetic phenomena on both an analytical and empirical basis. As a part of the program, we are studying the mathematical determination of impedance of an eddy-current coil and other electromagnetic phenomena as a function of coil dimensions, frequency, specimen conductivity and permeability, and coil-to-specimen spacing (lift-off). A technical memorandum[1] has been published which contains a derivation of the equations and examples of their use.

Beat-Frequency Eddy-Current Instrument

We have developed and constructed a prototype beat-frequency eddy-current instrument to measure conductivity variations in metals. The

[1]C. V. Dodd, A Solution of Electromagnetic Induction Problems, ORNL-TM-1185 (August 1965).

instrument has two L-C oscillators. One oscillator is tuned by the impedance of the test coil as it is affected by the metal specimen. The second oscillator is tuned by a variable piston capacitor to track the first oscillator. We designed the shape of the capacitor to give linear dial readings directly in microhm centimeters. The two frequencies are beat together and the output is fed into a speaker. While the instrument does not have any lift-off compensation, it does have the advantages of high resolution, direct readings, portability, and inexpensive components. This instrument approach has the potential for the greatest sensitivity and accuracy of any of the common eddy-current circuits.

Ultrasonic Test Methods

K. V. Cook

Nonbond Studies

We have continued our studies on the behavior of ultrasound in thin sections with the principal effort being the detection of nonbonds in cladding structures. We are attempting to develop a system for evaluating fuel tubes in a "hot" (radiation level) laboratory.[2] The Teflon guide block has been fabricated, and we have demonstrated that it will maintain proper alignment between the transducer and the specimen during evaluation.

A mechanical system for helically scanning the fuel tubes inside a hot cell has been designed and fabricated in conjunction with personnel from HRLEL. The scanner is now in our laboratory for an operational checkout and will probably be installed in the hot-cell facility within one month.

---

[2]K. V. Cook, Fuels and Materials Development Program Quart. Progr. Rept. June 30, 1965, ORNL-TM-1200, p. 27.

Tubing Inspection

Reference Standards. — We are continuing to work on the problems encountered in tubing inspection. A major problem is the establishment of realistic ultrasonic notch standards for calibration. Electrical-discharge machining appears to be a reliable method for making both inner- and outer-surface notches, and we are continuing to use this technique for our studies. In an effort to decrease the width of our notches until they more nearly resemble cracks, we machined notches with an 0.001-in.-thick tantalum tool. Tool wear is considerably reduced with the tantalum when compared to the brass shims we have been using; however, the notch width was not decreased. Figure 3.1a shows an 0.002-in.-deep notch made with a brass tool and Fig. 3.1b shows a similar notch fabricated using the tantalum tool. Actually the notch cut with the brass would make a better standard and it can be cut about six times faster. We will make further attempts to narrow the notch width. We have demonstrated that the calibration curves derived for 1/8-in.-long notches are also valid for 1/4- and 1/2-in.-long notches.

Contact-Immersion Testing

Sheet and Plate Evaluation. — Many times it would be desirable to be able to combine features of both the contact and the immersion methods of ultrasonic testing. This is especially true for evaluating sheet or plate for transverse cracking using a shear-wave ultrasonic technique. The contact method allows scanning of moderately warped sheet without loss of sensitivity and also allows hand scanning so the transducer can be rotated continuously, thereby detecting transverse discontinuities of any orientation. However, this method required a constant transducer pressure and coupling to assure a reliable inspection. Also, the crystal mounting can damage the sheet being inspected. The immersion technique deletes the problems just described; however, it takes excessive inspection time to scan for all possible orientations of transverse cracking, and for warped sheets certain areas will not be evaluated. Thus, if the good features of each could be combined, it could provide an improved system for scanning

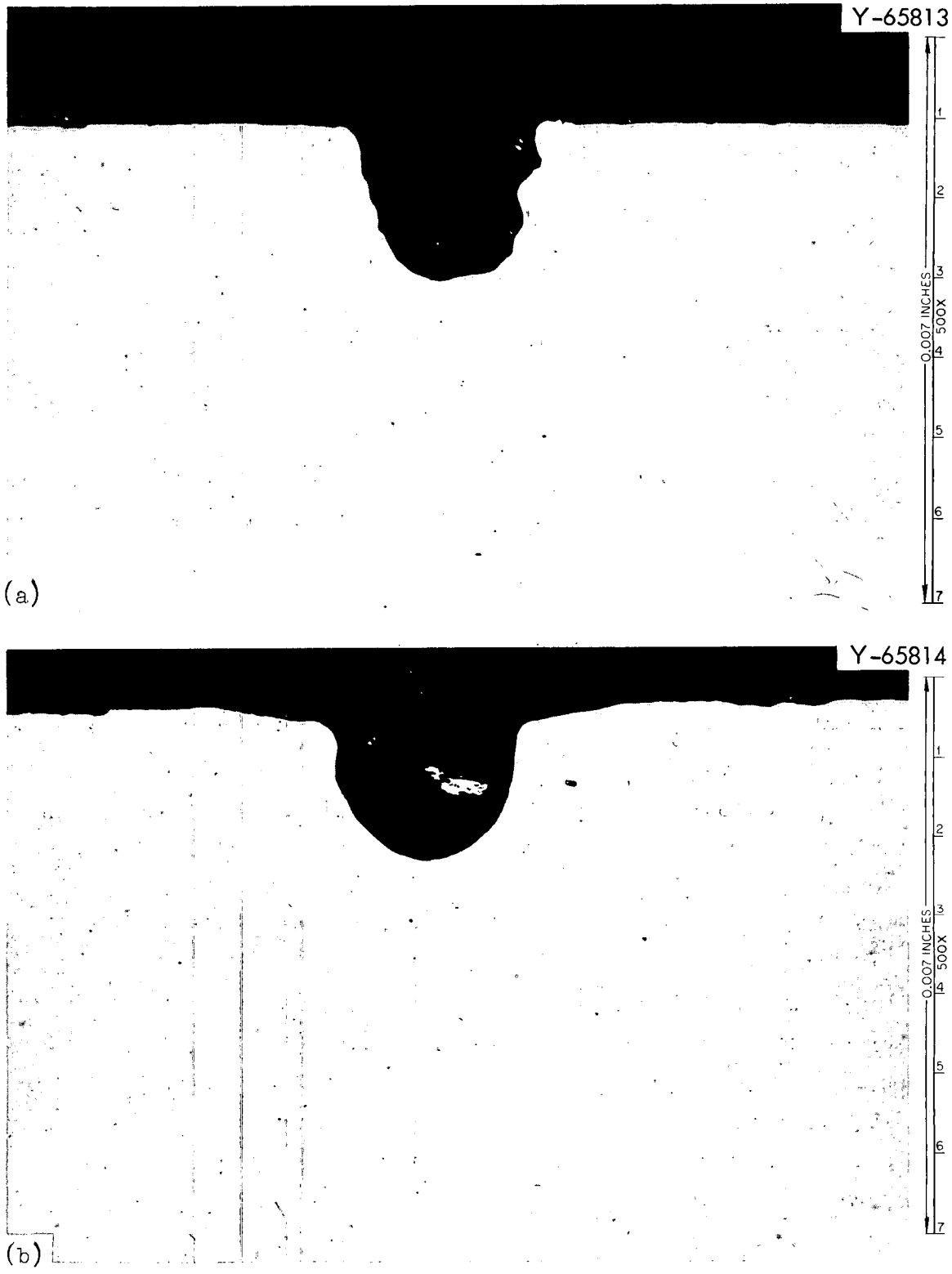

Fig. 3.1. Notches Fabricated by Electro-Discharge Machining. As-polished. (a) Using brass shim and (b) using tantalum shim.

sheet and plate for transverse cracking. A hand manipulated scanner has been designed and fabricated to allow this combination. The device holds the transducer at a variable angle (0 to 50°) and rides on the inspection piece on four Teflon contact points. With this mechanism, the plate can be moderately warped and the inspection still be valid. We have been using the device on a table which has a 3-in.-deep stainless steel immersion tank as a top.

Pipe Joint Evaluation. — The same contact-immersion device developed for evaluating sheet can be applied to the evaluation of pipe joints by the ultrasonic shear-wave method. The current design requires a straight section of pipe so that front and rear feet of the device are on a line parallel to the pipe axis for sending a sound beam longitudinally along the pipe. This system will be applicable to the evaluation of butt welded pipe joints.

Penetrating Radiation

X- and Gamma-Ray Attenuation Gaging — B. E. Foster, S. D. Snyder

Fuel Element Homogeneity. — We are continuing the study of x- and gamma-ray attenuation for the evaluation of fuel elements. Variation in transmitted intensity is monitored readily using a scintillation detector and is then related through proper calibration to the fuel loading homogeneity within the area of interest. The data analysis is continuing on two vibratorily compacted Th–3 wt % UO_2 fuel rods (1/2 in. in diameter), six ThO_2 pellets (1/2 in. in diameter), and nine ThO_2 pellets (3/4 in. in diameter) that were scanned for homogeneity using ^{60}Co and ^{137}Cs as the radiation sources.[3] For this analysis we are making a series of graphs relating scanning speeds, energy of the radiation source, inhomogeneity sensitivity and system stability. The results of the overall evaluation will provide us with data for selecting the proper isotope, scanning speed, and collimator size to determine the homogeneity in vibratorily compacted fuel rods in this size range.

[3]B. E. Foster and S. D. Snyder, Fuels and Materials Development Program Quart. Progr. Rept. June 30, 1965, ORNL-TM-1200, p. 29.

Gaging Probes for Hollow Cylindrical Specimens. — We are continuing our investigations into the development of scintillation detector probes to be inserted into hollow cylindrical specimens for determination of fuel homogeneity or wall thickness by x-ray attenuation. The use of light pipes is being studied for transmitting the light from a NaI(Tl) crystal to a photomultiplier tube when the crystal is bombarded with x or gamma rays.[4] We have compared 5/16-in.-diam, 20-in.-long Lucite and quartz rods that were coupled between a 1/4-in.-diam, 1/2-in.-long NaI(Tl) crystal and an RCA 6342A photomultiplier. These crystal and light pipe assemblies were inserted into stainless steel tubing with an 0.020-in.-wall thickness, and variations in thickness as small as 0.2% were detectable.

We observed very little difference in light transmission efficiency between the Lucite and the quartz. Since the quartz requires considerably more effort to prepare than the Lucite, we do not intend to pursue the use of quartz at this time. A literature survey is in progress concerning the use of various light transmitting materials for light pipes and a program for optimizing material, shape, size, and other important parameters for our applications has been outlined.

Scintillation Spectrometry — B. E. Foster, D. W. Neil

We are continuing the program for determining the uranium content in uranium-aluminum alloy rectangular blanks using a nondestructive technique. The equipment consists of a NaI(Tl) crystal and photomultiplier tube, linear amplifier, single-channel analyzer, high-voltage supply, scaler, and timer connected in the conventional spectrometer arrangement. With the spectrometer we monitored the count rate of the 184-kev gamma ray from the decay of ^{235}U. The count rate was determined for 5-min periods at frequent intervals over several days as a check on instrument stability. The equipment proved quite stable, and reproducible data were obtained. It was necessary to establish a relationship between count

[4]B. E. Foster and S. D. Snyder, Fuels and Materials Development Program Quart. Progr. Rept. Mar. 31, 1965, ORNL-TM-1100, p. 23.

rate and uranium content. This was accomplished by obtaining the count rate from several core blanks, each with a different uranium loading. Then the cores were dissolved chemically for uranium content. Of course, as the uranium content increases, there is an increase in self-absorption of the 184-kev gamma ray. Corrections to the observed counting rates were made for self-absorption and instrument resolving time. A plot was then made of corrected count rate vs grams uranium. Subsequent cores can be counted and the uranium content read directly from the plot. The calibration is incomplete but a cursory examination of the data looks quite promising for accurate values over a wide range of uranium content.

4. ZIRCONIUM METALLURGY

M. L. Picklesimer

We are conducting research along several lines on zirconium-base alloys of potential use as structural materials for water-cooled and/or -moderated reactor systems. The principal projects are: (1) studies of the physical metallurgy, including transformation kinetics and morphologies, mechanical properties, phase diagrams, and heat-treatment response; (2) the development, evaluation, and utilization of preferred orientation and strain anisotropy in α-zirconium alloys during fabrication, and the utilization of yield stress anisotropy in increasing maximum permissible design stresses in structures; (3) the determination of the effects of composition, temperature, and environment on the oxidation-corrosion rates in the thin-film stages of oxide growth; (4) a study of the effects of alloy composition and oxidation environment on the structural properties of thin oxide films in situ; and (5) investigation of stress orientation of hydrides in Zircaloy-2.

Precipitation of Hydrides in Zircaloy-2 as Affected by Preferred Orientation, Elastic Stress, and Hydrogen Content[1]

P. L. Rittenhouse M. L. Picklesimer

Hydride plates in Zircaloy-2 that are oriented perpendicular to a stress direction can drastically reduce ductility. This report discusses a continuation of work to determine the factors that influence directional precipitation of the hydrides.

Zircaloy-2 specimens were hydrided to three hydrogen levels and the hydrides were precipitated while the specimens were subjected to an elastic stress in either the rolling or transverse direction.

---

[1]Abstract of report ORNL-TM-1239 (September 1965).

Stresses applied during precipitation cause a reorientation of the hydrides which is dependent on stress level, the direction of stress relative to crystallographic features of the texture of Zircaloy-2, and the hydrogen content.

The Effect of Temperature Cycling Under Load on the Directional Precipitation of Hydrides in Zircaloy-2

P. L. Rittenhouse

The effects of preferred orientation, stress, and hydrogen content on the directional precipitation of hydrides in Zircaloy-2 have been studied and the data presented.[1,2,3] All of the load tests performed in the past have been single-cycle tests; that is, the hydrides were precipitated during only one cooling from 400°C. In the present series of tests, specimens of Schedule 18 Zircaloy-2 (Ref. 4) (nominally 150 ppm H_2) were heated and cooled while continuously under an elastic stress of 15,000 psi for as many as twenty cycles. All of these tests were made on specimens with stress axes parallel to the transverse direction of the rolled plate from which they were cut.

The hydride pole figures[5] determined after 1, 5, and 10 cycles of heating and cooling under the elastic stress are very similar, with a maximum pole density of slightly more than 4 at the normal direction, as shown in Fig. 4.1. The maximum pole density observed in the control (or unstressed) specimens was 20 at the same location.[4] After 20 cycles of heating and cooling, the maximum pole density near

---

[2]P. L. Rittenhouse, Fuels and Materials Development Program Quart. Progr. Rept. June 30, 1965, ORNL-TM-1200, pp. 31–35.

[3]P. L. Rittenhouse, Fuels and Materials Development Program Quart. Progr. Rept. June 30, 1964, ORNL-TM-920, pp. 57–60.

[4]P. L. Rittenhouse and M. L. Picklesimer, The Effect of Preferred Orientation and Stress on the Directional Precipitation of Hydrides in Zircaloy-2, ORNL-TM-844 (June 1964).

[5]M. L. Picklesimer and P. L. Rittenhouse, "Hydride and Basal Pole Figures in Zircaloy-2 by Quantitative Metallography," paper presented at the 19th Atomic Energy Commission Metallographic Meeting, Oak Ridge National Laboratory, April 20–22, 1965 (proceedings to be published as ORNL-TM-1161).

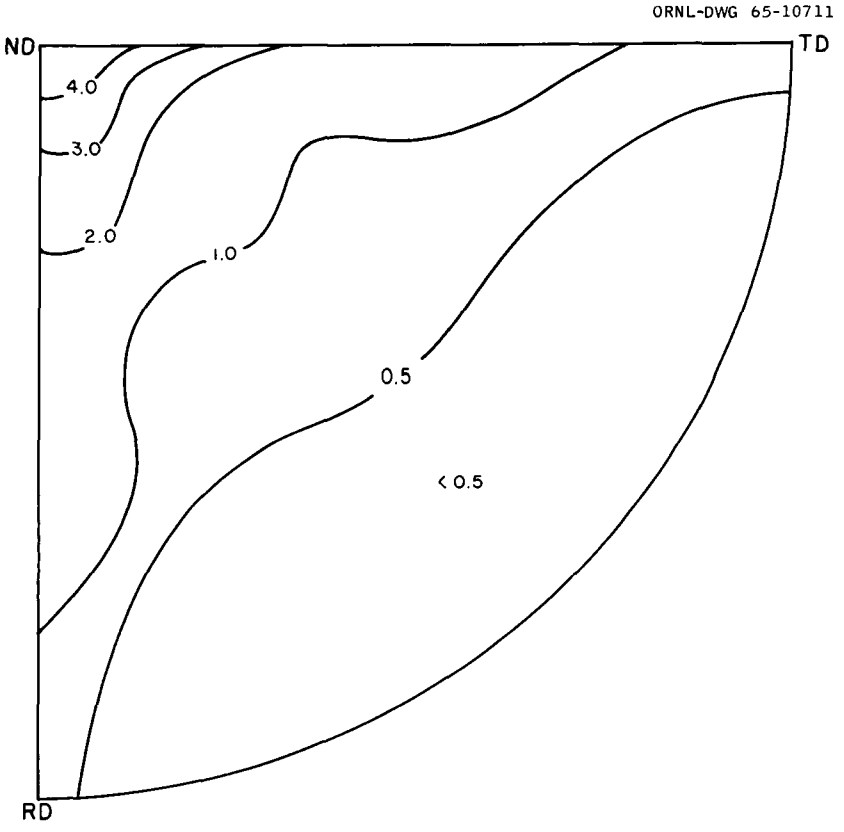

Fig. 4.1. Hydride Pole Figure in Zircaloy-2 after Five Thermal Cycles from 100 to 400°C. Elastic stress of 15,000 psi continuously applied. Schedule 18 Zircaloy-2, 150 ppm H_2.

the normal direction was somewhat more than 6, as shown in Fig. 4.2, and a second peak of intensity 3 had developed at about 30° towards the transverse direction. At the present time, we can not conclude that this single result for 20 cycles is significant nor that further cycles will further change the hydride orientation. A second specimen is being cycled 20 times. If the present result is confirmed, a new series of much greater number of cycles will be started. In addition, the effect of cooling rate during a single cycle will be examined.

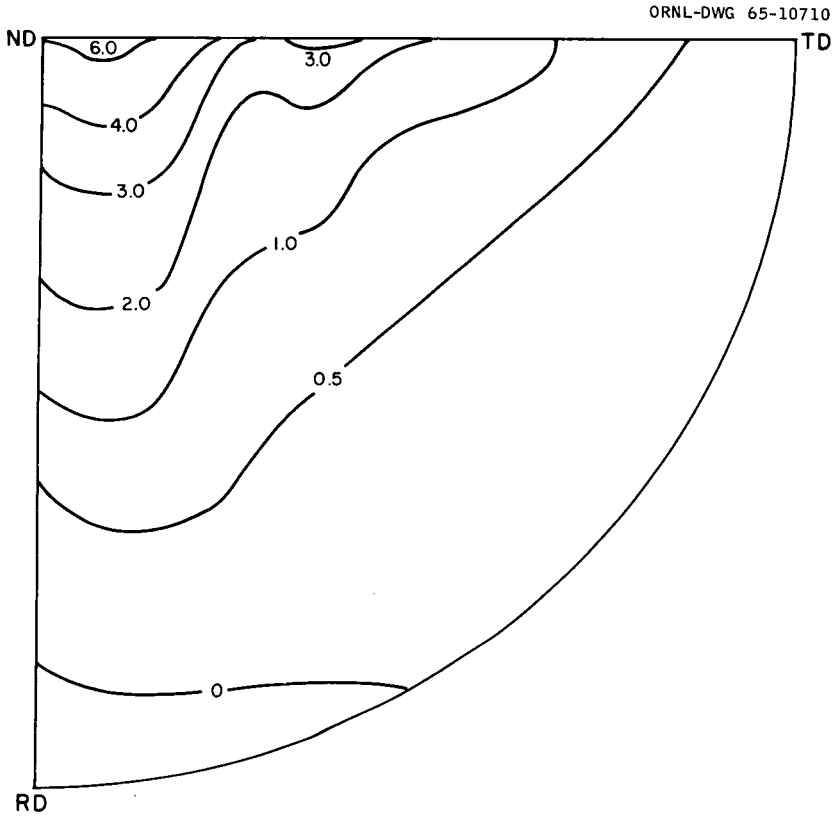

Fig. 4.2. Hydride Pole Figure in Zircaloy-2 after 20 Thermal Cycles from 100 to 400°C. Elastic stress of 15,000 psi continuously applied. Schedule 18 Zircaloy-2, 150 ppm H_2.

Anisotropy in Zircaloy-2

P. L. Rittenhouse M. L. Picklesimer

While awaiting the delivery of Zircaloy-2 tubing to be used in the program for determining the stress-strain anisotropy under conditions of biaxial stress, the tube-testing apparatus is being used to perform compression testing of Zircaloy-2 specimens having over 20 different crystallographic textures. The compression yield strengths and strain anisotropy data being collected will be used in conjunction with the tensile data previously obtained on these materials to give a more complete understanding and description of the anisotropy of mechanical properties in these materials.

The cross sections of round tensile and compression specimens of Zircaloy-2 become elliptical when plastically strained. The eccentricity of the ellipse of cross section varies with the magnitude of plastic strain and the orientation of the tension and compression axes relative to the crystallographic texture (and its perfection) of the material. It was found experimentally that the contractile strains in a tensile specimen could be expressed as a simple linear function of the axial strain.[6] The equations relating the natural strains are:

$$\bar{\epsilon}_{ij} = k_{ij}\,\bar{\epsilon}_{ii} \qquad (1)$$

and

$$\bar{\epsilon}_{ik} = k_{ik}\,\bar{\epsilon}_{ii} \quad , \qquad (2)$$

where k_{ij} and k_{ik} are the slopes of the axial strain-contractile strain plots and are constant for each strain direction in a given specimen over all strains from yielding to fracture. For an isotropic material,

$$k_{ij} = k_{ik} = -0.5 \qquad (3)$$

for all specimen axis orientations. The values of k_{ij} and k_{ik} observed in Zircaloy-2 tensile specimens have ranged from −0.05 to −0.95. The subscript notation used for these various strains is shown in Fig. 4.3 for both tensile and compressive strains in the direction of the specimen axis.

Values of k_{xy}, k_{xz}, k_{yx}, and k_{yz} can be determined from specimens with tensile axes in the rolling and transverse directions. An experimental determination of k_{zx} and k_{zy} is not usually possible

[6] P. L. Rittenhouse and M. L. Picklesimer, Metallurgy of Zircaloy-2: Part II. The Effects of Fabrication Variables on the Preferred Orientation and Anisotropy of Strain Behavior, ORNL-2948 (Jan. 11, 1961).

ORNL-DWG 65-8566

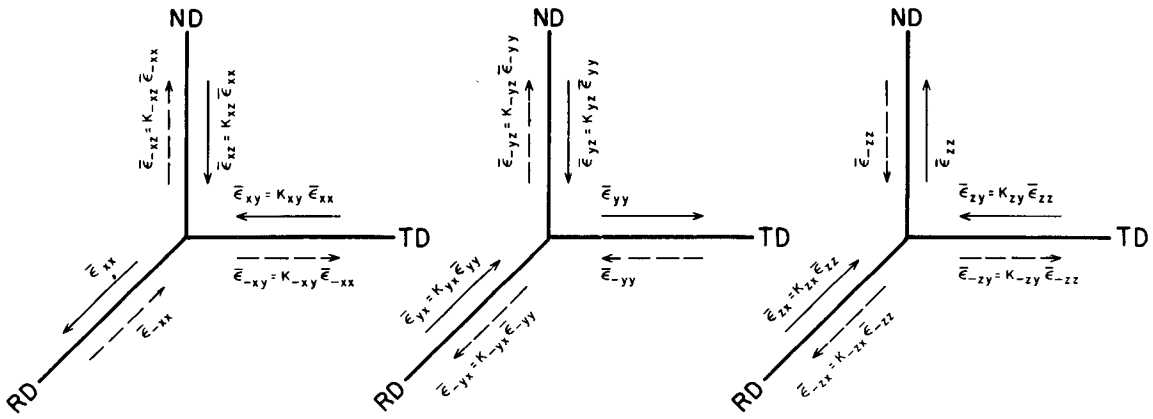

Fig. 4.3. Subscript Notation and Strain Anisotropy Constants for Uniaxial Tension and Compression.

for plate material, since it would require a tensile specimen with the tensile axis in the normal direction of the plate. However, it is possible to measure all six k's for compression specimens. This has been done for four of the materials with the result that the six k values satisfy the equation:

$$\frac{k_{-xy}}{k_{-xz}} \cdot \frac{k_{-yz}}{k_{-yz}} \cdot \frac{k_{-zx}}{k_{-zy}} = 1 \pm 0.02 \ . \qquad (4)$$

This equation was previously derived[6] by extending Hill's theory of yielding and plastic flow.[7]

Since the deformation of Zircaloy-2 in tension and compression occurs on the same slip system and on twinning planes with the same sixfold symmetry with respect to the basal plane, there is good reason to believe that Eq. (4) is applicable to the tensile specimen deformations as well. It is then possible to compute k_{zx} and k_{zy} after an

[7]R. Hill, Proc. Roy. Soc. (London), Ser. A, 193, 281 (1948).

experimental determination of the other four tensile k values. This is done as follows. First, the plastic true strain equation

$$\bar{\epsilon}_{ii} + \bar{\epsilon}_{ij} + \bar{\epsilon}_{ik} = 0 \qquad (5)$$

gives, by substitution of Eqs. (1) and (2),

$$k_{ij} + k_{ik} = -1.0 \quad . \qquad (6)$$

Simultaneous solutions of Eqs. (4) and (6) then gives

$$k_{zx} = \frac{k_{xz}\, k_{yx}}{k_{xy}\, k_{yz} + k_{xz}\, k_{yx}} \quad . \qquad (7)$$

By Eq. (6), the number of independent values of the k's is reduced from six to three for either tension or compression. On the assumption that Eq. (4) is valid, the number of independent k's is further reduced to two. Thus, the determination of one contractile-to-axial strain ratio on a specimen with its tensile stress axis in the rolling direction and a second on a specimen with the tensile stress axis in the transverse direction provides sufficient information to calculate the values of all six k's in tension. Since the deformation systems available are limited, it seems likely that there would be a relatively simple relationship between the k values for tension and compression along the same stress axes. An empirical correlation of the k values in tension and compression for the four lots of Zircaloy-2 tested to date is shown in Fig. 4.4. More determinations of k values in compression will be required before this correlation can be accepted. No relationship can be presently derived from the available theories of anisotropy, for none have considered such behavior to be possible, all assuming that the behavior is the same in tension and compression. If the empirical relationship is proven to be valid, it will permit a reduction from four to two in the number of k values that must be

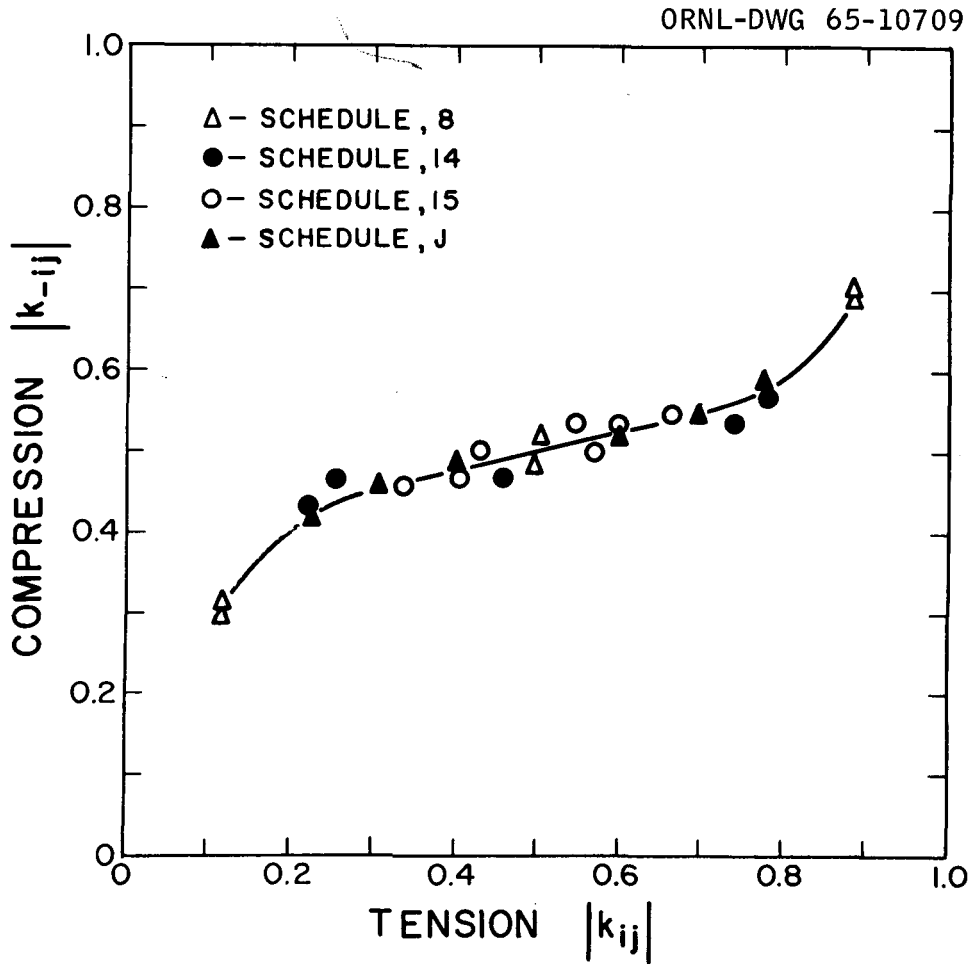

Fig. 4.4. Correlation of Strain Anisotropy Constants (k_{ij},k_{ik}) in Tension and Compression for Zircaloy-2.

determined to completely describe the strain anisotropy of Zircaloy-2 in uniaxial stress in this notation.

The preliminary data on both k values and compression yield strengths indicate that at least an empirical relationship can be established between tensile and compressive k values and yield strengths. The relationship, if proven, would require the measurement of only two tensile yield strengths and two k values from the tensile specimens to provide a complete description of the plastic stress-strain anisotropy of Zircaloy-2.

Strain Behavior in Zircaloy-2 Sheet-Type Tensile Specimens[8]

P. L. Rittenhouse M. L. Picklesimer

Rolling and transverse direction sheet-type tensile specimens of highly textured Zircaloy-2 were prepared and tested to study strain behavior as a function of specimen geometry. The results of these tests are compared with those obtained from round tensile specimen of the same material.

Nonuniform strain is exhibited in the necked region of the sheet specimens. This adds to the difficulty of using this type of specimen as a measure of strain anisotropy through ratios of contractile-to-axial strain. Some peculiarities in necking behavior are also discussed.

Crystal Structure Ball Models

M. L. Picklesimer D. O. Hobson

One of the more difficult tasks encountered in attempting to determine atom movements during slip and twinning is that of visualization of the atom arrangements on the crystallographic planes of interest. Drawings can be made, but three-dimensional patterns are quite difficult to demonstrate. A new technique has been developed that permits rapid and easy construction of the atom arrangement on any crystallographic plane of interest in either the face-centered cubic or the close-packed hexagonal structures. All attempts to construct body-centered cubic structures by this method have failed.

The new technique uses ferromagnetic steel bearing balls, Alnico horseshoe magnets, and plastic petri dishes. The steel balls become "sticky" in the field of the magnet, and are attracted to each

---

[8]Abstract of report ORNL-TM-1226 (September 1965).

other. As many as 5000 balls have been stacked in one model. A tool for adding balls to the model is easily made from copper tubing by cutting two slots from opposite sides of the tubing a ball diameter apart and about 3/4 in. from one end and forming a spring brass strip with tabs to enter the slots.

A ball drops into the slot region on pressing the strip and out the end of the tube when the brass strip is released. The copper tubing is long enough to hold 300 to 400 balls on each loading. The open end is flared to make loading easier and is closed with a cork or rubber stopper. The use of the tool, the magnets, and the petri dishes in the construction of a ball model is shown in Fig. 4.5.

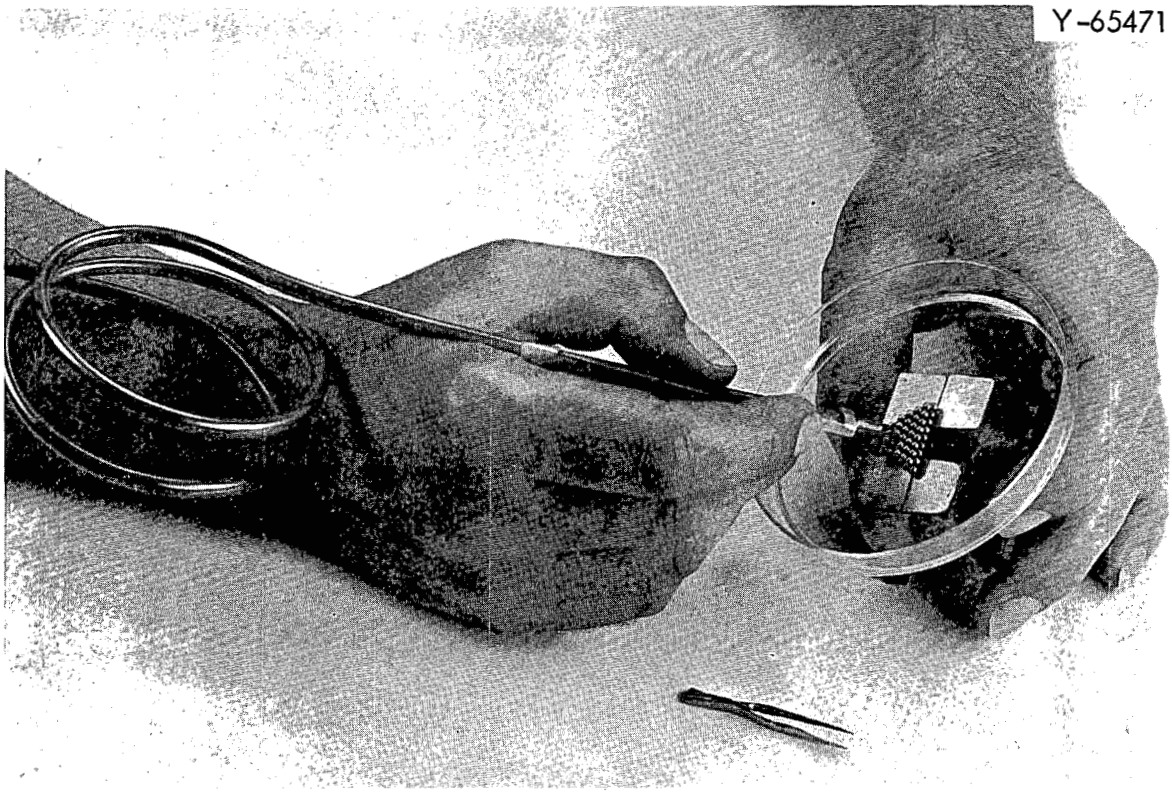

Fig. 4.5. Method of Adding Balls to Ball Model of Crystal Structure.

A ball model of the face-centered cubic structure is shown in Fig. 4.6. Balls colored by heat tinting have been used to outline certain features of the model for emphasis and to make examination of the photograph easier. Ball models of several crystallographic planes of the close-packed hexagonal crystal structure are shown in Figs. 4.7, 4.8, and 4.9. The two possible atom arrangements on the $\{10\bar{1}0\}$ planes are shown in Fig. 4.7. Figures 4.8 and 4.9 show two views of the same model, emphasizing different features, directions, and planes.

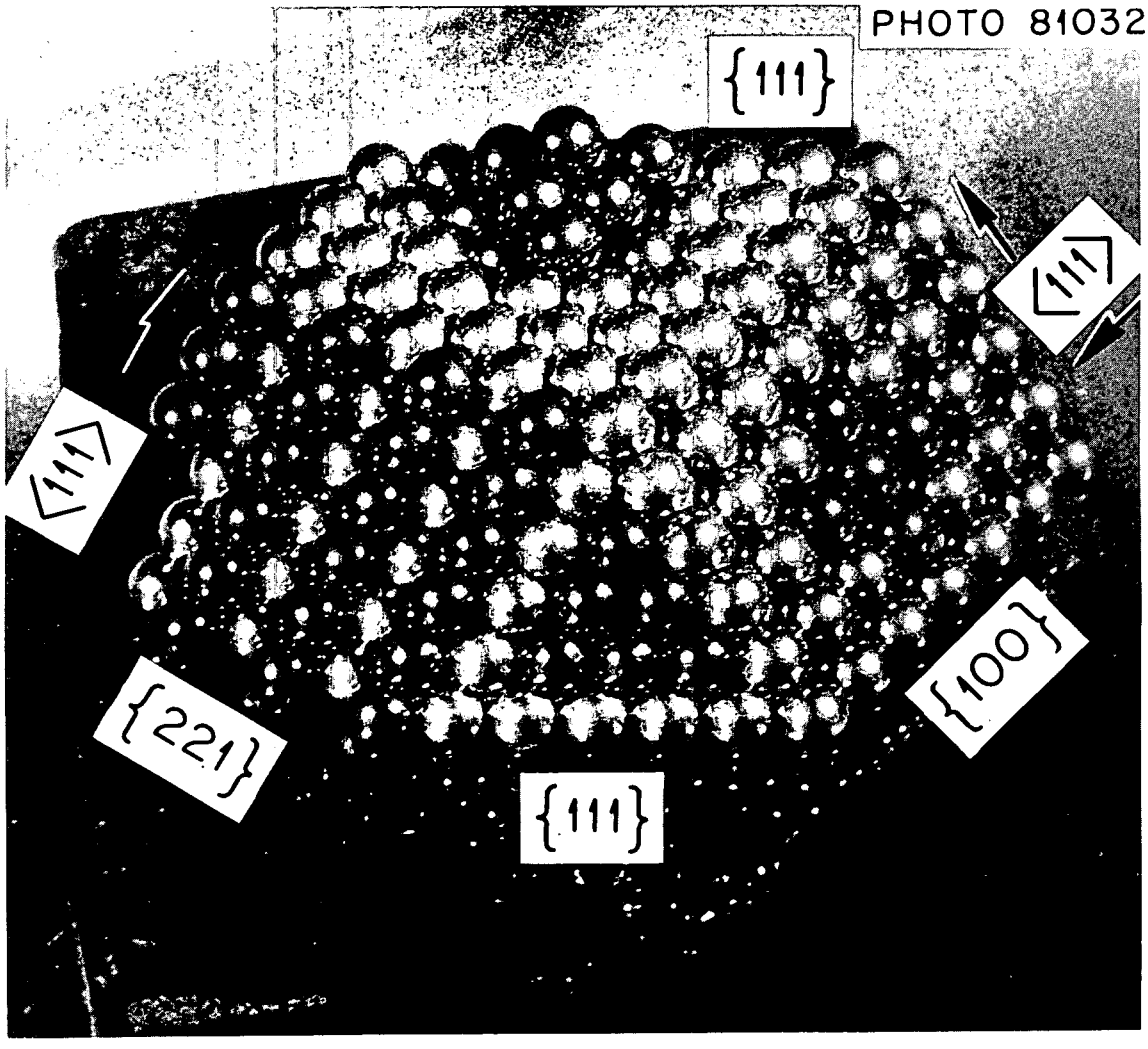

Fig. 4.6. Ball Model of Face-Centered Cubic Crystal Structure. Reduced 9.5% of original.

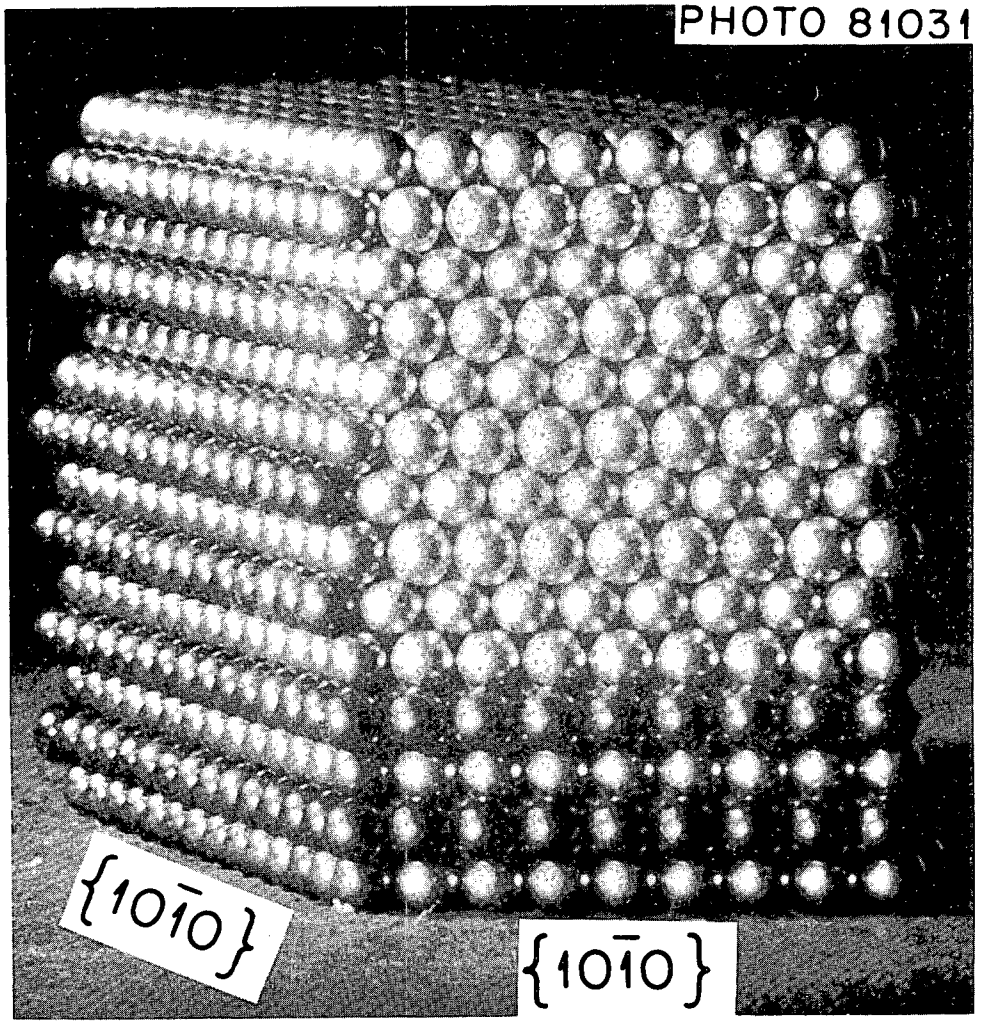

Fig. 4.7. Ball Model of Close-Packed Hexagonal Crystal Structure Showing {10$\bar{1}$0} Planes.

Shown in Fig. 4.8 are: (1) the {10$\bar{1}$2} twinning plane, (2) two ⟨11$\bar{2}$3⟩ directions on the {10$\bar{1}$1} plane, (3) the closed-packed hexagonal prism on the left side of the {10$\bar{1}$1} plane, and (4) side views of the {11$\bar{2}$1} and {11$\bar{2}$2} twinning planes. Shown in Fig. 4.9 are (1) a side view of the {10$\bar{1}$1} plane, and (2) front views of the {11$\bar{2}$1} and {11$\bar{2}$2} twinning planes, the colored balls showing the ⟨11$\bar{2}$3⟩ directions on these two planes. Such models can serve to emphasize such things as the multitude of slip systems available in zirconium alloys if the ⟨11$\bar{2}$3⟩ direction can be a slip direction.

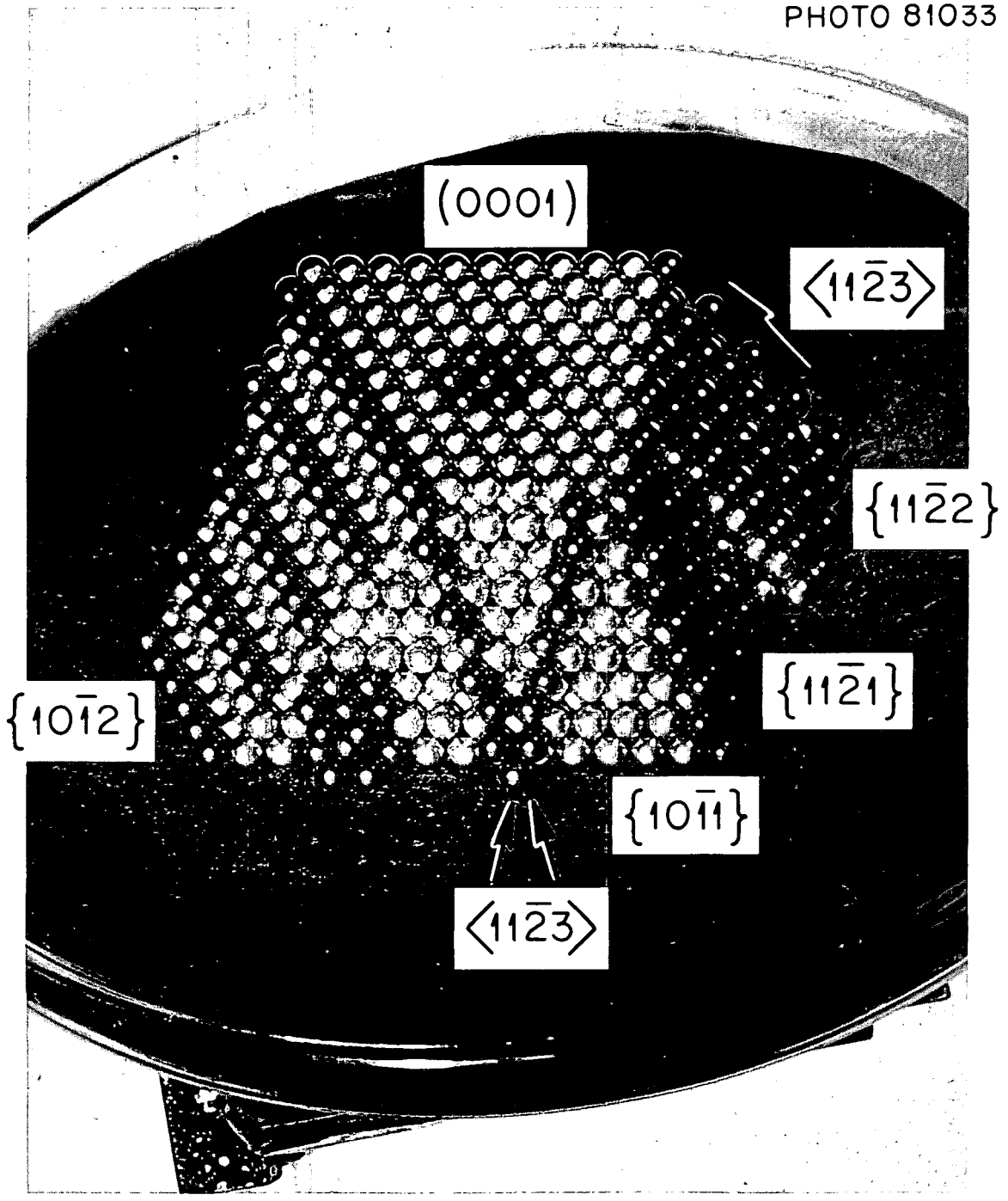

Fig. 4.8. Ball Model of Close-Packed Hexagonal Crystal Structure Showing {10$\bar{1}$2}, {10$\bar{1}$1}, {11$\bar{2}$1}, {11$\bar{2}$2}, and (0001) Planes and ⟨11$\bar{2}$0⟩ and ⟨11$\bar{2}$3⟩ Directions. Reduced 13% of original.

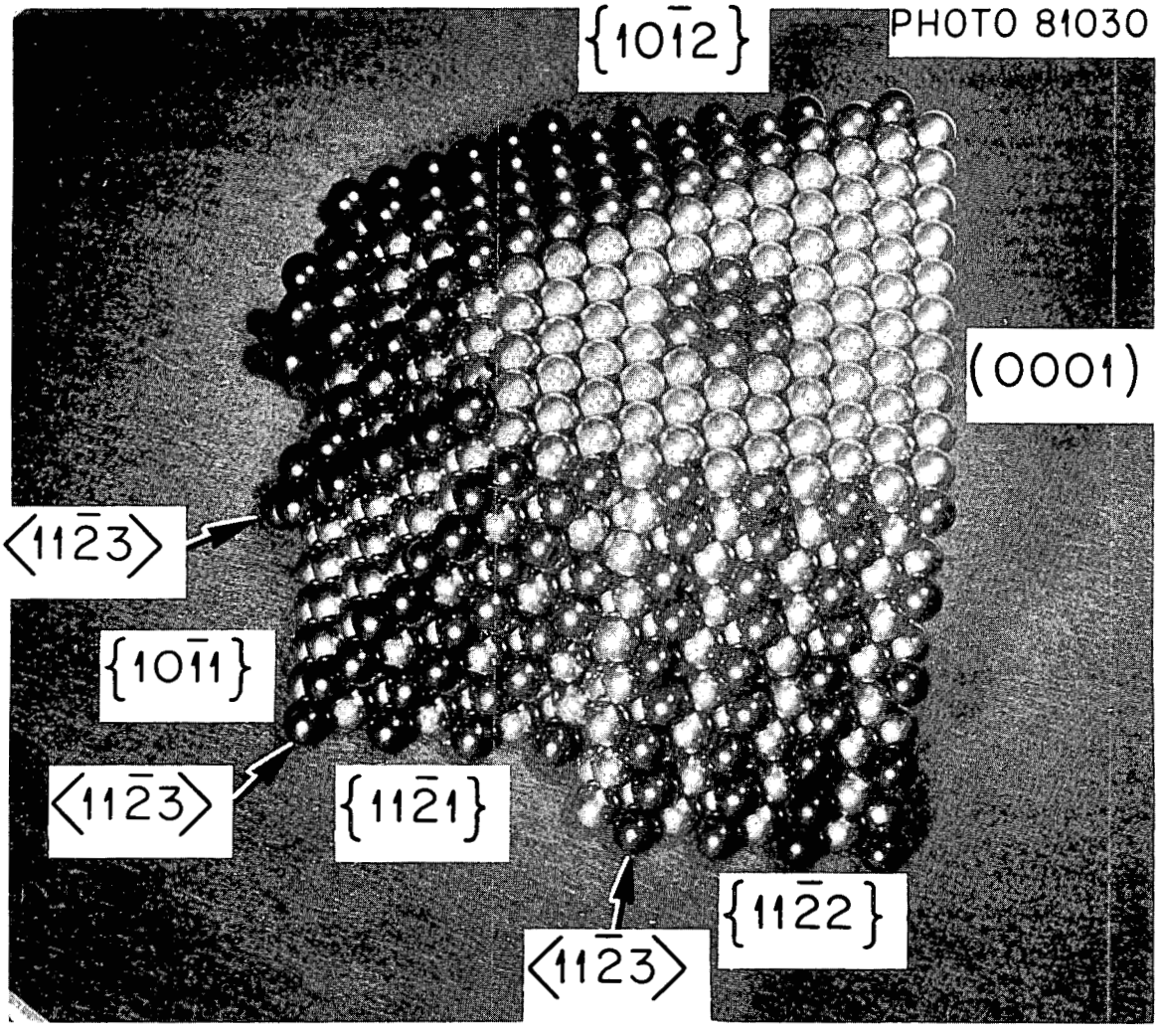

Fig. 4.9. Ball Model of Close-Packed Hexagonal Crystal Structure Emphasizing the Atom Arrangements on the {11$\bar{2}$1} and {11$\bar{2}$2} Planes. Reduced 13% of original

Certain observations reported in the literature indicate that ⟨11$\bar{2}$3⟩ can be a slip direction if there is sufficient restraint to plastic flow in the specimen.

Ball models of the twinning systems have been constructed, using plastic sheet to form the angle between the basal planes in the twin and the matrix. The models show graphically: (1) the strain present around the twinning plane, (2) that the twinning plane is primarily a mirror plane for atom positions located an appreciable distance from it rather than a mirror plane for the atoms that form

it and its immediate neighborhood, and (3) gives some indication of the amount of shuffling the atoms must undergo as the twinning plane moves through the lattice.

Defects and dislocations of various kinds, including stacking faults, are readily built into the model. Methods of applying force to the model are now being developed to determine the feasibility of watching atom movements during movements of such defects through the model.

Deformation Systems in Zirconium

M. L. Picklesimer J. C. Wilson

A single-crystal cube of iodide zirconium (one zone-melting pass) was compressed along the basal pole to provide a metallographic specimen with which the several techniques of twin identification and crystal orientation by microscopy could be checked and demonstrated. Five surfaces of the compressed specimen were examined after final metallographic preparation and twin trace angles, basal pole tilts[9] of both matrix and twins, and basal plane traces of both matrix and twins were measured. All twins found were identified positively as $\{11\bar{2}2\}$ twins, and the technique of grain orientation by polarized light microscopy[9] gave the same answer as to specimen orientation as did the more conventional techniques of using twin trace angles and a Wulff net and the trace angles on two intersecting surfaces.

A group of the $\{11\bar{2}2\}$ twins observed on one face of the compressed specimen are shown in Fig. 4.10. The specimen was rotated between the photographs at each magnification, so that twins and matrix can be definitely identified by a color change or a lack of it. The field of view shown in Fig. 4.10a and b is of the center twin intersection shown in Fig. 4.10c and d. This set of photomicrographs show second order twinning occurring in one of the $\{11\bar{2}2\}$ primary twins, and raises a question as to which twin was crossed.

---

[9]L. T. Larson and M. L. Picklesimer, Fuels and Materials Development Program Quart. Progr. Rept. June 30, 1965, ORNL-TM-1200, pp. 36–39.

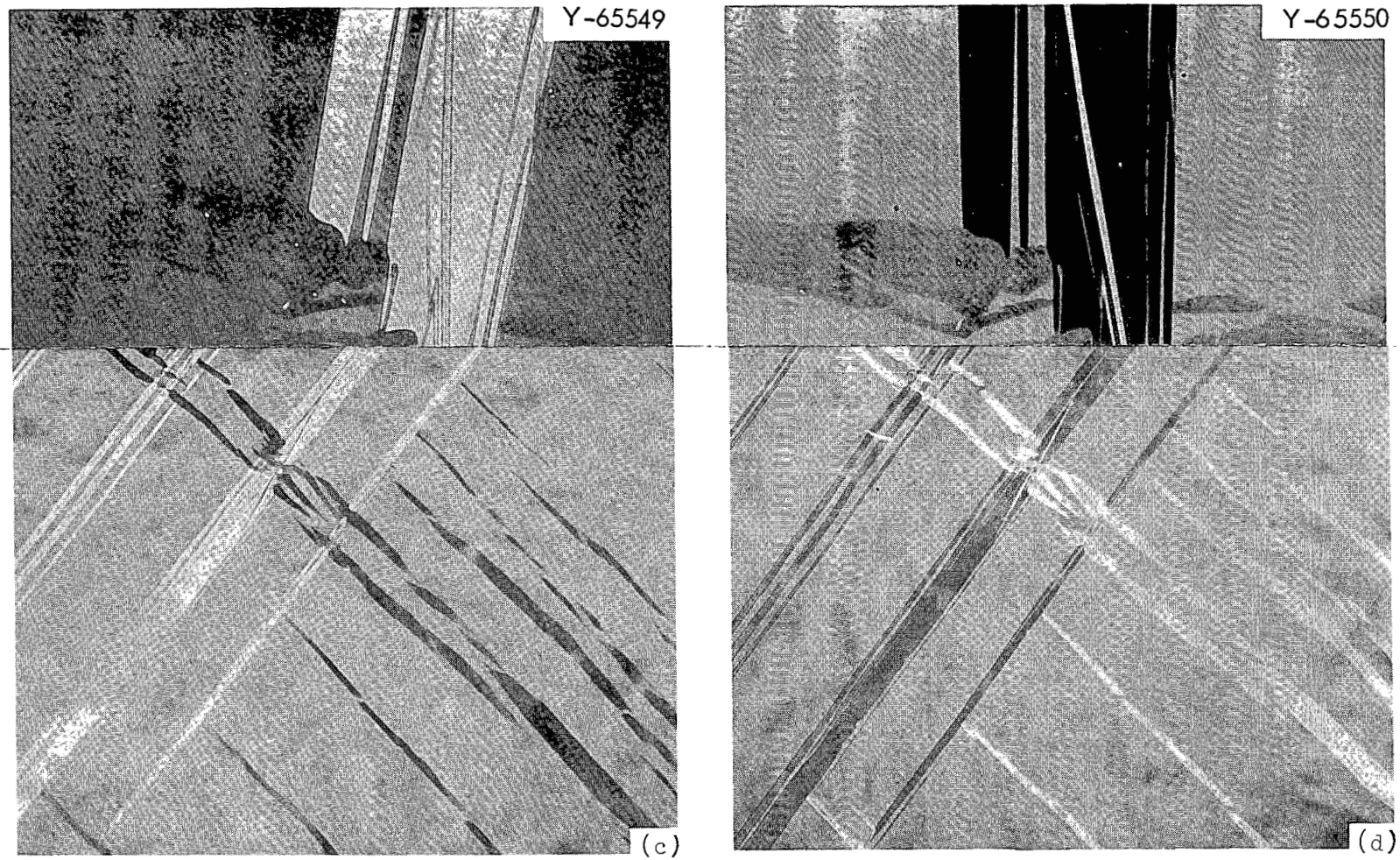

Fig. 4.10. Photomicrographs of {11$\bar{2}$2} Twins and Twin Intersections in a Single Crystal of Zirconium Compressed Along the Basal Pole Direction. (a) Main twin intersection seen in (a) and (b). 500×. (b) Polarized light rotated 90°. Same field as (d). 500×. (c) One orientation of polarized light. 75×. (d) Polarized light rotated 90°. Same field as (a). 75×.

OFFICIAL USE ONLY

Oxide Film Studies

J. C. Banter

The study of partially dissolved oxide films on zirconium has been extended to include films formed at 350°C in air and at 300°C in water. The optical absorption observed in the visible and ultraviolet regions of the spectrum in the as-formed thermal films[10] was enhanced by vacuum annealing even though the films were decreased in thickness only slightly. This indicates that the absorption in these films in the as-formed condition is equivalent to that observed in the same spectral region in the anodically formed films that had been vacuum annealed to partially dissolve them.[11] This absorption is attributed to the defects existing in the films, the most likely of which are oxygen-anion vacancies formed by oxide dissolution at the metal-oxide interface. Pemsler[12] has suggested that these vacancies condense at this interface at temperatures above 975°C to form voids, and that similar voids may form on a microscale at lower temperatures. The present results indicate that at even lower temperatures (400 to 600°C) these vacancies may condense along paths through the films, producing pores of sufficient size to allow bromine to penetrate to the underlying metal.[11] Such pores appear to be present in all vacuum annealed films, but there is no evidence of their presence in the as-formed thermal films despite the fact that such films exhibit the same type of absorption as the vacuum annealed anodic films.

These results are in agreement with the mechanism[12] suggesting that oxidation proceeds by the formation of oxygen-ion vacancies and free electrons at the oxide-metal interface by the oxide dissolution reaction. This is followed by diffusion of the vacancies and electrons

---

[10] J. C. Banter, Fuels and Materials Development Program Quart. Progr. Rept. March 31, 1965, ORNL-TM-1100, p. 37.

[11] J. C. Banter, Fuels and Materials Development Program Quart. Progr. Rept. June 30, 1965, ORNL-TM-1200, p. 39.

[12] J. P. Pemsler, J. Electrochem. Soc. 112, 447 (1965).

through the film to the oxide-oxygen environment interface. There they are consumed in the reaction whereby oxygen atoms enter the vacant lattice sites to reform stoichiometric oxide. This latter reaction could explain the lack of pores in the thermally formed films, since it would tend to act as a barrier to prevent their complete penetration through such films.

The need for further study of the relative contributions of oxygen dissolution and film formation processes to the overall oxidation mechanism is indicated. For this purpose, a special vacuum system is being built to be coupled to the spectrophotometer. This will permit reflection measurements to be made during vacuum annealing and oxidation experiments, either at temperature or at lower temperatures after heat treatment.

Attempts to measure the electrical conductivity of the oxide films on zirconium both before and after vacuum annealing have been unsuccessful because of electrical breakdown of the films when the equipment presently available is used. A variable range electrometer and associated equipment are being obtained which should allow conductivity measurements of the required kind to be made. It is expected that such measurements will give further insight into the electrical characteristics of the defects observed in the as-formed and vacuum annealed thermal films.

Preparation of Single Crystals of Zirconium and Zirconium Alloys

J. C. Wilson

Attempts to improve the yield and quality of zirconium single crystals by tilting the liquid-solid interface 30° from the horizontal were not successful. Aust and Chalmers[13] have used a similar method to reduce striations in metal crystals grown from the melt in a boat. We had expected that the grain boundaries, normally elongated in the direction of the bar axis, would tend to grow perpendicular to the

[13]K. T. Aust and B. Chalmers, Can. J. Phys. 36, 977 (1958).

liquid-solid interface and thus force most of the boundaries to grow out of the crystal. Experimentally, the boundaries tended to be parallel to the tilted liquid-solid interface.

Large grains (>3 mm in diameter) were grown in 0.3-mm-thick sponge zirconium strip by strain annealing. The critical strain was found to be about 2%, and the annealing time required was 30 hr at 830°C. Similar results are expected in experiments now under way using zone-refined sheet. The strain-anneal technique has not previously been very successful in zirconium and titanium because the nucleation of new grains occurred at twin intersections. This problem was prevented by using an initial grain size of less than 10 μ, a grain size small enough to essentially eliminate deformation by multiple and/or second order twinning.

Zone Refining of Zirconium

J. C. Wilson

A new cold trap and a variable speed drive were installed on the zone refining apparatus to allow refining overnight. We wish to determine if slower zoning speeds will result in better purification. The first experiments have been completed but the chemical analyses have not yet been obtained.

Preliminary tests have indicated that a commercial ion microprobe mass spectrometer using a small argon ion beam for sputtering of the specimen[14] may be usable to obtain analyses of the zone-refined zirconium with a sensitivity of 10 ppm or better over a mass range of 2 to 200 amu, at a cost of about $70.00 per specimen. Calibration standards are being made to permit a better examination of the possibilities of such an analytical technique for the high-purity materials we are producing. It also appears that analyses for carbon, nitrogen, and oxygen will be feasible. Comparison spectra will also be obtained with a spark-source mass spectrograph.

---

[14]Private communication from R. J. Gray and G. Hallerman, Metallography Group, to M. L. Picklesimer Sept. 8, 1965.

Several pounds of one-to-ten pass zone-melted zirconium rod stock have been produced for experiments within the program. Some of the 1/2- to 3/4-in.-diam rods have contained large single crystals of suitable size for machining 1/2-in.-diam spheres for oxidation and hydriding studies.

Properties of High-Purity Zirconium

J. C. Wilson

High-purity single-crystal specimens of zirconium are being used in several projects to obtain significant information with greater ease and accuracy. The present projects include oxidation of single-crystal spheres in air, determination of hydride habit planes, optical properties in single-crystal spheres, and studies of the modes of plastic deformation.

Oxidation

The first clear indication of the anisotropy of oxidation of zirconium as a function of crystal orientation was reported earlier[15] for films up to 500 A thick formed in air at 360°C. The work has been continued at 360 and 400°C to maximum film thicknesses of about 3400 A. The general pattern of oxidation previously described[15] has continued. The thicker films have shown that the rate of oxidation differs by at least a factor of 3 on different planes of the same crystal sphere. This has also shown that extreme care must be exercised in cutting flat single-crystal plates for detailed oxidation experiments, for there are several orientations where an error of 5° and less could cause a factor of 3 difference in the observed oxidation rates. These experiments have been carried out in an air furnace so arranged that the color changes over at least one (usually two) complete stereographic triangle can be observed continuously without interrupting the test.

---

[15]J. C. Wilson, Fuels and Materials Development Program Quart. Progr. Rept. March 31, 1965, ORNL-TM-1100, pp. 38–39.

We have observed small differences in the oxidation pattern and rate on crystallographically equivalent faces of the same crystal and in adjacent crystals in the same sphere. Similar differences are observed in the etch-pitting behavior. We suspect that the defect structure of the specimen may be slightly different for various planes that are members of the same family, depending on the details of how the alpha crystal transformed from the beta.

Hydrides in Zirconium

Zirconium hydride has been reported to precipitate on a number of planes in alpha zirconium. Babyak[16] has recently summarized the data available and has reported a distribution of hydrides among a number of crystallographic planes in the same specimen.

Hydrides have been observed on several of the single-crystal spheres prepared in our program. The principal habit plane observed has been $\{10\bar{1}0\}$, a few have been observed on the basal plane, and a few may have been on $\{11\bar{2}0\}$. Since all hydride habit planes are not observed on all spheres, purity or structure may influence the plane on which the hydride precipitates. We are presently determining the habit plane as a function of depth below the surface, oxygen contamination of the surface, and incomplete annealing after α-β-α cycling, using spherical single crystals.

A strong attack of the matrix next to hydride precipitates has been observed when an electropolishing solution described by Mills and Craig[17] is used for metallographic preparation of crystal bar zirconium. Deep grooves are observed in the matrix at large hydrides when the grain surface is a basal plane. Small precipitates, tentatively identified as hydrides, are also observed in the matrix between the large hydrides but oriented in $\langle 10\bar{1}0 \rangle$ directions. Hydride plates roughly

---

[16]W. J. Babyak, Hydride Habit Planes in Zirconium and in Unstressed and Stressed Zircaloy-4, WAPD-T-1757 (1965).

[17]D. Mills and G. B. Craig, "Etching Dislocations in Zirconium," paper presented at the Symposium of Zirconium and Its Alloys, 1965 Fall Meeting of the Electrochemical Society, Buffalo, New York, October 10–14, 1965.

parallel to the surface of the specimen were also revealed if they were no more than about 10 μ below the surface. This indicates that a local cell action is not responsible for the preferential attack of the matrix next to hydrides, but we do not as yet know whether local stress or some kind of segregation is responsible.

Plastic Deformation

The conditions leading to the development of a yield point in zirconium are being investigated. Tensile specimens of zone-refined and sponge zirconium have been tested at room temperature after annealing at 300 to 500°C. No yield points were observed. A point of inflection in the stress-strain curve was observed at the yield stress in the zone-refined material annealed at 300°C. Specimens will now be tested after annealing at lower temperatures.

An electroetching technique for developing dislocation etch pits in zirconium was described by Mills and Craig.[17] Using this technique, we have observed an increase in pit density in lightly deformed regions, and pits in patterns around hydride precipitates. Pit densities have often been observed to be greater by a factor of 10 to 100 at one grain boundary than at others in the same grain. These observations are consistent with the etch pits being developed at dislocations in the structures. The pitting is quite difficult to control, seeming to be strongly dependent on current density. Guard electrodes have been used, but even pitting over the face of a specimen has still not been obtained. The etch pits develop hexagonal shapes on basal planes, but the pit shapes on other planes have not yet been clearly defined, usually because the pit density was too great or the pits were not sufficiently developed. Etch-pitting studies will continue, for many studies of deformation in zirconium have been hindered by the lack of a technique for suitably revealing dislocations for optical examination.

PART II

REACTOR CHEMISTRY DIVISION

5. FISSION-GAS RELEASE AND PHYSICAL PROPERTIES OF FUEL MATERIALS DURING IRRADIATION

R. M. Carroll O. Sisman
R. B. Perez[1]

This is the second reporting of a program that is newly sponsored by the Reactor Fuels and Materials Development Branch. About five years ago, we began construction of an experimental apparatus to be used in the Oak Ridge Research Reactor to determine the diffusion coefficients of xenon and krypton in fuel materials while they were producing power. Our immediate goal was to obtain engineering measurements to fit into a formula that would describe the fission-gas diffusion through uranium dioxide. However, as the experiment progressed it became apparent that classical diffusion processes did not control the fission-gas release. In trying to discover the factors that do control the fission-gas release, our experimental approach has gradually changed from engineering tests to basic properties studies.

We do not yet have a finished equation for calculating the fission-gas release from UO_2, but a defect-trap model has been formed which qualitatively describes the mechanism of fission-gas release.[2] We will discuss the observations that led to the model, the experiments that have been made to test the model, and outline our current method of attack.

Mathematical Model[3]

The mathematical model describes a mechanism for the steady-state release of fission gas that fits the observations and conclusions in the previous report.[2] This is a rather oversimplified starting point from which further refinements may be made. For the present we will

---

[1]Consultant from the University of Florida.

[2]R. M. Carroll and O. Sisman, Fuels and Materials Development Program Quart. Progr. Rept. June 30, 1965, ORNL-TM-1200, pp. 55–64.

[3]R. M. Carroll, R. B. Perez, and O. Sisman, J. Am. Ceram. Soc. 48(2), 55–59 (1965).

consider that the clusters of defects (shown in Fig. 5.1) are quite permanent. That is, we assume that a fission product can escape from a point defect but has small probability of escaping from either the intrinsic defect or the clustered point defect trap, both of which we will treat as permanent traps. Note that an atom of gas born deep in the specimen has a high probability of falling into a permanent trap, and that only the gas that is born near the specimen surface has a high probability of escape.

We will, then, treat the knockout release separately and restrict the model to the consideration of the temperature-dependent gas-release

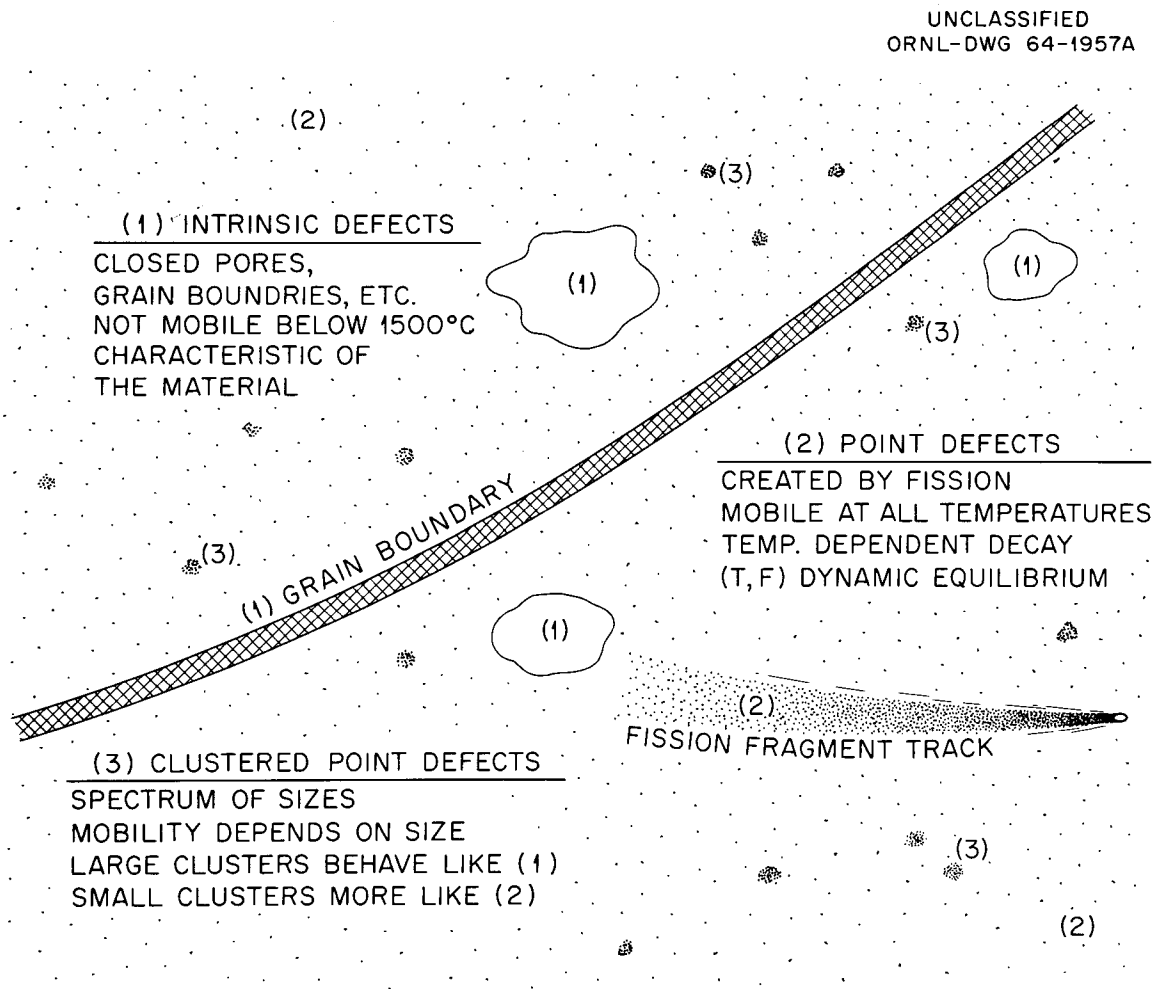

Fig. 5.1. Defect-Trap Characteristics.

processes, where large (permanent) and small (temporary) traps retard the escape of the fission gas. The small (type 2) traps reach a quick production-anneal equilibrium for a given fission rate and temperature. The fission products in a small trap have a probability of escaping the trap, but those in a large trap have a vanishingly small escape probability. Fission fragment tracks will create point defects in their wake and at the same time destroy any point defect traps in their path.

The mechanisms of trapping and release from traps are introduced by defining two parameters:

g = probability of trapping (sec^{-1})

b = probability of escape from trap (sec^{-1})

The other symbols to be used are:

M,H = density of mother, daughter isobars, respectively ($atoms/cm^3$)

r_o = the fractional probability that a trapped mother atom will escape the trap because of recoil energy when the mother decays into the daughter isobar

M_{tr},H_{tr} = concentration ($atoms/cm^3$) of mother, daughter isobars in traps

D = diffusion coefficient (cm^2/sec)

F = fission rate (fissions cm^{-3} sec^{-1})

E_X = activation energy for process X

R = gas constant

T = absolute temperature, °K

R_H = release rate of daughter isobars from the specimen per unit area

β_x = fission yield of isotope x

ϕ = neutron flux (neutrons cm^{-2} sec^{-1})

λ_x = decay constant of isotope x (sec^{-1})

Σ_f = macroscopic fission cross section (cm^{-1})

The hypothesis is made that the trapping probability is proportional to the fission density. In the expression

$$g = g_o + g_T\,(F,T) \quad , \tag{1}$$

the term g_o will account for both the presence of the intrinsic trap population and the traps produced by condensation of the point defects. The $g_T(F,T)$ term of Eq. (1) states that the population of point defects is a function of fission density and specimen temperature.

The gas trapped in the point defects can also escape by tunneling through the potential barrier created by the defect. This tunneling process is governed by an Arrhenius factor, and can be expressed as

$$b = b_o \exp\ (-\Delta E_b/RT) \qquad (2)$$

where ΔE_b is the activation energy of the tunneling process. Under the hypothesis of a diffusion mechanism coupled with radioactive decay and a trapping-release mechanism, the equations for the transport of the parent-daughter isobars can be easily written by making use of the principle of the conservation of particles.[3]

The equation giving the release rate of an inert-gas isotope is shown in Fig. 5.2, along with the simplifying assumptions for this first model. The constant R_H^o is the knockout yield in atom-centimeters per fission.

UNCLASSIFIED
ORNL DWG. 64-7441

Release Rate of Gaseous Daughter, $R_H = R'_H(T,F)\, e^{-\Delta E/2RT} + R_H^0 F$

$$R'_H(T,F) = F\sqrt{\frac{D_0}{\lambda'_H}}\left\{\beta_H + \left(\frac{\lambda_M}{\lambda'_M}\right)\left(\frac{W\beta_M}{1+(\lambda'_H/\lambda'_M)^{1/2}}\right)\right\}$$

$$\lambda' = \lambda\left[1+\left(\frac{g_0 + g_T F e^{\Delta E_g/RT}}{\lambda + b_0 e^{-\Delta E_b/RT}}\right)\right], \quad W = 1 + \left[\frac{g_0 + g_T F e^{\Delta E_2/RT}}{\lambda_M + b} r_0 + (1-r_0)\frac{b}{\lambda_H + b}\right]$$

SIMPLIFYING ASSUMPTIONS

(1) No change of microstructure

(2) Release by recoil is not temperature dependent

(3) Trapping probability of intrinsic and cluster traps is constant with time.

(4) Mother-daughter are affected the same by the traps.

(5) Diffusion of point defects are neglected.

(6) Homogenous distribution of traps.

Fig. 5.2. A Mathematical Model for Mother-Daughter Release.

Oscillating Experiments

In order to more fully exploit the defect-trap theory and to evaluate the various factors in the equations, we have modified the experiment so that it can now be operated in a dynamic mode. These changes make it possible to oscillate either the neutron flux or the temperature in a controlled fashion. By studying the amplitude and phase shift of the fission-gas release under various input conditions, we hope to develop our defect-trap model for fission-gas release and to experimentally establish the parameters (D_o, g_o, g_t, b_o, r_o, ΔE_g, ΔE_b) in the mathematical model.

The fission gas released from the specimen during irradiation is monitored continuously by a gamma-ray spectrometer. By appropriate settings of the spectrometer controls, the variation in the emission rate of a single isotope can be recorded over a period of time. A record of the flux or temperature variations during this same period of time is kept by a digital recording voltmeter.

Following the installation of the oscillating equipment, single-crystal specimens were irradiated. The specimens were sliced from the same crystal as some of the previous specimens but were polished to a metallographic finish before irradiation (the previous specimens had a ground finish). The surface of a specimen with the ground finish had become smoother during irradiation, and we believe this smoothing may have caused the observed reduction in fission-gas-release rate as burnup progressed.[4] We wished, therefore, to see if a specimen that was smooth at the beginning of irradiation would show this change. Analysis of the data indicates that the gas release from the polished specimen did not decrease with time. Also, the recoil release, which is associated with total surface area, was about the same for both specimens after irradiation smoothing had occurred. This observation substantiates our belief that irradiation smoothing influences the fission-gas release.

---

[4]R. M. Carroll and O. Sisman, Nucl. Sci. Eng. 21, 47–58 (1965).

Fission-Rate Oscillations

We have already demonstrated in the steady-state experiments that the fission-gas release below 600°C is independent of temperature and directly proportional to fission rate. We have shown that this low temperature release is by knockout rather than direct recoil.[2] Further confirmation of this theory is found in the results of oscillating the neutron flux while holding the specimen at a constant 575°C temperature. The data of Fig. 5.3 show that the ^{88}Kr release is proportional to fission rate but that the gas-release oscillations are not instantaneous with fission-rate oscillations. Gas release by recoil would be instantaneous while a knock-out release would depend on concentration of fission gas at the surface of the specimen as well as fission rate. Thus, this phase shift supports the contention that the low-temperature release is predominately by a knockout process.

The X marks on the time-flux plot of Fig. 5.3 show when samples of fission gas were taken for a quantitative analysis. The amount of ^{88}Kr released during this flux oscillation is shown in Fig. 5.4. The striking feature of Fig. 5.4 is that the amount of ^{88}Kr released during the oscillation is greater when the flux is decreasing than when the flux is increasing. The data form a sort of hysteresis curve (Fig. 5.4), which may be explained also on the basis of gas released by a knockout process. Our reasoning is that the amount of knockout is the product of the surface concentration of fission gas and the recoil rate. Naturally, the production of the fission gas is proportional to the fission rate and a greater concentration exists on the specimen surface after the specimen has passed through the high-flux region. This concentration is depleted while passing through the low-flux region and, for a given neutron flux, less fission gas is knocked out when the flux is increasing from a minimum value than when the flux is decreasing from a maximum value. Direct recoil release would yield the same amount of ^{88}Kr for the same neutron flux regardless of the past history of the specimen.

Another facet of Fig. 5.3 is that the release during the dynamic operation is much greater than the release during steady-state operation;

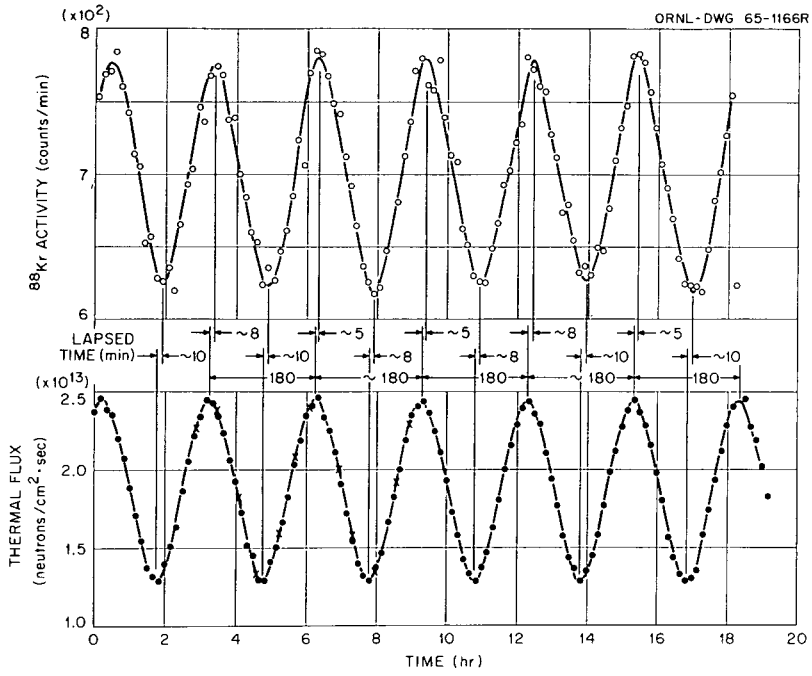

Fig. 5.3. Uranium Dioxide Single Crystal, C1-13-9-29, 3-hr Flux Cycle, 575°C.

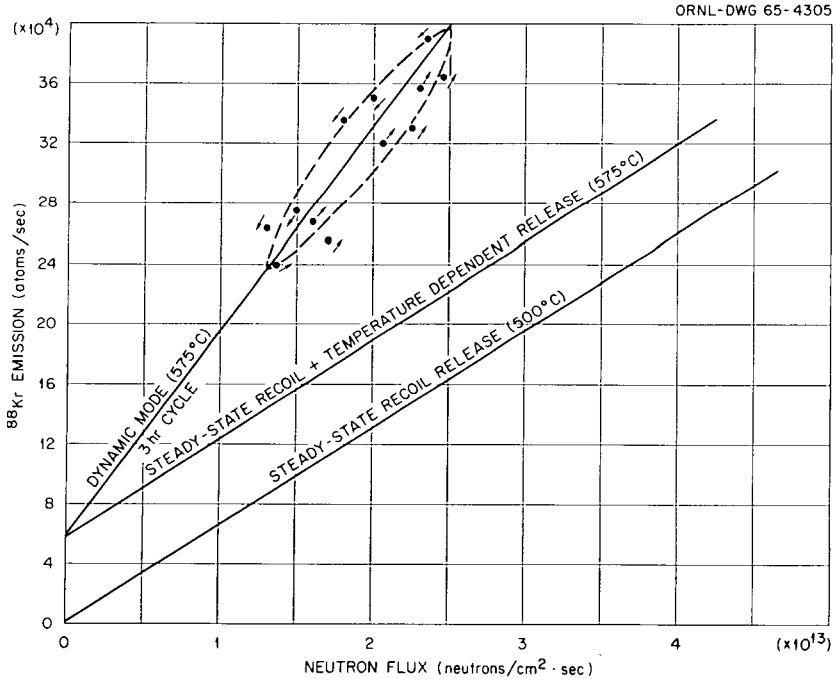

Fig. 5.4. Uranium Dioxide Single Crystal.

about 2.5 times as much. However, some of the release during dynamic operation is caused by the temperature-dependent contribution. If the temperature-dependent contribution is subtracted, the release rate during oscillation is still double the steady-state release rate for the same flux.

We think the larger release rate during the oscillation of flux is because the trap population is oscillating. The number of traps is greatest just after the neutron flux is maximum. As the flux decreases, the annealing rate of the traps exceeds the production rate and the trap population declines. Fission gas escaping the traps can migrate to the UO_2 surface and be available for knockout. When the flux is increasing, the trap production exceeds the annealing rate and the trap population increases. The increasing trap population is, however, offset by the increased production rate of the fission gas and the amount of fission gas arriving at the specimen surface will not be greatly different from the steady-state operation.

The specimen used to obtain these data was a polished single crystal of UO_2. However, the surface of any specimen is a grain boundary, and by our model, this is a deep trap for fission gas. Thus, this cyclic, point-defect annealing will deliver additional gas in surges to the specimen surface where it is trapped. The maximum rate of delivery will be during the flux decrease and therefore will account for some of the observed hysteresis. The net effect, however, will be to increase the total amount of fission gas at the specimen surface available for knockout as compared to steady-state operation. Thus, the data from Figs. 5.3 and 5.4 support the defect-trap model.

When the neutron flux was oscillated while the specimen temperature was above 600°C, we noticed that the fission gas was released in a more complex form. One such measurement, a 10-hr cycle while the specimen was at 840°C, is illustrated in Fig. 5.5. We think that the flux peak results in a maximum in the knockout release that has a delay time of about 20 min. The small activity peak, about 200 min after the flux peak, is the result of the changing trap population on the temperature-activated release.

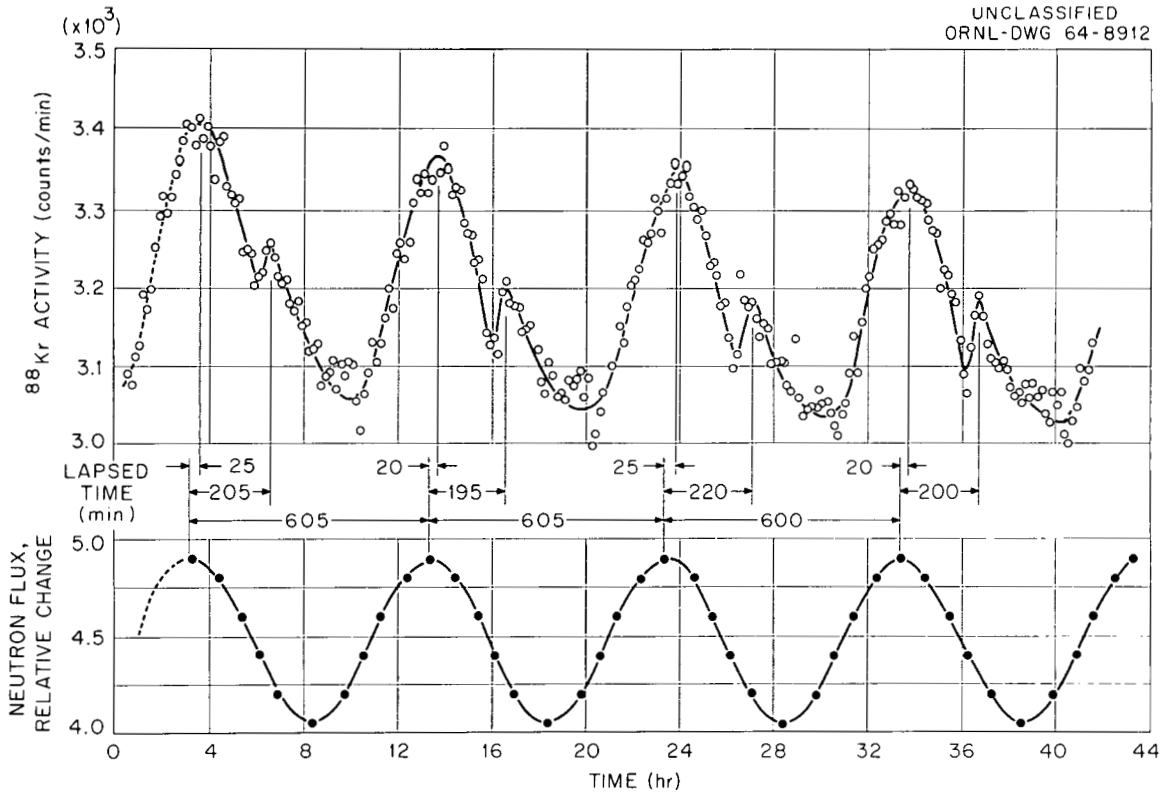

Fig. 5.5. Uranium Dioxide Single Crystal, C1-13-8-8, 10-hr Flux Cycle, 840°C.

Recall that the temperature-dependent fission-gas escape rate did not change much when the specimen was irradiated at constant temperatures but different flux levels. The data in Fig. 5.5 do show a change. The recoil process will account for the large peak, and we think the small peak is caused by the annealing of traps that were created during the times of maximum fission rate. In any event, the entire variation of gas release in Fig. 5.5 is only about 5% of the release rate, while the precision of the steady-state measurements is about 10% and would not have detected this change.

Temperature Oscillations

When the specimen was maintained at a constant fission rate and the temperature was cycled we observed a large, but smooth, osicllation of fission-gas release rate (see Fig. 5.6). However, the maximum release rate occurred about 10 min before the specimen reached

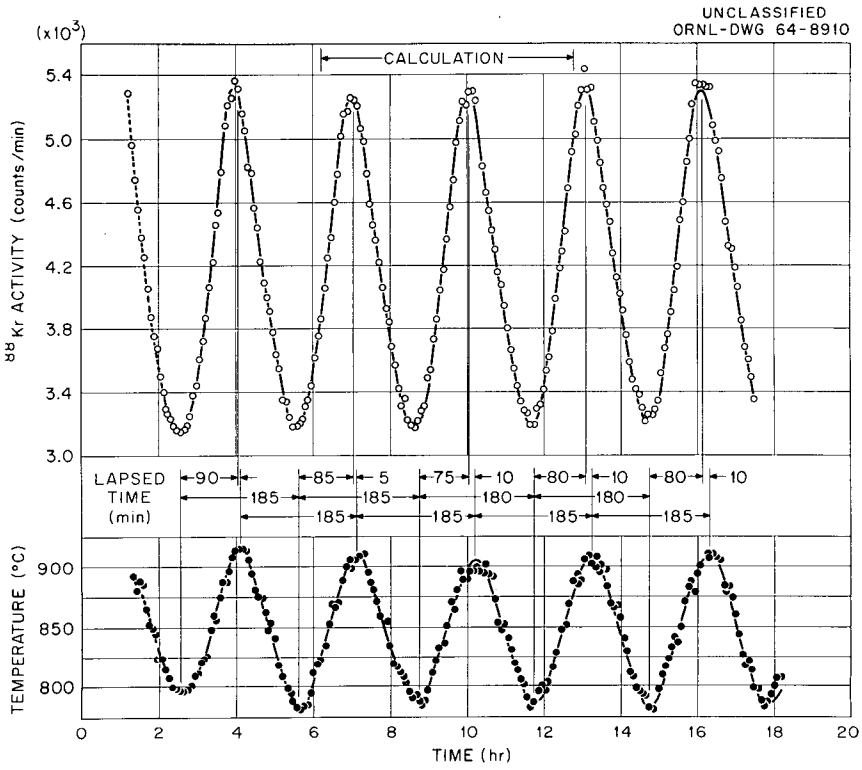

Fig. 5.6. Uranium Dioxide Single Crystal, C1-13-8-17, 3-hr Temperature Cycle; $\phi = 5.3 \times 10^{13}$ neutrons cm^{-2} sec^{-1}.

its maximum temperature, while gas release and temperature reached minimum values at the same time. By the defect-trap model we observed that gas that is trapped at the lower temperatures is being released as the temperature increases, thus producing more gas release at a given temperature on the heating cycle than on the cooling cycle. This would result in a maximum gas-release rate before the maximum temperature was obtained.

A diffusion model predicts an out-of-phase gas release in somewhat the same manner except that the minimum gas release should also be out of phase by the same amount. Therefore, we think this result is further confirmation of the defect-trap model.

The fission-gas release waves were analyzed in terms of their Fourier components, yielding amplitude and phase information as a function of frequency. This analysis compared the steady-state release rate (at zero frequency) with that at different frequencies. The gas release was found to increase as the frequency of oscillation

increased and at very slow oscillations the release approached steady-state levels. This result is consistent with the results in Fig. 5.4 and with those predicted for the defect-trap model by Perez;[5] namely, that as the oscillation frequency increases, the frequency-dependent factors overcome the trapping effect and the release approaches a diffusion mode, thus resulting in an increase of gas release.

---

[5]R. B. Perez, Trans. Am. Nucl. Soc., 8(1), 22–23 (1965). To be published in Nuclear Applications.

PART III

SOLID STATE DIVISION

6. IRRADIATION EFFECTS ON ALLOYS AND STRUCTURAL MATERIALS

D. S. Billington M. S. Wechsler

The research of the Radiation Metallurgy Section of the Solid State Division, reported herein, encompasses two aspects of radiation effects on metals and alloys: the effect of radiation on metallurgical reactions in alloys and on plastic deformation and fracture. The major emphasis is on body-centered cubic metals, although our studies of segregation in copper-nickel alloys and of the tensile properties of nickel are exceptions. There are several reasons for this emphasis on body-centered cubic metals. For one thing, radiation damage in body-centered cubic metals has been studied much less thoroughly than in face-centered cubic metals in the past, although, of course, the body-centered cubic metals have as much basic significance. Now that it is possible to prepare purer and better characterized samples of body-centered cubic metals, particularly iron and the refractory metals, it seems appropriate to pursue radiation damage studies on these materials to a greater extent.

Another motivation for studying the body-centered cubic metals stems from more practical considerations. The problem of the embrittlement of pressure vessel steels continues to lend concern over the safety of reactor pressure vessels. The problem has its origin in the phenomenon of low-temperature brittleness to which the body-centered cubic metals are susceptible. Therefore, continued effort to better understand the processes of flow and fracture in these metals is required. As is described, the activities of the Radiation Metallurgy Section in this area includes rather fundamental work, such as plastic deformation and etch pitting in single crystals of niobium and stress relaxation measurements of dislocation dynamics in iron, and somewhat more applied work on the tensile properties of irradiated iron and nickel. Finally, the Section has responsibilities for several reactor pressure vessel surveillance programs and in this work irradiations and tests on commercial steels are required.

To increase the effectiveness of the research, several new facilities, chiefly for the Bulk Shielding Reactor, have been installed or are being constructed or designed. These include an irradiation chamber at the northwest corner of the BSR (now in operation), a liquid-nitrogen-cooled cryostat for operation at the edge of the reactor (almost completely constructed), and a neutron convertor facility for irradiations in a high-purity fission flux (under design).

Effect of Irradiation on Precipitation of Nitrides in Alpha Iron

J. T. Stanley W. E. Brundage

In recent months our study of the iron-nitrogen system has concentrated on the trapping of radiation produced defects by nitrogen atoms. This work was motivated by the results of the Brookhaven group on the iron-carbon system. Damask and Wagenblast[1] interpreted their internal friction measurements in iron-carbon specimens as showing that in heavily irradiated specimens carbon atoms diffuse to vacancies and form complexes that are stable to about 250°C. Subsequently, results of electrical resistivity,[2] calorimetric,[3] and electron microscope[4] measurements were presented to confirm this model. Finally, calculations were made by Johnson[5] using the results of Damask and co-workers to devise an effective carbon-iron interaction potential. Johnson then used this interaction potential to calculate certain properties of the iron-carbon

---

[1]H. Wagenblast and A. C. Damask, "Kinetics of Carbon Precipitation in Irradiated Iron," Phys. Chem. Solids 23, 221–27 (1962).

[2]F. E. Fujita and A. C. Damask, "Kinetics of Carbon Precipitation in Irradiated Iron – II Electrical Resistivity Measurements," Acta Met. 12, 333–39 (1964).

[3]R. A. Arndt and A. C. Damask, "Kinetics of Carbon Precipitation in Irradiated Iron – III Calorimetry," Acta Met. 12, 341–45 (1964).

[4]H. Wagenblast, F. E. Fujita, and A. C. Damask, "Kinetics of Carbon Precipitation in Irradiated Iron – IV Electron Microscope Observations," Acta Met. 12, 347–53 (1964).

[5]R. A. Johnson, G. J. Dienes, and A. C. Damask, "Calculations of the Energy and Migration Characteristics of Carbon and Nitrogen in α-Iron and Vanadium," Acta Met. 12, 1215–24 (1964).

system. Many of the calculations showed good agreement with experiment. The calculations led Johnson to predict that a nitrogen atom in iron would be bound to a vacancy with about the same energy as a carbon atom.

In our experiments with neutron irradiated iron-nitrogen alloys, we were unable to obtain results that indicated a comparable trapping of nitrogen atoms by vacancies.[6] In general we did not irradiate to doses high enough to produce the trapping reaction. More recently, using electron irradiations we have been able to produce defect concentrations comparable to the nitrogen atom concentrations, and we have observed a phenomenon that may be due to the trapping reaction.

Review of Experimental Procedures and Previous Results

In the experiments on the iron-carbon system and on the iron-nitrogen system, measurements were made on highly supersaturated solid solutions prepared by quenching from higher temperatures to room temperature. In both systems the supersaturated solid solutions decompose into precipitates, but the solubility of the nitride is considerably higher than the solubility of the carbide. In each system internal friction measurements give a sensitive and specific indication of the amount of carbon or nitrogen in solution in iron in the regular interstitial position, which is the octahedral site of the iron lattice. Experiments have established that neutron irradiation can enhance the rate of formation of the carbide[1] and the nitride.[6] Our experiments have indicated that electron irradiation cannot enhance the rate of metastable nitride precipitation and, in fact, may slow it down. The enhanced rate of precipitation upon neutron irradiation is almost certainly due to formation of nucleation sites for the precipitation, but the nature of these nucleation sites is not known.

---

[6]J. T. Stanley, "The Effect of Irradiation on Precipitation of Nitrides in Iron," pp. 349–56 in Diffusion in Body Centered Cubic Metals, The American Society for Metals, Metals Park, Ohio, 1965.

Interaction Between Point Defects and Nitrogen Atoms in Iron

Recently we have found that when iron-nitrogen specimens are irradiated with 2-Mev electrons at low temperatures to doses sufficient to produce defect concentrations equal to the concentration of nitrogen atoms in solution, a certain fraction of the nitrogen atoms disappears from solution at a temperature below 35°C. These nitrogen atoms are presumably trapped by radiation produced defects. In experiments to date it was found that when the calculated Frenkel defect concentration was equal to the nitrogen atom concentration about 16% of the nitrogen atoms were trapped, and when the Frenkel defect concentration was double the nitrogen atom concentration about 38% of the nitrogen atoms were trapped. Figure 6.1 shows the results of experiments that suggest that this trapping reaction occurs. For the measurements represented by steps 4 and 9 in Fig. 6.1, the sample was irradiated at low temperatures with essentially all of the nitrogen in solution. The sample was then removed from the irradiation apparatus and placed in the measuring apparatus. Measurements were made at approximately 10°C temperature intervals up to 65°C. The measurements even at the low temperatures show a decrease in the amount of nitrogen remaining in solution after the irradiation. In the case of the smaller dose irradiation the fractional decrease in internal friction at each temperature is constant. This fact indicates that trapping occurs below 25°C. However, for the higher dose irradiation the fractional decrease is not as great for the two lowest temperature measurements as for the higher temperature measurements. The significance of this last observation is not known at present.

Internal friction measurements upon solution annealing of the electron-irradiated iron-nitrogen sample have established the approximate temperature at which nitrogen atoms are released from their traps. Following step 4, Fig. 6.1, the sample was aged at 65°C to precipitate the remaining nitrogen as Fe_8N (step 5). The sample was then solution annealed at 370°C. Step 6, Fig. 6.1, shows that the level of free nitrogen returned to the value it had after the electron irradiation, which indicates that the solution anneal at 370°C redissolved the Fe_8N precipitate but did not release nitrogen from the radiation-produced traps.

ORNL-DWG 65-7021

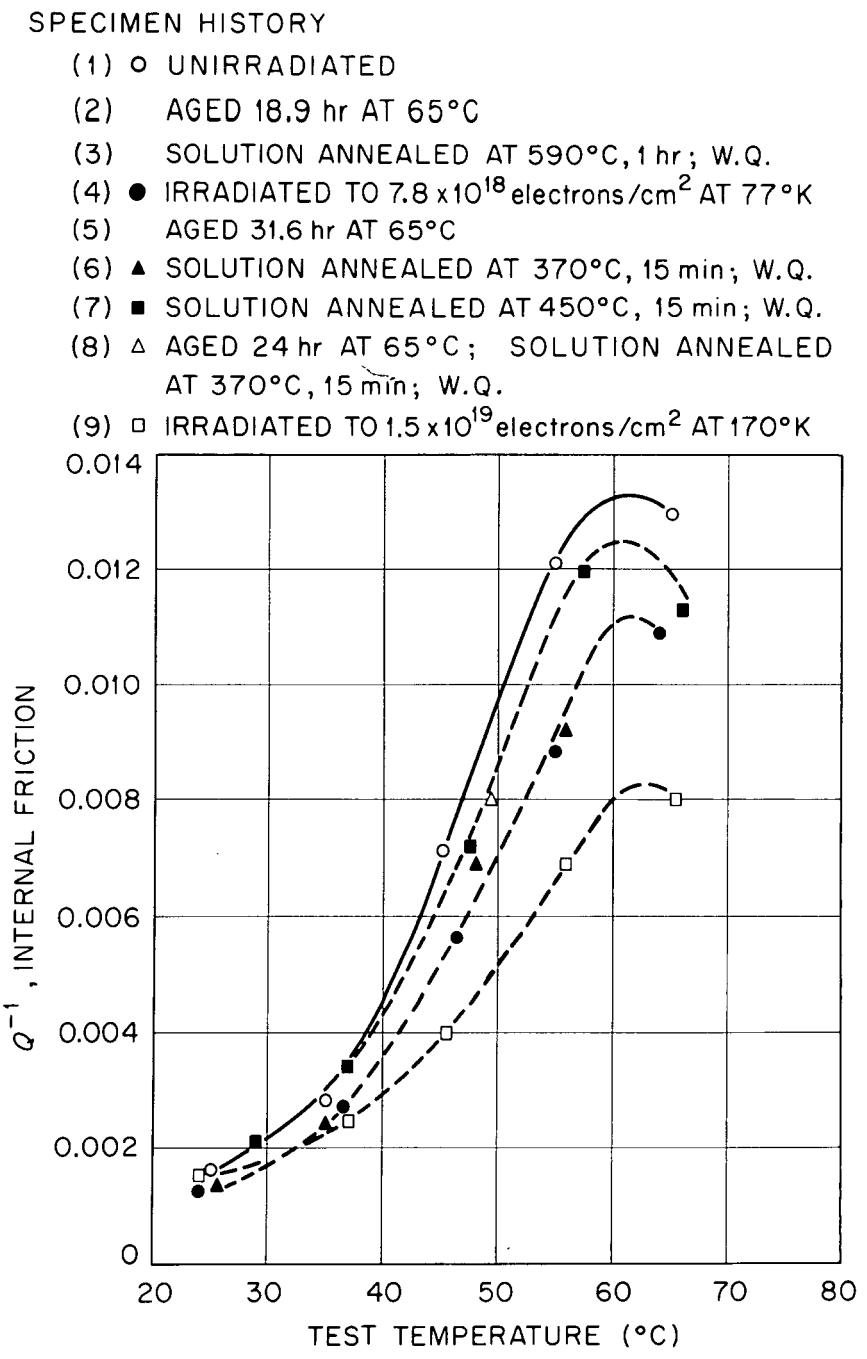

Fig. 6.1. Effect of 2-Mev Electron Irradiation on the Nitrogen Internal Friction Peak in Fe—0.013 wt % N. Frequency: 35 cps. Initial condition: solution annealed at 590°C for 2 hr and water quenched (W.Q.).

Then a solution anneal at 450°C was applied (step 7). This time the concentration of free nitrogen increased almost to its value before irradiation (filled squares, Fig. 6.1). Thus, for the irradiation at 77°K to 7.8×10^{18} electrons/cm^2, the trapped nitrogen was released between 370 and 450°C. Another aging at 65°C and solution annealing at 370°C (step 8 and open triangle, Fig. 6.1) gave the same concentration of free nitrogen as after the solution anneal at 450°C.

We have seen that the irradiation to 1.5×10^{19} electrons/cm^2 at 170°K produced a decrease of about 38% in the internal friction peak due to free nitrogen (open squares, Fig. 6.1). This suggests that 38% of the nitrogen atoms were trapped by radiation-produced defects. This nitrogen-defect complex may be expected to introduce a new internal friction peak. If the relaxation strength of the complex were equal to that for the free nitrogen, the additional peak would have a height of about 5×10^{-3}. Therefore, following the internal friction run shown in Fig. 6.1, a search was made for an additional peak by making internal friction measurements at temperatures from −200 to 300°C. Figure 6.2 shows that no peak (other than the peak at 65°C due to free nitrogen) of

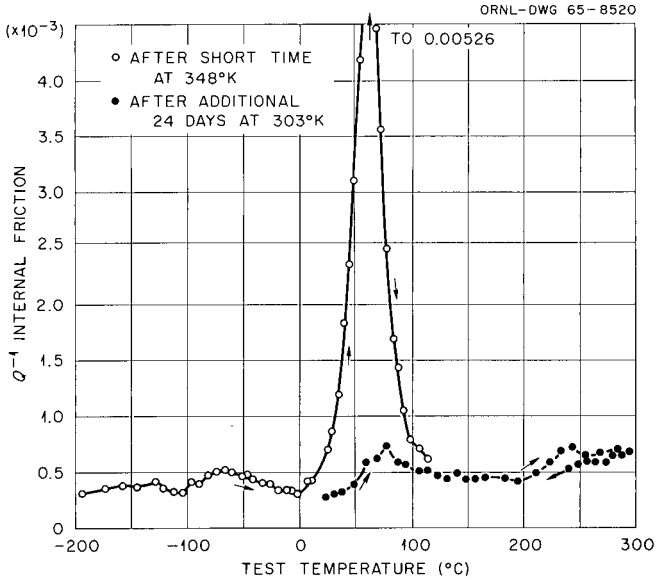

Fig. 6.2. Internal Friction of an Fe–0.013 wt % N Sample Following Electron Irradiation at 1.5×10^{19} electrons/cm^2 (E = 2 Mev) at 170°K.

the expected magnitude was detected. It may be that the relaxation strength of the complex is much smaller than for free nitrogen. Another possibility is that by the time the measurements of Fig. 6.2 were made, many types of complexes had formed containing various numbers of defects and nitrogen atoms. In this case, a larger internal friction peak due to trapped nitrogen might be observed at an earlier stage in the trapping.

In the next series of measurements, the temperature range for the release of nitrogen atoms from traps following the irradiation to 1.5×10^{19} electrons/cm^2 was determined in a manner similar to that described above for the irradiation to 7.8×10^{18} electrons/cm^2. However, because of the intervening treatment (Fig. 6.2) the sample probably contained some Fe_4N precipitate. The sample was solution annealed and quenched from temperatures from 580 to 660°K (315 to 385°C). The internal friction measurements at 65°C (Fig. 6.3) indicate that the

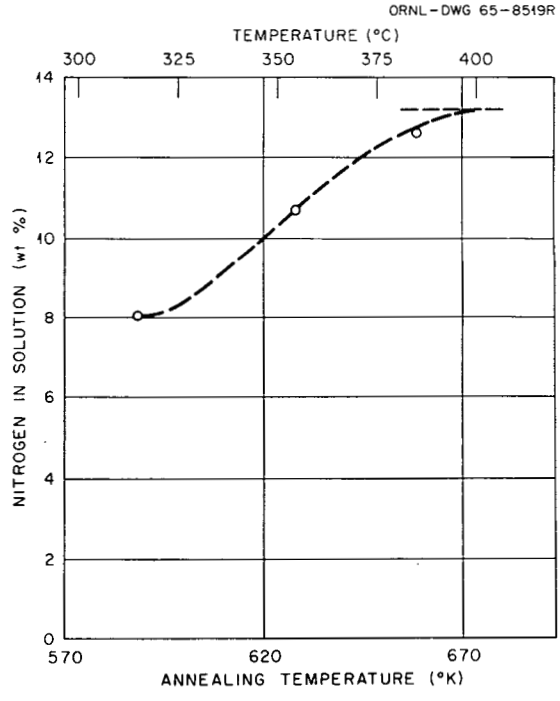

Fig. 6.3. Re-Solution of Nitrogen in Fe–0.013 wt % N upon Isochronal Annealing (t = 15 min) Following Electron Irradiation to 1.5×10^{19} electrons/cm^2 (E = 2 Mev) at 170°K.

trapped nitrogen in this case was released between 315 and 385°C, which is above the temperature for re-solution of the Fe_4N precipitate.

Finally we have made some isothermal aging experiments at 65°C to see the effect of large electron doses on the kinetics of precipitation of Fe_8N. These results are shown in Fig. 6.4 for the sample before irradiation and after irradiation at 77°K with 7.8×10^{18} electrons/cm^2. The effect of the electron irradiation is to slow down the precipitation. There are two possible explanations for the observed retardation of Fe_8N precipitation: (1) After electron irradiation there is less nitrogen in solution so that a smaller number of nitride particles are nucleated. (2) The nuclei for nitride precipitation are impurity atoms and the vacancies created by the irradiation allow these impurity atoms to diffuse and agglomerate so that the number of nuclei is decreased.

The results of our experiments are summarized in Fig. 6.5, which is a schematic diagram of an assumed isochronal annealing experiment on an iron-nitrogen sample irradiated at about 170°K to an electron dose of

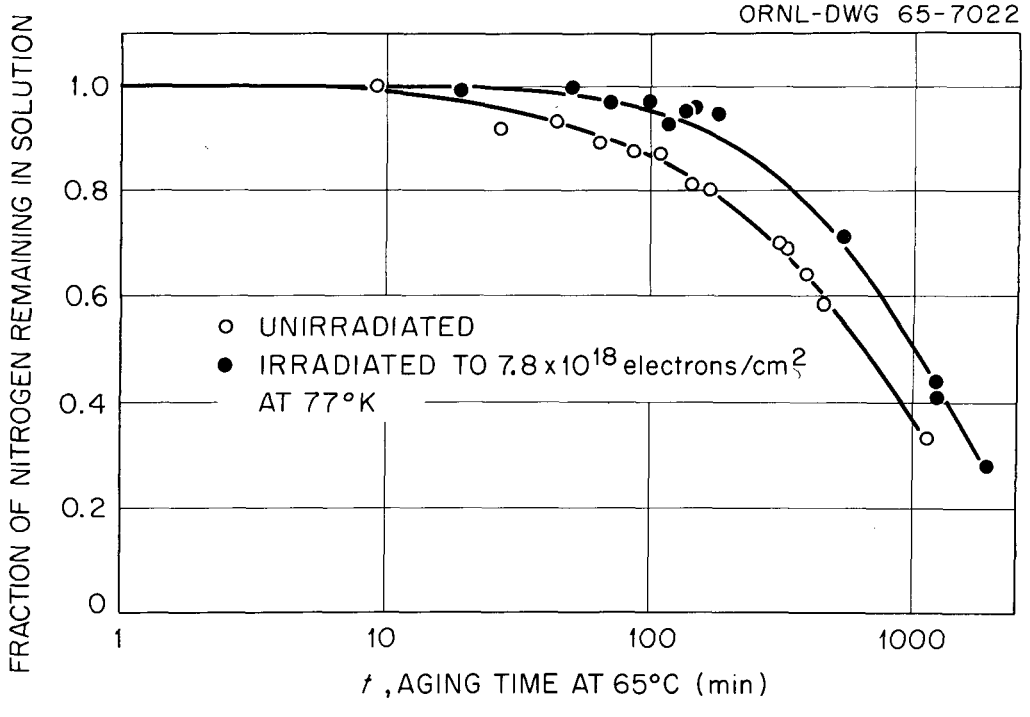

Fig. 6.4. Effect of 2-Mev Electron Irradiation on the Rate of the Precipitation of Nitrogen in Fe–0.013 wt % N at 65°C.

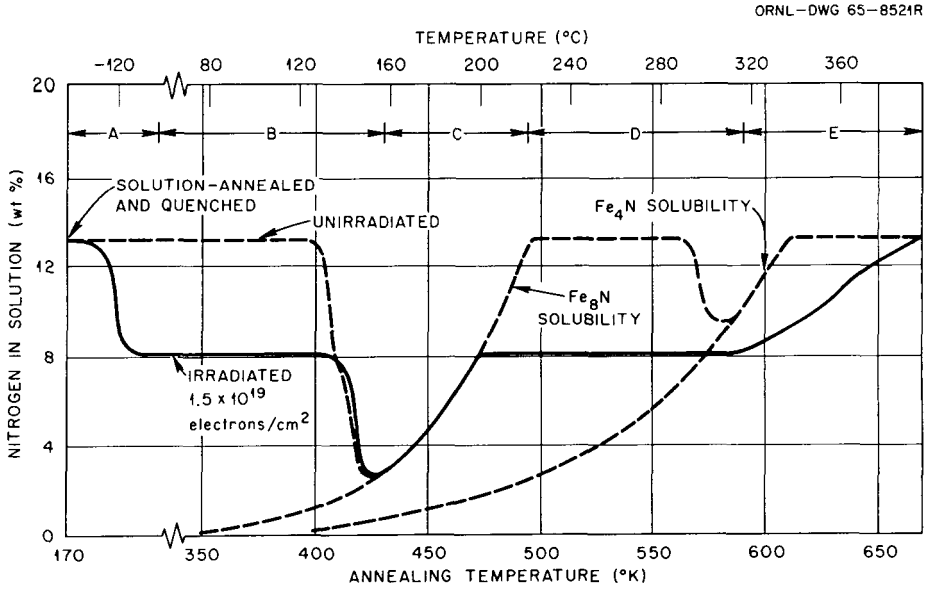

Fig. 6.5. Schematic Diagram of Isochronal Annealing of an Iron Specimen Containing 0.013 wt % N.

1.5×10^{19} electrons/cm^2. In Fig. 6.5 the amount of nitrogen remaining in solution (after, say, 15 min anneals at temperature intervals of 25°C) is plotted as a function of annealing temperature. Stage A represents the trapping of nitrogen atoms by radiation-produced defects. The temperature of this stage has not been definitely established, but it must occur below 35°C. If this stage occurs between −10°C and 35°C, it could be observed by measuring the nitrogen internal friction peak. If it occurs below −10°C, other techniques would have to be used.

Stage B represents the precipitation of nitride, Fe_8N. Although isochronal annealing experiments have not been done, we can estimate the location of stage B from isothermal annealing experiments. We have drawn stage B at somewhat lower temperatures for the unirradiated sample compared to the irradiated sample; this shift is in qualitative accord with the isothermal measurements.

Stage C represents the re-solution of the Fe_8N precipitate according to the solubility data of Fast and Verrijp.[7] In the case of the

[7]J. D. Fast and M. B. Verrijp, "Solubility of Nitrogen in Alpha-Iron," J. Iron Steel Inst. (London) 180, 337–43 (1955).

unirradiated sample, the recovery continues until the total amount of nitrogen is redissolved. In the case of the irradiated sample the nitrogen recovers only to the level remaining after stage A.

Stage D represents the precipitation of the nitride, Fe_4N. The location of this stage is suggested by isothermal aging experiments. The high temperature of this stage is apparently due to nucleation difficulties. We have indicated that we don't expect this stage for the irradiated sample because of the lower free nitrogen concentration.

For the unirradiated sample stage E represents the re-solution of Fe_4N according to the data of Fast and Verrijp. For the irradiated sample stage E represents the breakup of the nitrogen atom-defect complex. The temperature of this stage is based on the observations shown in Fig. 6.3.

Conclusions

Although our measurements are incomplete, one conclusion at this time is that our results do not agree with the results of the Brookhaven measurements as to the number of defects needed to trap nitrogen or carbon atoms. In the Brookhaven experiments about 0.01 wt % C was present in the samples and a fast neutron dose of 4.8×10^{16} neutrons/cm^2 caused half of the carbon to be trapped.[1] Thus, for a primary cross section of 3 barns, 1600 defects per primary knock-on would be required on the average to produce vacancies equal to the number of carbon atoms. Normally the number of defects per primary collision event for neutron spectra such as that in the Brookhaven experiment is taken to be about 100 to 200. The discrepancy might be explained by assuming the flux measurements to be in error by a factor of 10. However, on the basis of our electron experiments about 6 times this number would be required to trap all of the carbon atoms so that the flux measurements would have to be in error by a factor of 60. In our longest neutron irradiation of 23 days the fast neutron dose was 1.3×10^{17} neutrons/cm^2, and if the number of defects per primary collision were 1600 then the defect concentration would equal the nitrogen atom concentration. However, our experiments showed no measurable trapping of the nitrogen atoms for this

case. If one assumes that the flux measurements were in error so that there actually were equal numbers of carbon atoms and vacancies, and that excess vacancies were not needed to trap all of the carbon atoms, then it appears that the reaction would have occurred faster than observed by Damask et al. Thus, for a vacancy concentration of 4.7×10^{-4} the number of jumps required for a carbon to reach a vacancy would be 6×10^{2} and at 50°C this would require about 1 min, whereas the time observed by Wagenblast and Damask[1] was 20 min. In view of the above discussion, we feel that the process observed could not have been trapping of a carbon atom by a vacancy on a one-to-one basis, but must have been some more complicated process such as precipitation of a carbide on nuclei created by the irradiation. It is obvious that a great deal more work will be required before the behavior of interstitials such as carbon and nitrogen in irradiated iron will be understood.

For the case of neutron irradiated specimens more attention should be given to the role of substitutional impurities that might be formed by nuclear transmutations. It is known that a number of elements introduced into iron in small quantities can attract nitrogen and carbon atoms and effectively remove them from solid solution as far as the internal friction peak is concerned.[8] These impurity elements could also act as nuclei for the formation of precipitates. Neutron irradiation could act by two mechanisms to increase the effective concentration of such impurity atoms: (1) The energetic displacement events occurring in the neighborhood of a region rich in such impurities could distribute them through the lattice so that they are more effective. (2) Nuclear transmutations could change an impurity into one that interacts more strongly with carbon or nitrogen. In order to investigate these possibilities, experiments should be done with different neutron spectra and with much purer iron.

---

[8]An early paper on this subject is L. J. Dijkstra and R. J. Sladek, "Effect of Alloying Elements on the Behavior of Nitrogen in Alpha Iron," J. Metals 5, 69–73 (1953). For more recent information of this type see J. F. Enrietto, "Complex Damping Effects in Fe-Mn-N Alloys," Trans. Met. Soc. AIME 224, 1119–23 (1962).

Another important problem is to determine the energy of interactions of each type of defect, interstitial and vacancy, with carbon and nitrogen in iron. Clearly, these experiments should be carried out with irradiations, such as electron irradiations, that produce simple damage states.

Radiation-Enhanced Segregation in a Copper-Nickel Alloy

J. M. Williams B. C. Kelley
M. S. Wechsler

In a previous report[9] it was shown that bombardment of copper-nickel alloys at liquid-nitrogen temperature with fast neutrons endows the material with the ability to undergo segregation upon subsequent warm-up. The segregation is accompanied by a decrease in the electrical resistivity. Isochronal annealing curves showing the change in resistivity as a function of temperature following neutron irradiation were reported. It was further shown[10] that the effect of low-temperature electron bombardment in producing the resistivity decrease was similar to that of the neutron bombardment. From these studies it was concluded that radiation enhanced diffusion is the primary mechanism whereby the radiation produces the segregation.

In the present experiment, we have measured the activation energy of the thermally activated resistivity decrease following low-temperature neutron bombardment using the ratio-of-slopes method. We will now show that this activation energy should equal the energy of motion of the diffusion-enhancing point defect.

In the ratio-of-slopes method[11] the activation energy of a process is calculated from the change in the rate of the process upon abruptly changing the isothermal annealing temperature from one value to another.

---

[9]J. M. Williams, W. Schüle, B. C. Kelley, and M. S. Wechsler, Fuels and Materials Development Program Quart. Progr. Rept. June 30, 1964, ORNL-TM-920, p. 92.

[10]J. M. Williams, B. C. Kelley, and M. S. Wechsler, Fuels and Materials Development Program Quart. Progr. Rept. March 31, 1965, ORNL-TM-1100, p. 45.

[11]A. C. Damask and G. J. Dienes, p. 147 in Point Defects in Metals, Gordon and Breach, New York, 1963.

The type of measurements required are illustrated schematically in Fig. 6.6. Now, under radiation enhanced diffusion, the change in resistivity that has taken place at a given time will be a function of the number of atomic jumps, n_J, that have taken place. Thus,

$$\Delta\rho = \Delta\rho(n_J) \quad , \tag{1}$$

whereupon

$$\frac{d\Delta\rho}{dt} = \frac{d\Delta\rho}{dn_J} \frac{dn_J}{dt} \quad . \tag{2}$$

Now,

$$\frac{dn_J}{dt} = n_D \nu_D \quad , \tag{3}$$

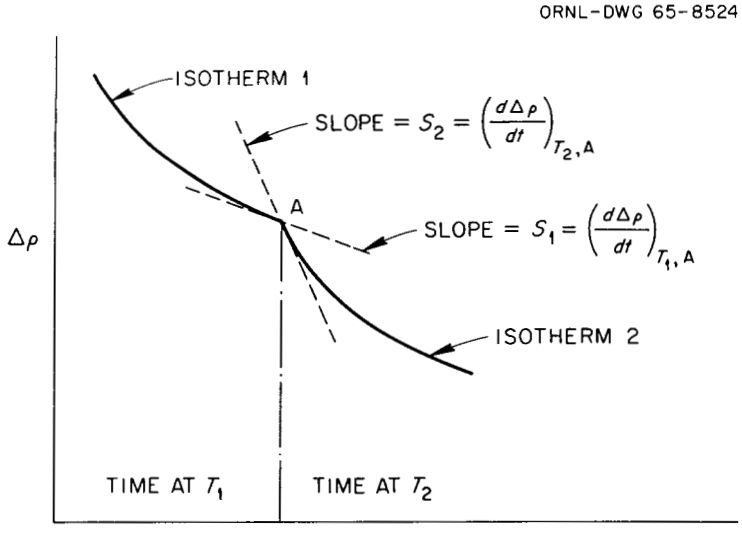

Fig. 6.6. Schematic Anneal Curve at Temperature T_1 and T_2 to Illustrate Activation Energy Determinations by Ratio-of-Slopes Method.

where n_D is the concentration of diffusion-enhancing defects and ν_D is the jump rate of each defect; ν_D may be expressed as

$$\nu_D = \nu_0 \exp(-E_m/kT) \quad , \tag{4}$$

where E_m is the energy of motion of the defect and k is Boltzmann's constant. Thus,

$$\frac{d\Delta\rho}{dt} = \frac{d\Delta\rho}{dn_J} n_D \nu_0 \exp(-E_m/kT) \quad . \tag{5}$$

Now, $\frac{d\Delta\rho}{dn_J}$ is in general a function of $\Delta\rho$. But since the final value of $\Delta\rho$ for Isotherm 1 is the same as the initial value for Isotherm 2 (at point A, Fig. 6.6), the value of $\frac{d\Delta\rho}{dn_J}$ is the same for both isotherms. Similarly, n_D at point A is common to the two isotherms. Thus, at the point where the two isotherms intersect, we have for the slopes of the two isotherms

$$S_1 = \left(\frac{d\Delta\rho}{dt}\right)_{T_1,A} = \left(\frac{d\Delta\rho}{dn_J}\right)_A n_D(A) \nu_0 \exp(-E_m/kT_1) \tag{6}$$

and

$$S_2 = \left(\frac{d\Delta\rho}{dt}\right)_{T_2,A} = \left(\frac{d\Delta\rho}{dn_J}\right)_A n_D(A) \nu_0 \exp(-E_m/kT_2) \tag{7}$$

and hence

$$\ln(S_2/S_1) = \frac{E_m}{k}\left(\frac{1}{T_1} - \frac{1}{T_2}\right) \tag{8}$$

from which E_m can be evaluated. It should be pointed out, however, that this method assumes a uniquely activated process.

In this experiment a series of short isothermal annealing curves were obtained for a Ni–40 wt % Cu alloy that had previously been irradiated to a dose of 1×10^{17} neutrons/cm^2 ($E > 1$ Mev) at a temperature of about −180°C. These results are shown in Fig. 6.7. From expanded plots of these curves the activation energies were evaluated from Eq. (8) for the temperature range shown. The results are summarized in Table 6.1. It is seen that the apparent activation energy

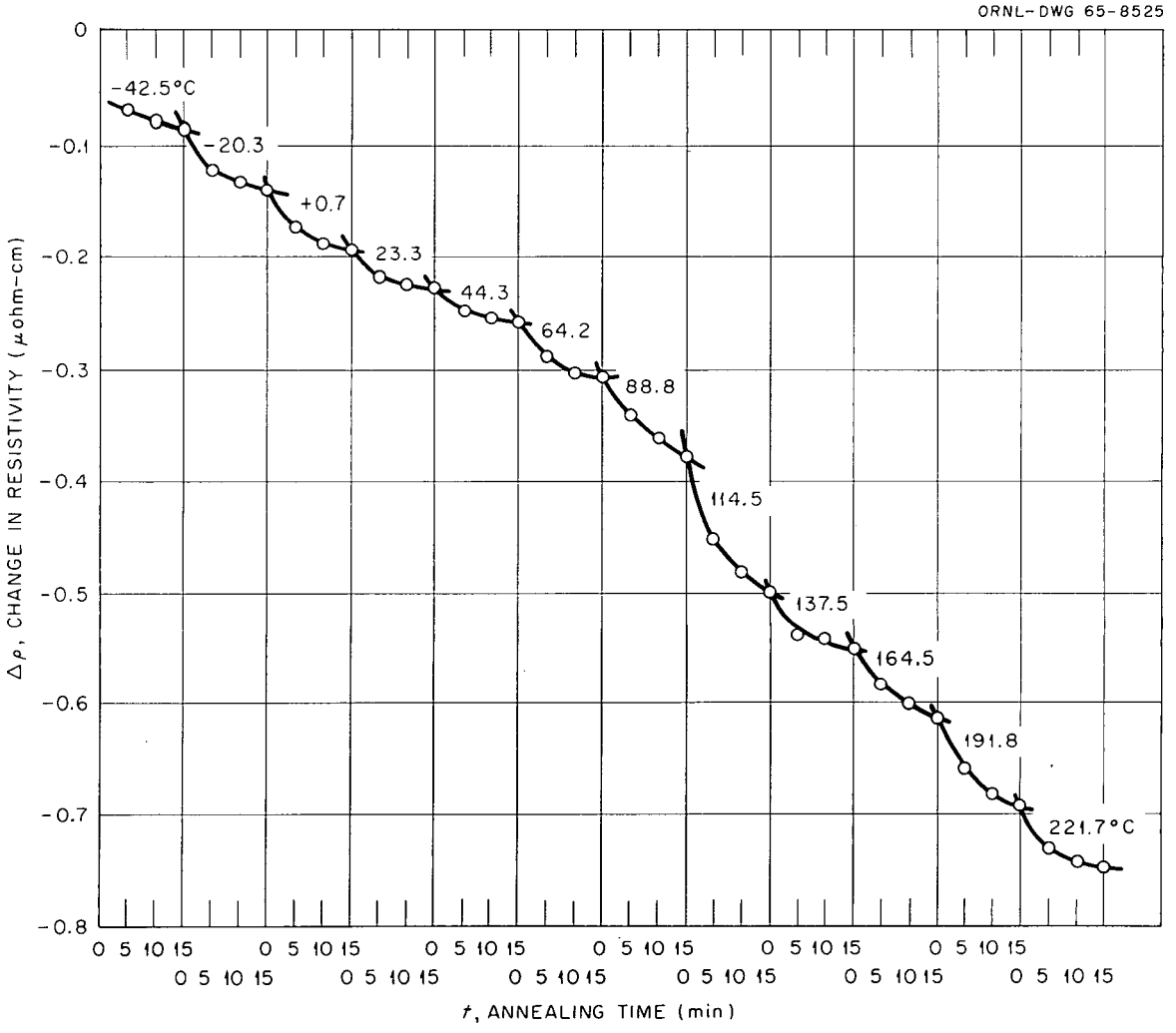

Fig. 6.7. Annealing of Ni–40 wt % Cu after Irradiation to 1×10^{17} neutrons/cm^2 ($E > 1$ Mev) at −180°C. All resistivity measurements at −196°C.

Table 6.1. Activation Energies for Annealing Ni–40 wt % Cu after Irradiation to 1 x 10^{17} neutrons/cm^2 (E > 1 Mev) at –180°C

Temperature of Isotherm 1 (°C)	Temperature of Isotherm 2 (°C)	Activation Energy, E_m (ev)
–42.5	–20.3	0.56
–20.3	+0.7	0.69
+0.7	23.3	0.93
23.3	44.3	1.22
44.3	64.2	1.26
64.2	88.8	1.28
88.8	114.5	1.31
114.5	137.5	1.28
137.5	164.5	1.57[a]
164.5	191.8	1.25
191.8	221.7	1.69

[a]Doubtful value.

increases generally with increasing temperature, although over the fairly wide range of temperatures from 23 to 192°C, E_m is quite constant at a value between 1.2 and 1.3 ev.

A Study of Radiation Hardening in Iron by Stress Relaxation Techniques

S. M. Ohr

This program has been directed toward an understanding of the mechanism of radiation hardening in body-centered cubic metals, especially iron and its alloys. It is shown that the radiation hardening can be attributed to two causes: (1) an increase in the dynamical resistance of the lattice to dislocation motion, and (2) the difficulty in the generation and multiplication of dislocations. With the use of a stress relaxation technique, we have been able to measure these effects separately. It is found that, while the density of mobile dislocations is lowered by as much as 2 orders of magnitude upon irradiation, the

major cause of the radiation hardening is the increase in the dynamical resistance of the lattice to dislocation motion. We will first describe the techniques and the results obtained for unirradiated samples and then will proceed to compare these with the results from the irradiated samples.

Since Johnston and Gilman[12] measured the velocity of dislocations in LiF by etch-pit techniques, the stress dependence of the dislocation velocity has often been represented by the formula

$$v = (\sigma/\sigma_o)^m \quad , \tag{9}$$

where

v = the average dislocation velocity,

σ = the uniaxial tensile stress,

σ_o = the stress corresponding to unit velocity,

m = the index of the stress dependence of the velocity.

Stein and Low[13] found that the value of m for edge dislocations in silicon iron is approximately 35 at room temperature. Since then a number of indirect measurements[14] have shown that the value of m increases rapidly with strain.

We applied a stress relaxation technique[15] to study dislocation dynamics in unirradiated iron and iron-silicon and in irradiated iron. In the stress relaxation technique, a tensile sample is deformed in an

---

[12]W. G. Johnston and J. J. Gilman, "Dislocation Velocity, Dislocation Densities, and Plastic Flow in LiF Crystals," J. Appl. Phys. 30, 129 (1959).

[13]D. F. Stein and J. R. Low, Jr., "Mobility of Edge Dislocations in Silicon-Iron Crystals," J. Appl. Phys. 31, 362 (1960).

[14]W. G. Johnston and D. F. Stein, "Stress Dependence of Dislocation Velocity Inferred from Strain Rate Sensitivity," Acta Met. 11, 317 (1963).

[15]F. W. Noble and D. Hull, "Stress Dependence of Dislocation Velocity from Stress Relaxation Experiments," Acta Met. 12, 1089 (1964).

Instron machine to a certain amount of strain, the crosshead motion is suddenly halted, and the subsequent change in the applied stress is recorded continuously as a function of time (Fig. 6.8). When a tensile test is interrupted, the stress relaxes because the plastic flow continues as the dislocations gradually come to rest. Since the total strain rate $\dot{\epsilon}$ is held to zero, the plastic strain rate $\dot{\epsilon}_p$ is matched by an elastic strain rate $\dot{\epsilon}_e$, i.e.,

$$0 = \dot{\epsilon} = \dot{\epsilon}_e + \dot{\epsilon}_p$$

$$= \frac{1}{E}\frac{d\sigma}{dt} + 0.5\, b\, \rho\, v \quad , \tag{10}$$

where

E = the combined elastic modulus of the specimen and the machine,

0.5 = the orientation factor for tensile strain,

b = the Burgers vector,

ρ = the mobile dislocation density.

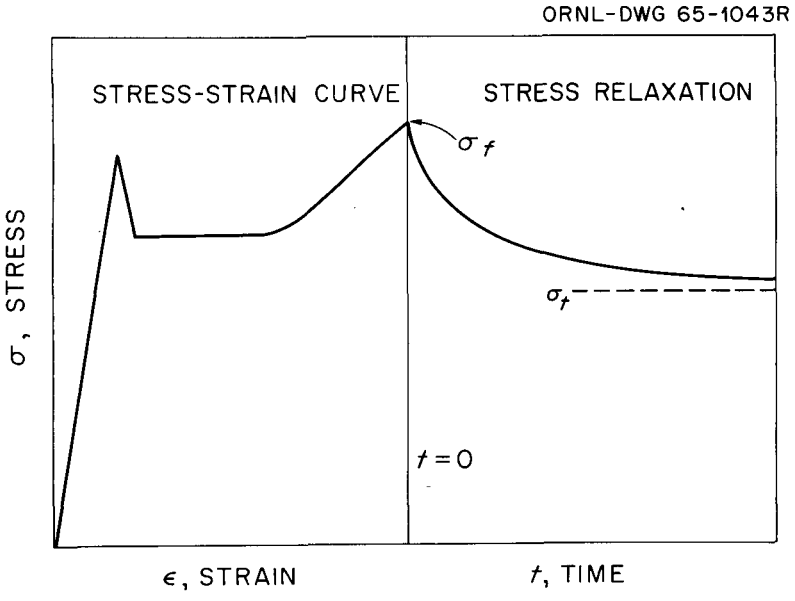

Fig. 6.8. Schematic Stress-Strain and Stress-Time Curves.

In both unirradiated and irradiated samples, the stress relaxes rapidly at first. However, as the relaxation progresses, the rate of relaxation diminishes gradually and eventually the stress approaches an asymptotic value. Since the slope of the relaxation curve, $\frac{d\sigma}{dt}$, is directly proportional to the dislocation velocity, v, we have interpreted this asymptotic value to be a threshold stress, σ_t, below which there is no macroscopic motion of dislocations. The stress effective in moving the dislocations is, therefore, the difference between the applied stress and the threshold stress. It is proposed that the velocity of the dislocations should be written as

$$v = \mu \, (\sigma - \sigma_t)^m \quad , \tag{11}$$

and the plastic strain rate should be given as

$$\dot{\epsilon}_p = 0.5 \; b \; \rho \; v$$

$$= 0.5 \; b \; \rho \; \mu \; (\sigma - \sigma_t)^m \quad , \tag{12}$$

where μ is the mobility of the dislocations (i.e., the velocity under unit effective stress).

The equation governing the stress relaxation is written as

$$\frac{1}{E} \frac{d\sigma}{dt} + 0.5 \; b \; \rho \; \mu \; (\sigma - \sigma_t)^m = 0 \quad . \tag{13}$$

From Eqs. (12) and (13), the plastic strain rate is related to the relaxation rate, $\frac{d\sigma}{dt}$, and to the applied stress in the following manner,

$$\dot{\epsilon}_p / 0.5 \; b = \rho \; v = - \frac{1}{0.5 \; b \; E} \frac{d\sigma}{dt}$$

$$= \rho \; \mu \; (\sigma - \sigma_t)^m \quad . \tag{14}$$

When the logarithm of the plastic strain rate, measured from the relaxation rate, is plotted against the logarithm of the effective stress, $\sigma - \sigma_t$, the value of m can be obtained from the slope and the intercept should yield the value of $\rho\,\mu$, which is a measure of the mobile dislocation density.

In Fig. 6.9 we have plotted the decay of the plastic strain rate as a function of the effective stress obtained from an Fe–3.2 wt % Si sample that has been given a strain of 0.8% prior to stress relaxation.

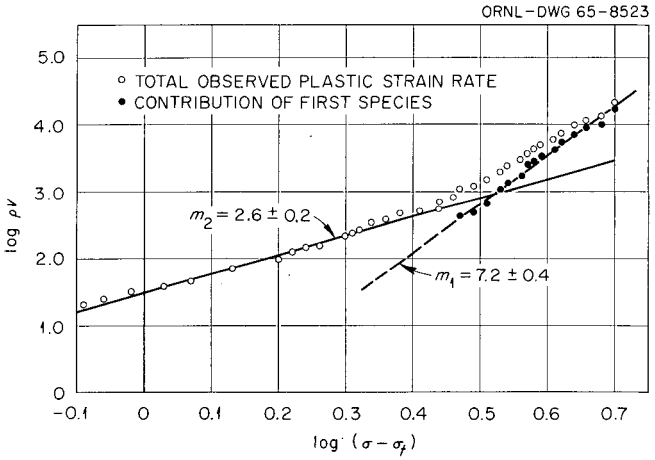

Fig. 6.9. Plot of the Plastic Strain Rate vs the Effective Stress During Stress Relaxation for Fe–3.2 wt % Si. The straight lines represent the least-square fit and the errors indicate the standard deviation of the slope.

The start of the stress relaxation is represented by the first point on the upper right corner and the subsequent points are obtained as the stress relaxation progresses. It can be seen in this plot that the points lie nearly along two straight lines indicating that the plastic deformation is carried out by two species of dislocations that differ in the values of the stress dependence of the velocity, m. The dislocations whose contribution to the plastic strain rate is predominant in the early stage of the relaxation will be called the first species, while those that contribute most in the later stage will be called the second species. To separate out the two species, the line representing the latter was extended into the early stage of the relaxation, the

antilogarithm of the extended portion was subtracted from that of the total observed strain rate and the logarithm of the difference was replotted against the effective stress. This procedure has yielded another straight line, which is then taken as the contribution of the first species.

Figure 6.10 shows a similar plot obtained from Ferrovac-E iron, after the sample has been given strains of 0.6 and 10.6%, respectively. In both silicon iron and high-purity iron, each of the stress relaxation curves can be separated into two straight lines corresponding to the following values of m,

$$m_1 = 7.0 \pm 0.6$$

$$m_2 = 2.5 \pm 0.3$$

and the values of m obtained in this way do not vary with strain within the experimental errors. The representation of the relaxation curves

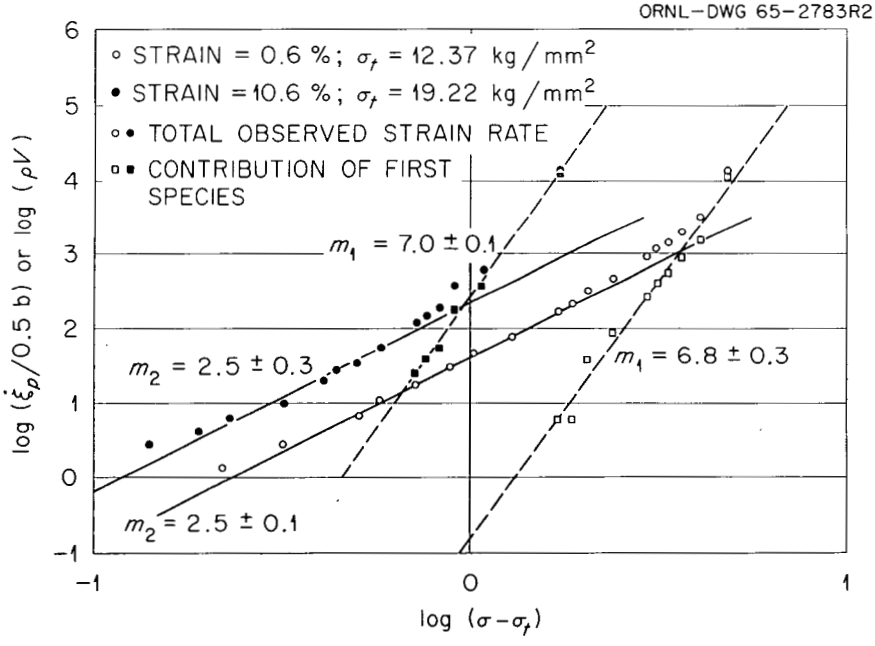

Fig. 6.10. Plot of the Plastic Strain Rate vs the Effective Stress for Ferrovac-E Iron after the Sample was Strained to 0.6 and 10.6%.

by straight lines implies that the densities of mobile dislocations remain constant during the relaxation. In terms of the two species of dislocations, the plastic strain rate is written as

$$\dot{\epsilon}_p = 0.5\, b \left[\rho_1\, \mu_1\, (\sigma - \sigma_t)^7 + \rho_2\, \mu_2\, (\sigma - \sigma_t)^{2.5}\right] . \qquad (15)$$

The magnitude of the threshold stress varies with strain at which the tensile test is halted. In Fig. 6.11 we have plotted the threshold stress and the flow stress as a function of strain. It is shown that the threshold stress is significantly high even at the onset of plastic deformation and it increases rapidly at strains greater than the Lüders strain. We have defined the initial value of the threshold stress as the plastic limit, σ_p (Fig. 6.11), after Gilman and Johnston[16] who have measured a similar quantity in LiF by etch-pit techniques. The portion of the threshold stress that increases with strain is

[16] J. J. Gilman and W. G. Johnston, "Dislocations in LiF Crystals," Solid State Phys. 13, 148 (1962).

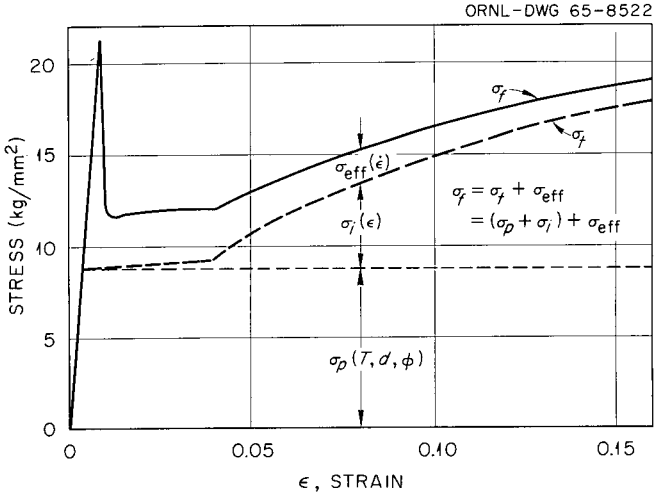

Fig. 6.11. Plot of the Flow and Threshold Stress vs Strain for Ferrovac-E Iron. The flow stress has been separated into the plastic limit, σ_p, the internal stress, σ_i, and the effective stress, σ_{eff}.

interpreted as the internal stress field associated with work-hardening. Johnston[17] has proposed that in work-hardening crystals the velocity of dislocations should be written as

$$v = \left(\frac{\sigma - \sigma_i}{\sigma_o} \right)^m , \tag{16}$$

where σ_i, expressed as

$$\sigma = H \epsilon_p , \tag{17}$$

is the internal stress field and H is the rate of work-hardening. Our results indicate that σ_i in Eq. (16) should be replaced by the threshold stress, σ_t, and the threshold stress is composed of the internal stress field, σ_i, and the plastic limit, σ_p. We have found that the threshold stress is quite sensitive to the test temperature, while the internal stress field is expected to be relatively insensitive to the test temperature. It is further noticed that the threshold stress depends on the grain size and the irradiation dose. We, therefore, express the threshold stress as follows,

$$\sigma_t = \sigma_p (T, d, \phi) + \sigma_i (\epsilon) , \tag{18}$$

where σ_p is the plastic limit and ϕ is the irradiation dose. The effective stress, on the other hand, is proportional to the test speed.

It can be seen that the first species of dislocations initially carries between 80 to 90% of the plastic strain rate and that these dislocations are the first to decay out during the stress relaxation. This is taken as evidence that the first species of dislocations moves

---

[17]W. G. Johnston, "Yield Points and Delay Times in Single Crystals," J. Appl. Phys. 33, 2716 (1962).

faster than the second species. Since the etch-pit study[12] has shown that the edge dislocation segments move at a velocity considerably greater than that of the screw segments, we may conclude that the first species is the edge dislocation and the second species is the screw dislocation. In fact, when the mobility data of Stein and Low[13] on edge dislocations in silicon iron are reexamined so as to subtract a threshold stress from the applied stress, the value of m is found to lie close to our value of m_1. It is expected that the edge dislocations are apt to travel a long distance and reach out to the surface under the influence of the applied stress while the screw dislocations are left behind in the crystal. This may be the reason why Stein and Low could observe only edge dislocations in their etch-pit work and also, during transmission electron microscopic examination of deformed iron,[18] why the dislocations observed were mainly of screw type.

In order to study the effect of electron and neutron irradiations on the mechanical properties in terms of the dislocation dynamics, a number of tensile samples of Ferrovac-E iron were irradiated with 2-Mev electrons to doses up to 8×10^{18} electrons/cm^2 and also with neutrons to doses up to 8×10^{18} neutrons/cm^2 ($E > 3$ Mev). For the electron irradiations the current density was about 23 μa/cm^2, and the irradiation temperature ranged from 55 to 65°C. For the neutron irradiations the irradiation temperature was about 96°C.

Figure 6.12 shows a plot of the relaxation rate against the effective stress obtained for a sample electron irradiated to a dose of 4.24×10^{18} electrons/cm^2, along with the curve obtained from an unirradiated sample. Figure 6.13 shows a similar plot obtained from a sample that was neutron irradiated to a dose of 1.28×10^{18} neutrons/cm^2 ($E > 3$ Mev). In these plots, each of the stress relaxation curves can again be separated into two straight lines corresponding to the values of m of 7 and 2.5, indicating that irradiation does not affect the stress dependence of dislocation velocity.

---

[18]S. M. Ohr and D. N. Beshers, "Crystallography of Dislocations and Dislocation Loops in Deformed Iron," Phil. Mag. 10, 219 (1964).

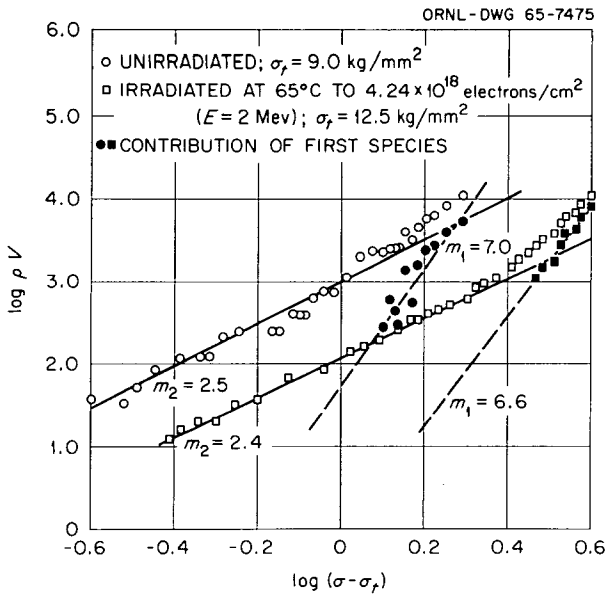

Fig. 6.12. Dislocation Velocity vs Effective Stress in Electron Irradiated Ferrovac-E Iron. Grain size is 30 μ. Tested at room temperature.

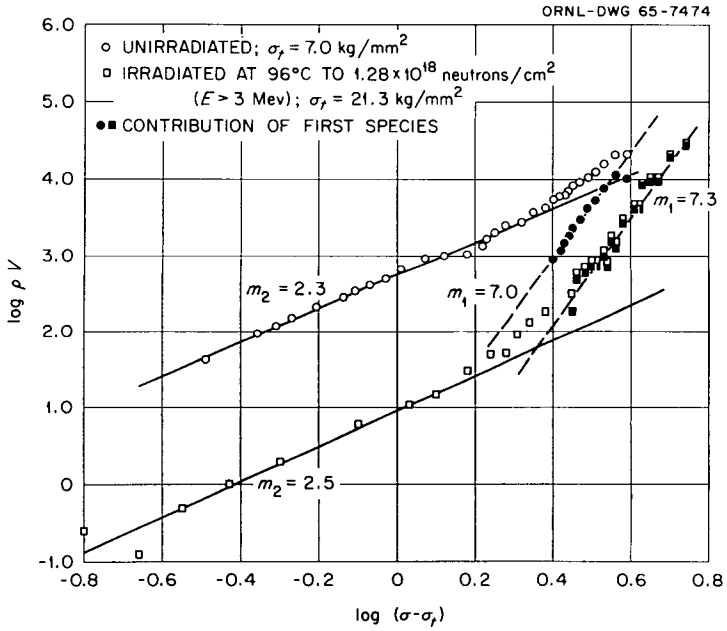

Fig. 6.13. Dislocation Velocity vs Effective Stress in Neutron Irradiated Ferrovac-E Iron. Grain size is 130 μ.

Since the edge dislocations play a predominant role in plastic deformation, the plastic strain rate, given by Eq. (15), may be approximated as

$$\dot{\varepsilon}_p = 0.5\, b\, \rho_e\, \mu_e\, (\sigma - \sigma_t)^7 \quad , \tag{19}$$

where the subscript e refers to the edge dislocation segments. By rearranging the terms, the yield or flow stress can be written as

$$\sigma = \sigma_t + \left(\frac{\dot{\varepsilon}_p}{0.5\, b\, \rho_e\, \mu_e} \right)^{1/7} \quad . \tag{20}$$

Thus, the yield or flow stress σ would increase if there is either an increase in the threshold stress, σ_t, or a decrease in the mobile dislocation density, ρ_e. We have found upon irradiations by both electrons and neutrons that the threshold stress has increased substantially. This increase in threshold stress is responsible for 70 to 90% of the radiation hardening as reflected by the yield stress. The remainder of the radiation hardening is attributable to a radiation produced decrease in the mobile dislocation density. The mobile dislocation density in the irradiated samples is lower than that in the unirradiated samples by as much as 2 orders of magnitude, which indicates that the generation and multiplication of dislocations are suppressed by irradiation. However, the variation in the yield stress is relatively insensitive to the changes in the mobile density due to the presence of the one-seventh power, as can be seen in Eq. (20).

It is concluded, therefore, that radiation hardening may be attributed to two effects. The major effect is the increase in the threshold stress, that is, the increased dynamical resistance of the lattice to dislocation motion. The reduction of mobile dislocation density makes a further small contribution to the hardening.

Tensile Tests on Irradiated Iron

N. E. Hinkle N. K. Smith

Since most irradiation effects studies on pressure vessel steels are conducted in neutron flux environments considerably in excess of the flux at the pressure vessel wall of operating power reactors, it is necessary to determine whether this variance of neutron flux (or dose rate) has an effect on the mechanical property changes observed at the same integrated neutron dose. Harries, Barton, and Wright[19] have reported that there is no dose-rate effect on the room temperature tensile strength of EN-2 mild steel irradiated from 100 to 350°C with fission neutron fluxes of 3 to 300 $\times 10^{11}$ neutrons cm^{-2} sec^{-1} at a neutron dose of about 2.2×10^{17} neutrons/cm^2. Since the longest exposure time in Harries' experiments was about 200 hr, it was felt that longer term irradiations at higher integrated doses may be needed to detect a dose-rate effect. Therefore, a series of experiments designed to investigate the effect of neutron-dose rate on the tensile properties of irradiated Ferrovac-E iron was initiated.[20] Ferrovac-E iron was chosen instead of steel because as a single-phase material it is easier to control its structure. The starting stock was supplied by the Crucible Steel Company with the following chemical analyses:

Element	wt %
Nickel	0.035
Chromium	0.01
Molybdenum	0.01
Cobalt	0.007
Sulfur	0.007
Silicon	0.006
Phosphorus	0.005

[19]D. R. Harries, P. J. Barton, and S. B. Wright, "Effects of Neutron Spectrum and Dose Rate on Radiation Hardening and Embrittlement in Steels," J. Brit. Nucl. Energy Soc. 2, 398 (1963).

[20]N. E. Hinkle and N. K. Smith, Fuels and Materials Development Program Quart. Progr. Rept. March 31, 1965, ORNL-TM-1100, p. 65.

Element	wt %
Copper	0.005
Vanadium	0.004
Manganese	0.001
Oxygen	0.0065
Carbon	0.004
Nitrogen	0.001
Hydrogen	0.0003

The material was vacuum-annealed for 2 hr at 885°C and furnace cooled. The resulting grain size was 130 μ.

Six experiment assemblies, previously described,[20] were built for irradiation in the poolside facility of the ORR at varying distances from the face of the reactor. Irradiation of four of the assemblies has been completed and testing of the samples has begun. Two of the assemblies are still being irradiated. Five of the assemblies will receive a dose of about 2×10^{18} neutrons/cm^2 ($E > 2.9$ Mev as determined by nickel activation) at dose rates of 7 to 1000×10^{10} neutrons cm^{-2} sec^{-1} The neutron flux is shown in Fig. 6.14 as a function of distance from the face of the reactor tank for a position about 3 in. below the reactor horizontal midplane. The nickel monitors were shielded in 40 mils of cadmium and therefore no correction for ^{58}Co burnup was required. The fast flux for a 2.5-day irradiation period is seen to decrease by a factor of 10/ft from the reactor face (open symbols, Fig. 6.14). The flux as a function of vertical distance above and below the horizontal midplane is shown in Fig. 6.15 for six separate distances from the face of the reactor. The irradiation assemblies were built and located at the reactor in a manner designed to maintain the maximum void space between any sample position and the reactor tank, thus minimizing moderation of the neutron flux. It is believed that this geometry should yield a nearly constant spectrum for the various irradiation positions.

The nominal irradiation temperature for these experiments was chosen as 94°C (200°F). However, due to uncontrollable factors, some

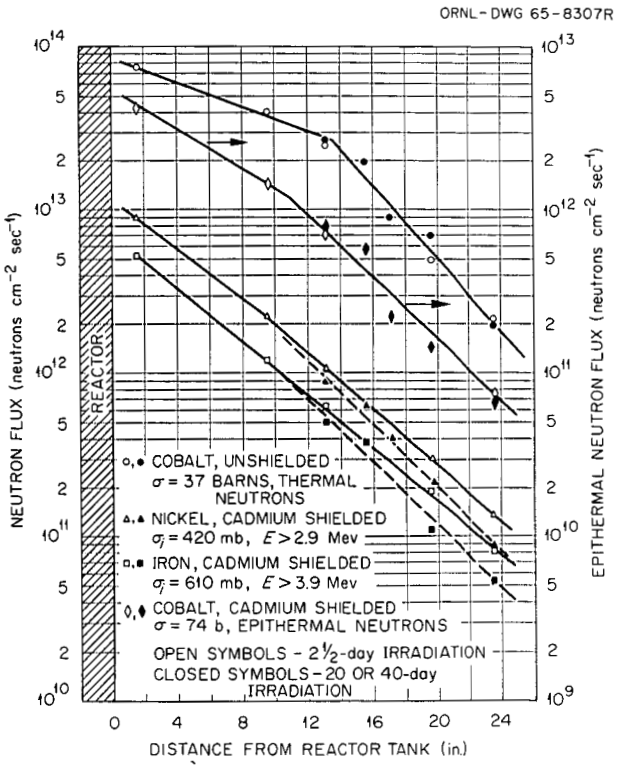

Fig. 6.14. Neutron Flux at the ORR P-6 Poolside Facility as a Function of Horizontal Distance from the Reactor Face, 3 in. Below the Horizontal Midplane.

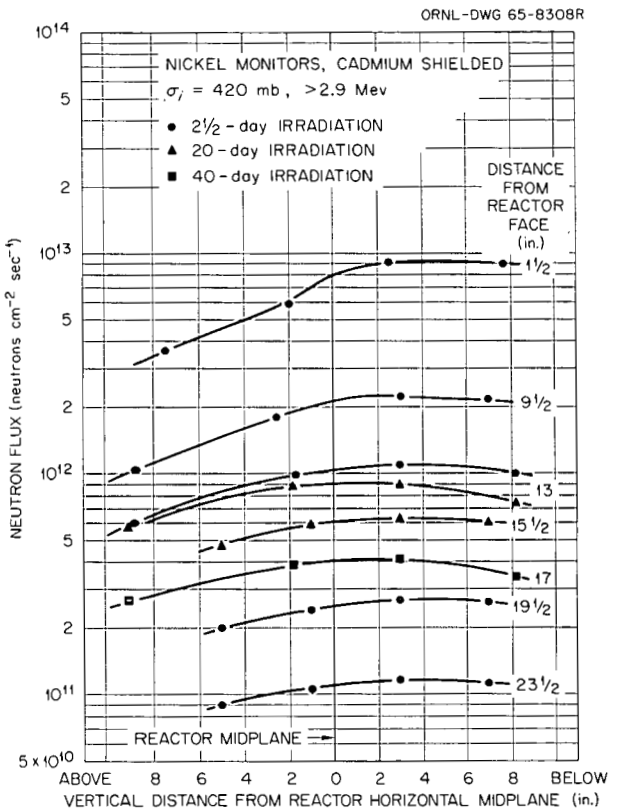

Fig. 6.15. Neutron Flux (E > 2.9 Mev) at the ORR P-6 Poolside Facility as a Function of Vertical Distance Above and Below the Reactor Horizontal Midplane. The horizontal distances from the face of the reactor are indicated.

samples were irradiated at temperatures as low as 70°C or as high as 105°C. Preliminary testing indicates that within that range of irradiation temperatures, the yield stress values are within the normal scatter due to material variables, primarily grain size.

The postirradiation testing of the Ferrovac-E iron has taken two approaches: (1) routine tensile tests and (2) stress relaxation tests by the method of Ohr.[21] The first results of the stress relaxation tests on irradiated samples are discussed in the previous section on dislocation dynamics in iron.

The tensile tests are performed on an in-cell Instron frame and crosshead with a remote console. Measurements of the sample elongation are made with a remote extensometer developed by R. G. Berggren and J. C. Wilson[22] and recently modified[23] to incorporate a direct-current voltage linear variable differential transformer in place of the alternating-current voltage LVDT formerly used. Tensile data are being obtained at a variety of strain rates, but the bulk of the data will be obtained at a strain rate of 0.02 min^{-1}.

The general effect of neutron irradiation is to increase the lower yield stress, decrease the rate of work hardening, and decrease the uniform elongation. This is shown in Fig. 6.16 by the true stress–true strain curves for one control and two irradiated samples (different doses) of coarse grain Ferrovac-E iron at each of three strain rates. It was previously reported[20] that a plot of log yield stress vs log Lüders strain for unirradiated Ferrovac-E iron indicates a good fit to the expression

$$\sigma_{LY} = K\bar{\epsilon}_L^n \quad . \tag{21}$$

---

[21]S. M. Ohr, "A Study of Radiation Hardening in Iron by Stress Relaxation Techniques," this chapter.

[22]R. G. Berggren and J. C. Wilson, "A Remotely Operated Extensometer," ASTM Bull. 210, 35 (December 1955).

[23]R. G. Berggren, W. J. Stelzman, and T. N. Jones, Fuels and Materials Development Program Quart. Progr. Rept. March 31, 1963, ORNL-TM-1100, p. 86.

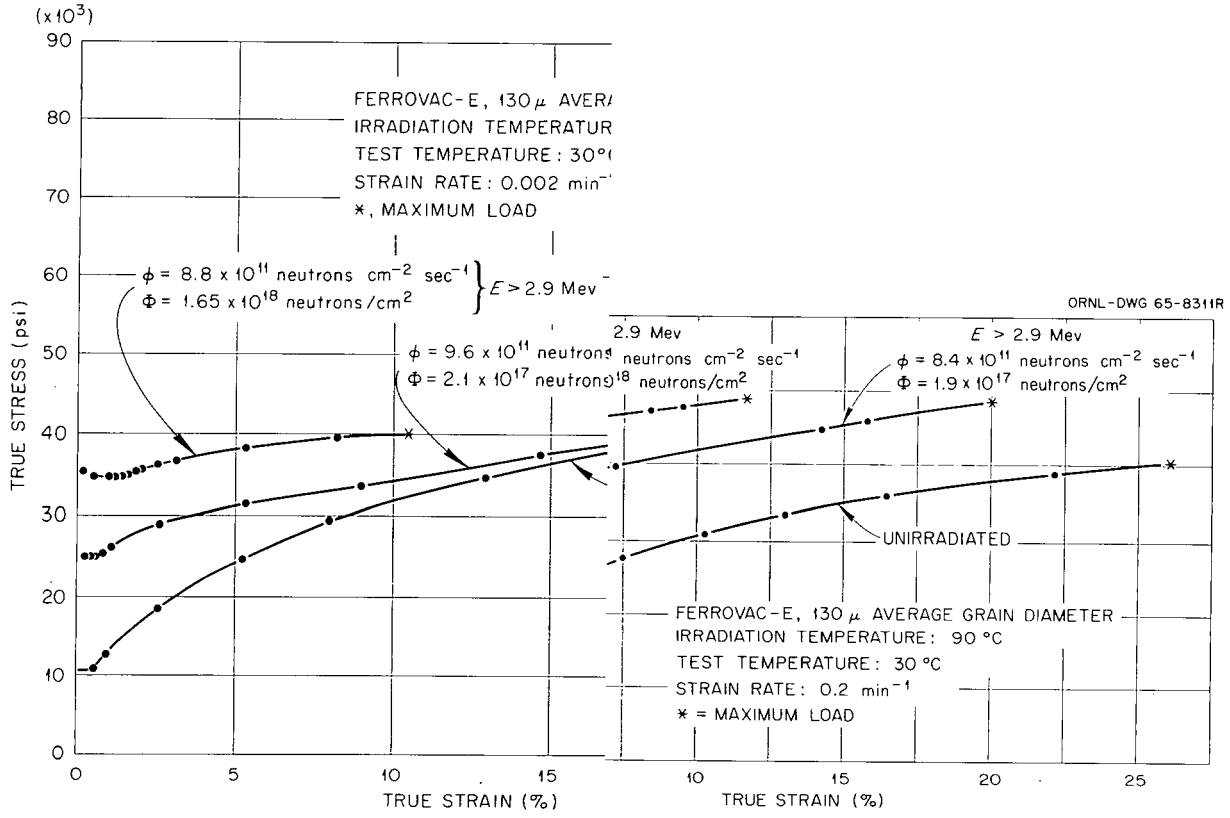
(x10³)
TRUE STRESS (psi)
TRUE STRAIN (%)
FERROVAC-E, 130 μ AVER
IRRADIATION TEMPERATUR
TEST TEMPERATURE: 30°
STRAIN RATE: 0.002 min⁻¹
*, MAXIMUM LOAD
φ = 8.8 x 10¹¹ neutrons cm⁻² sec⁻¹
Φ = 1.65 x 10¹⁸ neutrons/cm²
E > 2.9 Mev
φ = 9.6 x 10¹¹ neutrons
Φ = 2.1 x 10¹⁷ neutrons
ORNL-DWG 65-8311R
2.9 Mev
neutrons cm⁻² sec⁻¹
¹⁸ neutrons/cm²
E > 2.9 Mev
φ = 8.4 x 10¹¹ neutrons cm⁻² sec⁻¹
Φ = 1.9 x 10¹⁷ neutrons/cm²
UNIRRADIATED
FERROVAC-E, 130 μ AVERAGE GRAIN DIAMETER
IRRADIATION TEMPERATURE: 90 °C
TEST TEMPERATURE: 30 °C
STRAIN RATE: 0.2 min⁻¹
* = MAXIMUM LOAD
TRUE STRAIN (%)

However, for irradiated samples it is seen in Fig. 6.16 that the yield stress increases upon irradiation without any significant increase in the Lüders strain.

We have mentioned that a primary objective of this study is to determine whether radiation hardening or embrittlement is affected by the dose rate. The effect of dose rate on the lower yield stress at an integrated dose of about 1.5×10^{18} neutrons/cm^2 is shown in Fig. 6.17. It is seen that although there is a threefold increase in the lower yield stress, there appears to be no effect of dose rate for the flux range of 4 to 70 $\times 10^{11}$ neutrons cm^{-2} sec^{-1} ($E > 2.9$ Mev). Future investigation of the dose-rate effect in this series of experiments will include samples from lower fluxes and postirradiation damage recovery studies of the lower yield stress.

It has long been suspected that an interconnection exists between the strain-rate dependence of yield and flow stresses in the body-centered cubic metals and the ductile-brittle transition phenomenon

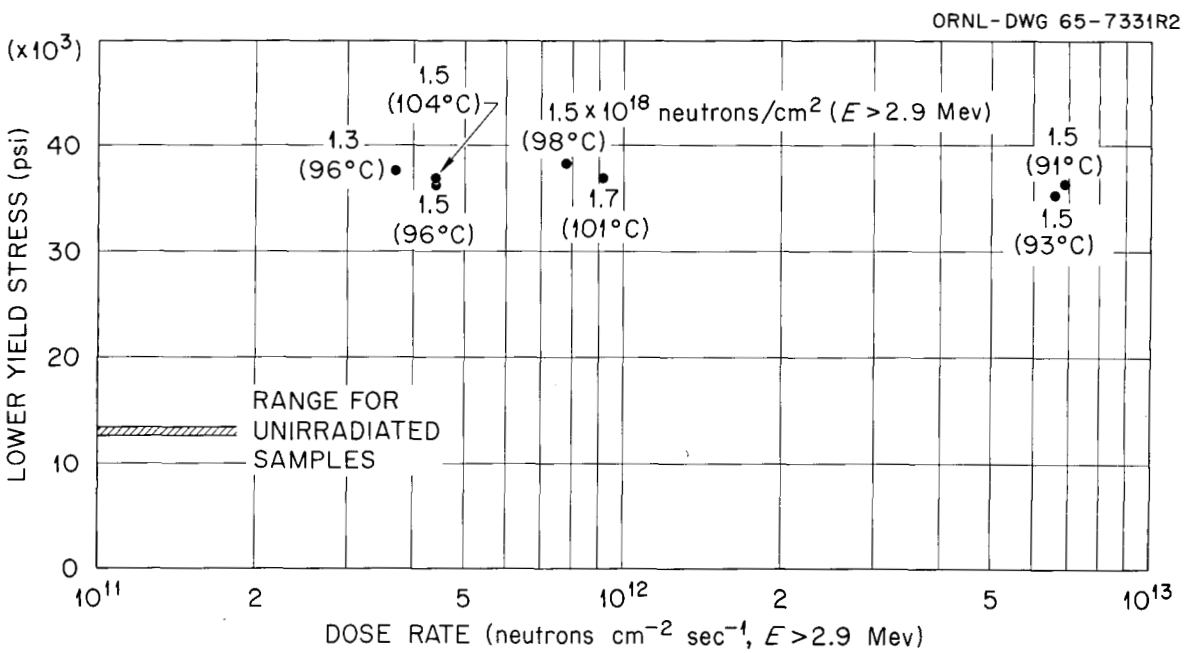

Fig. 6.17. Lower Yield Stress vs Dose Rate for Constant Dose and Irradiation Temperature as Shown. Sample: Ferrovac-E iron; grain size: 130-μ diameter; test temperature: 30°C.

exhibited by these metals. The strain rate dependence is sometimes analyzed in terms of the parameter[24,25]

$$m' = \frac{d \ln \dot{\epsilon}}{d \ln \sigma}$$

and, therefore, in Fig. 6.18 we have plotted log lower yield stress, σ_{LY}, vs log strain rate, $\dot{\epsilon}$, for our unirradiated Ferrovac-E iron. The values of m' for various segments of the curve are indicated. It is seen that the logarithmic strain rate sensitivity increases (m' decreases)

---

[24]W. G. Johnston and D. F. Stein, "Stress Dependence of Dislocation Velocity Inferred From Strain Rate Sensitivity," Acta Met. 11, 317 (1963).

[25]G. T. Hahn, "A Model For Yielding With Special Reference to the Yield Point Phenomena of Iron and Related BCC Metals," Acta Met. 10, 727 (1962).

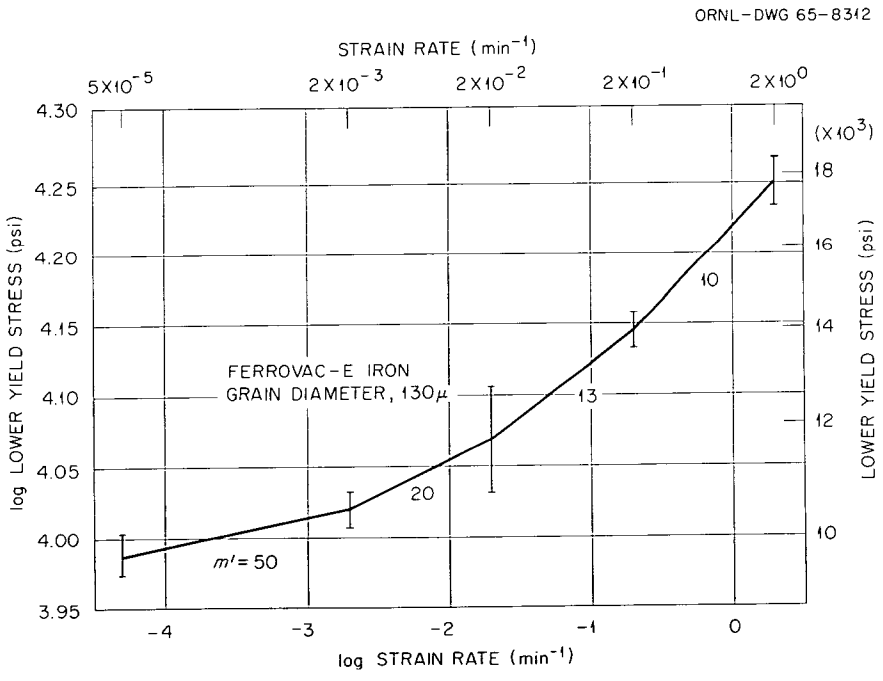

Fig. 6.18. Log Lower Yield Stress vs Log Strain Rate for Unirradiated Ferrovac-E Iron. Grain size: 130-μ diameter; test temperature: 23–30°C.

with increasing strain rate. Furthermore, the lower yield stress appears to approach asymptotically a lower limit with decreasing strain rate. Now, in view of the discussion in the previous section,[21] it seems reasonable to associate this asymtotic value with the threshold stress determined from stress relaxation experiments. To test this idea, the yield stress was determined as a function of strain rate for samples having grain diameters of 17, 60, and 130 μ. These samples were also given a stress relaxation treatment[21] following straining at various strain rates and the threshold stress was determined. The results are shown in Fig. 6.19, where it is seen that the threshold stress is independent of the strain rate prior to the stress relaxation run. Also, it is noted that in the limit as the strain rate approaches zero, the yield stress approaches the threshold stress for all three grain sizes.

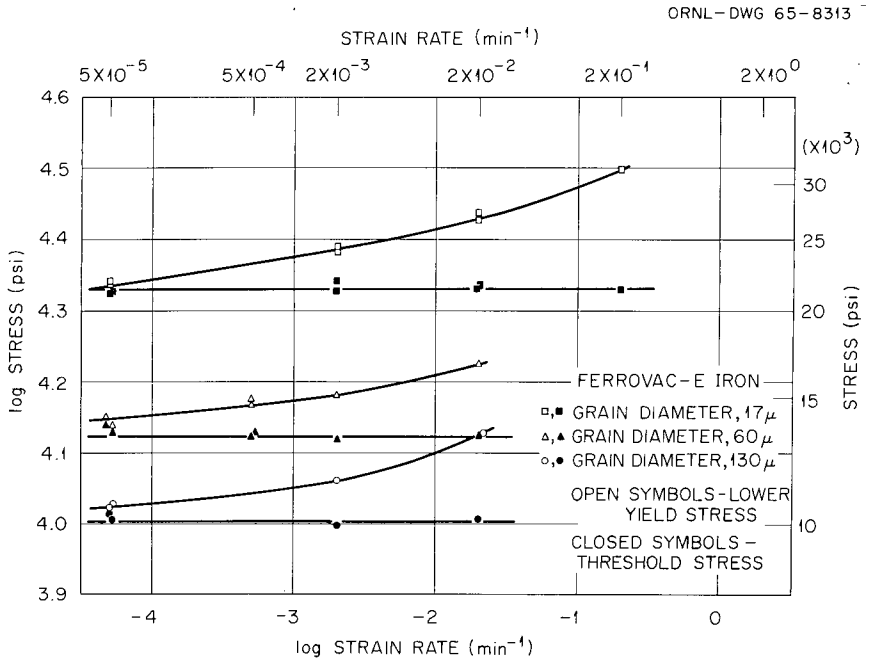

Fig. 6.19. Log Lower Yield Stress and Log Threshold Stress as a Function of Log Strain Rate for Ferrovac-E Iron of Three Grain Sizes. Test temperature: 24°C.

It is of interest to analyze the grain size dependence of the yield and threshold stresses. In Fig. 6.20 these stresses are plotted according to the Petch relation[26]

$$\sigma = \sigma_i + K_y d^{-1/2} .$$

Within the range of grain sizes used, the yield and threshold stresses appear to obey this relation. Furthermore, for the yield stress, σ_i and K_y are observed to increase with increasing strain rate.

[26]N. J. Petch, "The Cleavage Strength of Polycrystals," J. Iron and Steel Inst. (London) 174, 25 (1953).

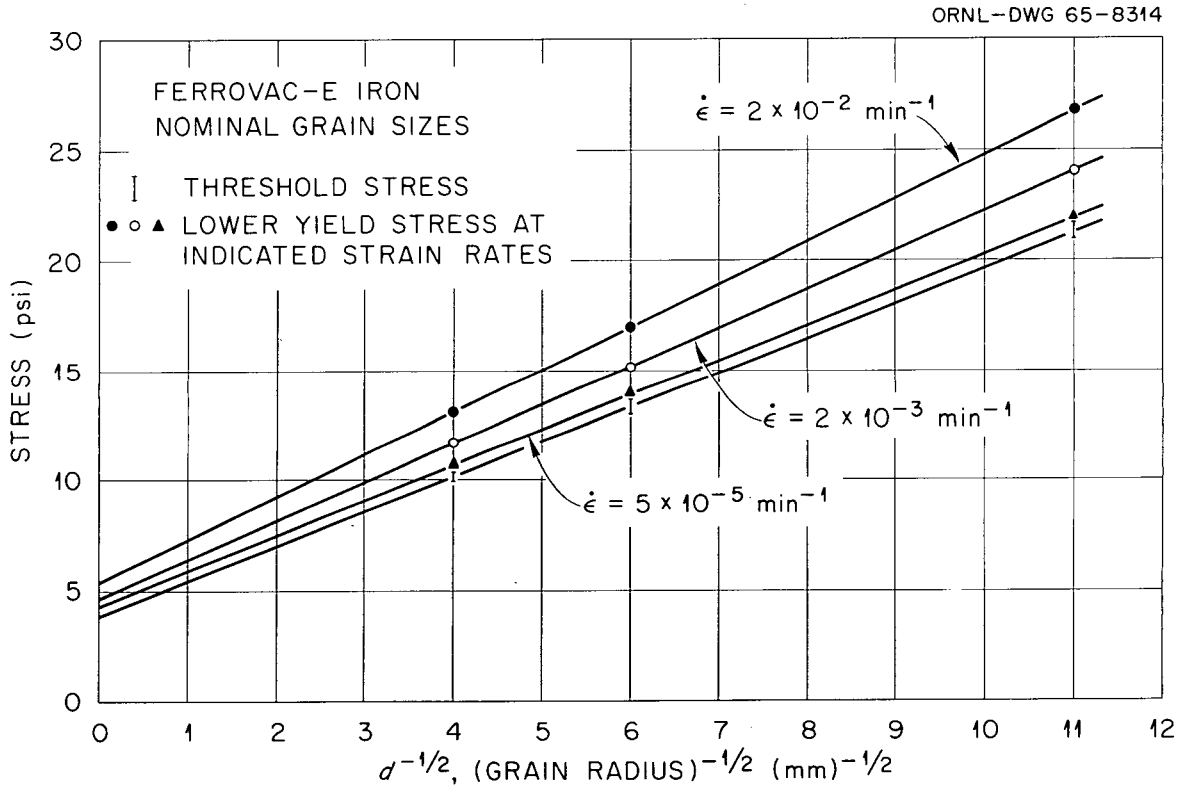

Fig. 6.20. Log Lower Yield Stress at Three Strain Rates and Threshold Stress vs (Grain Radius)$^{-1/2}$ for Ferrovac-E Iron. Test temperature: 24°C.

Plastic Deformation in Niobium Single Crystals[27]

R. E. Reed M. S. Wechsler

In recent years, there has been an increasing interest in plastic deformation in the refractory body-centered cubic metals. The interest stems in part from a desire to better understand the large temperature and strain rate dependence of flow in the body-centered cubic metals as compared to the face-centered cubic metals, and to determine whether the temperature and strain rate dependence has a bearing on the low-temperature brittleness of body-centered cubic metals. Since the effect of radiation on the ductile-brittle transition phenomenon is being investigated in the Radiation Metallurgy Section of the Solid State Division at ORNL, we have undertaken a study of the radiation effects on flow and fracture in niobium.

Little information has been reported on the effect of radiation on plastic deformation in niobium, especially for single-crystal samples. Makin and Minter[28] have observed an increase in the yield stress of polycrystalline niobium by a factor of almost 2 upon neutron irradiation to 10^{20} neutrons/cm^2 ($E > 0.6$ Mev) at 16°C. Upon postirradiation annealing above 100°C, they noted a further increase in yield stress, which persisted up to about 400°C where recovery began toward the pre-irradiation value. The yield stress at room temperature for a grain size of 0.013 mm was about 42 kg/mm^2, which, in view of the results of Tottle,[29] suggests an oxygen content of about 1600 ppm. Evans, Weinberg, and Van Thyne[30] also investigated neutron-irradiation hardening in

---

[27]The preparation and characterization of samples were performed under the Research Materials Program.

[28]M. J. Makin and F. J. Minter, "The Mechanical Properties of Irradiated Niobium," Acta Met. 7, 361 (1959).

[29]C. R. Tottle, "The Physical and Mechanical Properties of Niobium," J. Inst. Metals 85, 375 (1956–57).

[30]P. R. V. Evans, A. F. Weinberg, and R. J. Van Thyne, "Irradiation Hardening in Columbium," Acta Met. 11, 143 (1963).

polycrystalline niobium of three grain sizes containing about 190 ppm O. They analyzed their results in terms of the Petch equation

$$\sigma_{YS} = \sigma_i + K_y d^{-1/2} \quad ,$$

where d is the grain diameter and σ_{YS} the yield stress, and they concluded tentatively that the increase in σ_{YS} was due chiefly to an increase in σ_i. Plastic deformation in single-crystal niobium has been studied by Mitchell, Foxall, and Hirsch[31] and by Votava[32] but not as a function of irradiation.

In this investigation, the starting stock was obtained from the Wah Chang Corporation. The manufacturer's analysis is given in Table 6.2, along with analyses obtained at our laboratory by the methods indicated. The major substitutional impurities were tantalum and tungsten. The niobium stock was given a vertical-zone, electron-beam refining treatment at a zone speed of about 4 in./hr at a pressure of 5 to 15 $\times 10^{-7}$ torr. As a measure of the overall impurity content, the ratio between resistivities at room temperature and liquid hydrogen temperature was measured as a function of distance along the zoned rod and number of zone passes. The results, shown in Fig. 6.21, indicate an increase in the resistivity ratio from 28 to 190 upon twelve zone passes. Our analyses indicate that, while the concentrations of interstitial impurities are lowered by the zone refining, the tantalum and tungsten contents are unaffected.

For the tensile tests, single crystals of single-pass niobium were grown in the zone refiner. The samples were seeded so as to produce all samples in a single orientation near the center of the stereographic

---

[31]T. E. Mitchell, R. A. Foxall, and P. B. Hirsch, "Work Hardening in Niobium Single Crystals," Phil. Mag. 8, 1895 (1963).

[32]E. Votava, "Eine Neue Methode zur Herstellung verformungsfreier Einkristall-Zugproben hochschmeltzender Metalle und einige Ergebnisse über die plastische Deformation von Niob-Einkristallen," Phys. Stat. Sol. 5, 421 (1964).

Table 6.2. Composition of Starting Material[a]

Element	Wah Chang Ingot Analysis, ppm		ORNL Analysis of 0.190-in.-diam Cold-Swaged Rod, Vacuum Annealed, ppm			
	Top	Bottom	Leco Combustion	Vacuum Fusion	Mass Spectrometer	Neutron Activity
Carbon	30	50	20			
Oxygen	110	60		48		
Nitrogen	35	55		42		
Hydrogen	4.4	4.1		3		
Aluminum	<20	<20			15	
Boron	<1	<1			0.1	
Cadmium	<5	<5			<2	
Cobalt	<10	<10			1	
Chromium	<20	<20			3	
Copper	<40	<40			30	
Iron	<50	<50			10	
Hafnium	<80	<80			15	
Magnesium	<20	<20			5	
Manganese	<20	<20			<1	
Molybdenum	<20	<20			3	
Nickel	<20	<20			5	
Lead	<20	<20			<10	
Silicon	<50	<50			30	
Tin	<10	<10			<5	
Tantalum	<500	<500				395
Titanium	<40	<40			30	
Vanadium	<20	<20			<1	
Tungsten	245	280				282
Zirconium	<100	<100			140	

[a]Wah Chang Niobium Ingot No. 31831.

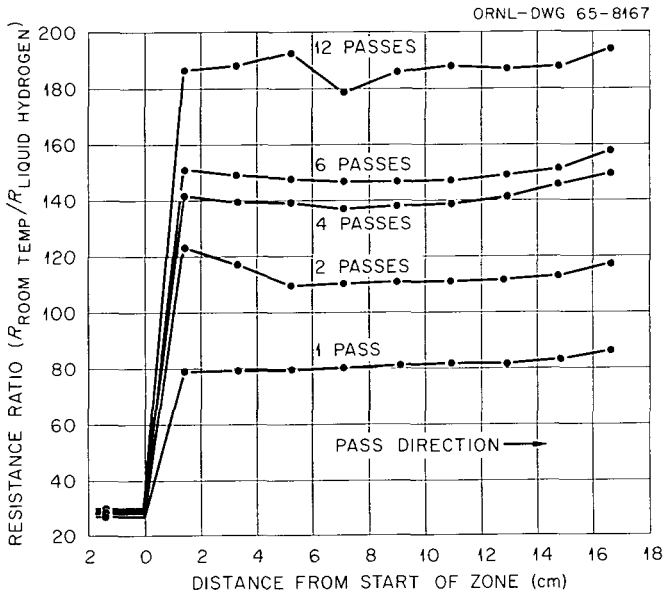

Fig. 6.21. Resistivity Ratio Along a Niobium Single-Crystal Rod as a Function of the Number of Floating Zone Passes. Source: Wah Chang Corp.; zone speed: 3.8 in./hr; diameter: 0.475 cm (nominal).

triangle where the Schmid factor, $\cos \lambda_o \cos \phi_o$ (λ_o and ϕ_o are the initial angles between the tensile axis and the slip direction and slip plane normal, respectively), has its maximum value of one-half (see Fig. 6.22). The zoned rod was centerless ground to produce a gage section 0.75 in. long and 0.085 in. in diameter with a taper of less than 0.0002 in. After the grinding, 20 mils were removed by chemical polishing, which was sufficient to eliminate all signs of cold work in the Laue back-reflection patterns. Furthermore, the uniformity of orientation was checked by traversing the sample axially in the x-ray beam and no lack of uniformity could be detected in the Laue patterns.

It is known that lattice rotation must occur in single crystals during tensile deformation, if the alignment of the samples is to be maintained in the tensile machine (see, for example, Figs. 5.12 and 5.13 of Ref. 33). In principle, the amount of rotation is given

[33]B. Chalmers, Physical Metallurgy, John Wiley & Sons, New York, 1959.

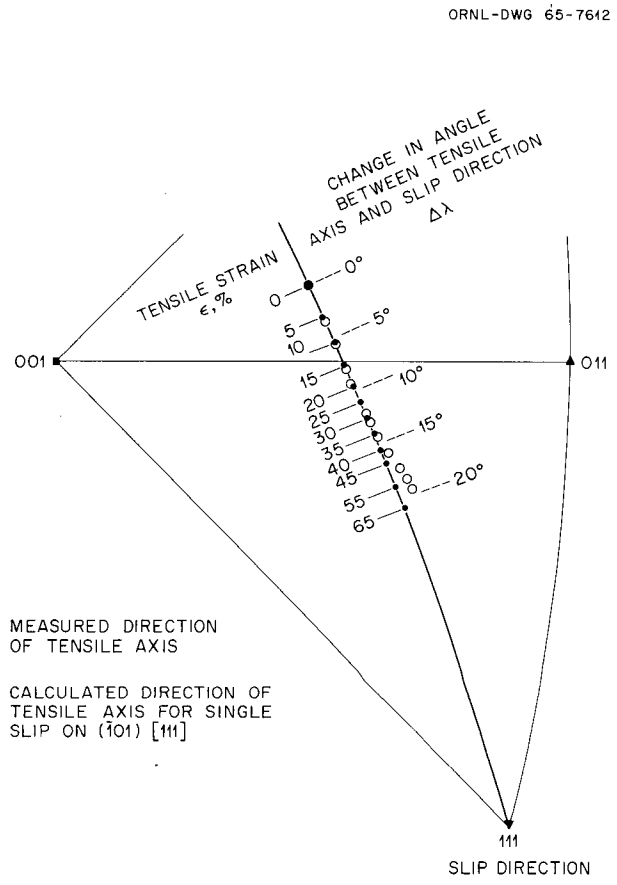

Fig. 6.22. Rotation of Tensile Axis as a Function of Deformation for a Niobium Single Crystal.

by

$$\Delta\lambda = \lambda - \lambda_o \tag{22}$$

where[34]

$$\frac{\ell}{\ell_o} = \frac{\sin \lambda_o}{\sin \lambda} \quad , \tag{23}$$

and by

$$\frac{\ell}{\ell_o} = \frac{\cos \phi_o}{\cos \phi} \quad , \tag{24}$$

[34]E. Schmid and W. Boas, Plasticity of Crystals, F. A. Hughes and Company, London, 1950.

where ℓ is the gage length during deformation, λ and ϕ are angles between the tensile axis and the slip direction and slip plane normal, respectively, and the subscript zero indicates the quantities in the initial condition before extension. Figure 6.22 shows a comparison of the orientation of the tensile axis as calculated using Eqs. (23) and (24) and as actually measured by back-reflection x-ray patterns as a function of tensile strain in 5 or 10% increments. The calculations refer to single slip on the primary system, $(\bar{1}01)[111]$, in which case the orientation of the tensile axis rotates toward [111] along a great circle containing the original orientation. It is seen in Fig. 6.22 that the observed orientation stays on this great circle until the tensile strain, $\epsilon = [(\ell - \ell_o)/\ell_o]$, reaches about 0.4. At this point, the observed tensile axis orientations (open circles) begin to depart from the calculated orientations (filled circles), indicating the onset of secondary slip on the system $(101)[\bar{1}11]$. We note also that this point is reached after a rotation of about 15°. Now, when the tensile axis has reached the horizontal 001-011 symmetry line, the resolved shear stress on the secondary system is equal to that on the primary one. The fact that the tensile axis extends so far into the 001-011-111 stereographic triangle before secondary slip starts, corresponding to overshooting of about 8° (from $\Delta\lambda \cong 7°$ to $\Delta\lambda \cong 15°$), indicates considerable latent hardening on the secondary system. In fact, one can calculate from Fig. 6.22 that the secondary slip system, $(101)[\bar{1}11]$, does not begin to operate until the resolved shear stress on it is about 13% greater than on the primary system $(\bar{1}01)[111]$.

Observations have also been made of the slip lines on the surface of a polished single crystal of niobium as a function of tensile deformation. Figures 6.23 and 6.24 show the slip lines after 65% extension on two surfaces 90° apart. The actual cross section of the sample was circular, although the sketches in Figs. 6.22 and 6.23 show a square cross section in order to better illustrate the slip geometry. The orientation of the sample was such that the projection of the tensile axis on the slip plane was in the slip direction. As is indicated in the figures, the initially circular cross section becomes elliptical,

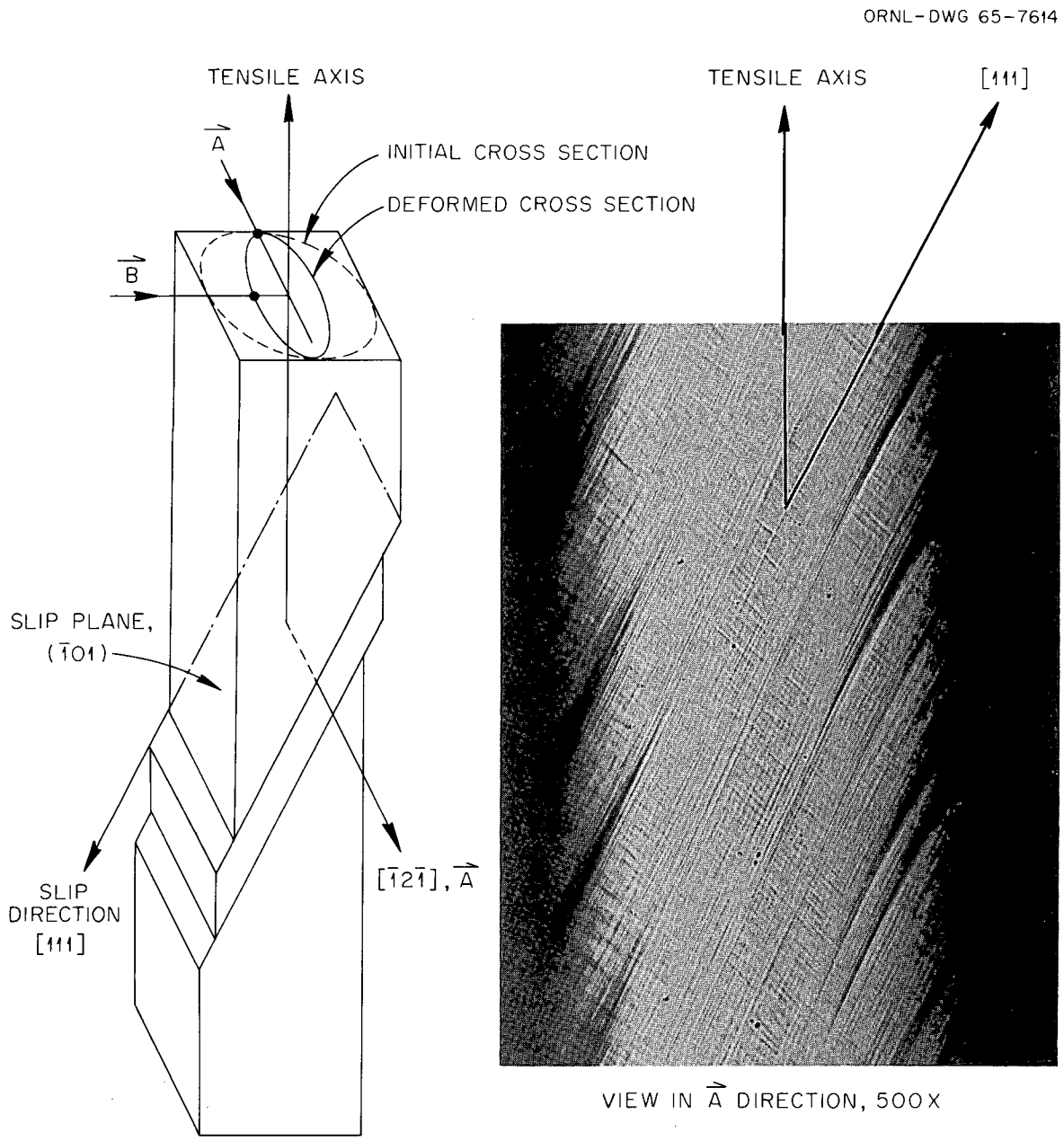

Fig. 6.23. Slip Lines in Single-Crystal Niobium after 65% Extension. Edge dislocation surface.

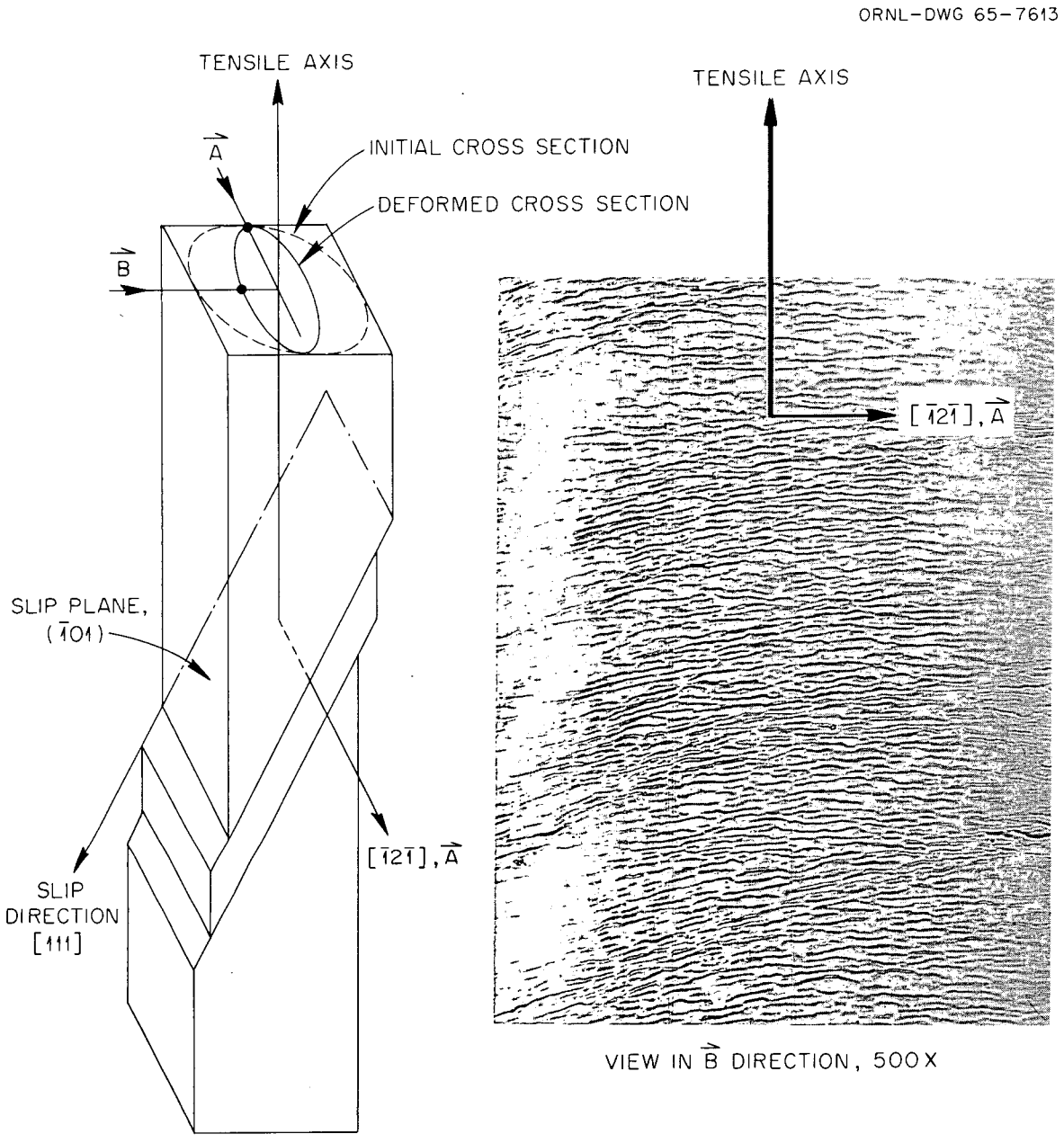

Fig. 6.24. Slip Lines in Single-Crystal Niobium after 65% Extension. Screw dislocation surface.

with the major axis of the ellipse (direction $\vec{A}$) perpendicular to the slip direction. The surface shown in Fig. 6.23 is viewed along the $\vec{A}$ direction; the surface is quite rounded in accordance with the sketch. The primary slip lines along [111] in Fig. 6.23 are probably due to the motion of edge dislocations of Burgers vector [111] which are aligned along $[\bar{1}2\bar{1}]$ and therefore emerge from the surface shown. These slip lines are quite straight. We note that the angle between the tensile axis and [111] in Fig. 6.23 is about 25°. Since the original angle was about 45°, this represents a rotation of $\Delta\lambda = 20°$ for an extension of 65%, which agrees with the rotation shown in Fig. 6.22. Some secondary slip lines are also apparent in the photomicrograph of Fig. 6.23. The secondary slip plane, (101), intersects the $(\bar{1}2\bar{1})$ plane along the $[\bar{1}01]$ direction. Therefore, the secondary slip lines (along $[\bar{1}01]$) should be perpendicular to the primary slip lines (along [111]), which is seen to be approximately the case in Fig. 6.23. Finally, the slip lines in Fig. 6.23 are spaced quite uniformly, which indicates uniform deformation and therefore uniform lattice rotation as a function of distance along the axis of the sample. This was verified by traversing the sample axially in the x-ray beam while a back-reflection Laue was being taken. The resulting Laue spots were still fairly sharp.

For the surface viewed in the perpendicular direction $\vec{B}$, Fig. 6.24 shows the wavy slip lines characteristic of the cross slip of screw dislocation which are aligned along [111]. The lines are roughly horizontal indicative of the general motion of screw dislocations in the $[\bar{1}2\bar{1}]$ direction. Since the $\vec{B}$ direction was along the minor axis of the cross section ellipse, the surface viewed in the $\vec{B}$ direction was much flatter than the one viewed along the $\vec{A}$ direction.

For our first reactor irradiation of the niobium samples, we used the Position Five Facility (PFF) in the Bulk Shielding Reactor (BSR). The PFF is a new facility and is described below. Fourteen single-crystal tensile samples, all in the orientation shown in Fig. 6.22, were irradiated inside 20-mil-thick cadmium wrappers to a dose of 3.9×10^{17} neutrons/cm^2 ($E > 1$ Mev). A dummy sample, also encased in

cadmium, was included in the irradiation assembly and thermocouples were spot-welded to it at the upper and lower shoulders and at the center of the gage length. The irradiation temperature was recorded continuously and gave a value of (135 ± 5)°C. Thermal and fast neutron detectors were also encased in cadmium wrappers and included in the assembly. The neutron dosimetry results are described below in the section dealing with the BSR-PFF, but we mention here that the spectrum was found to adhere quite closely to a fission spectrum and at a BSR power level of 1 Mw the flux of neutrons in the entire spectrum was 3×10^{12} neutrons cm^{-2} sec^{-1}. After irradiation, the cadmium wrappers were removed in the hot cells and the radioactivity of the samples was found to be low enough to permit testing in the laboratory.

At this writing, two of the irradiated tensile samples have been tested. The first of these was pulled in tension to fracture at room temperature at a crosshead speed of 0.02 cm/min. The stress-strain curves for the irradiated sample and a corresponding control sample are given in Fig. 6.25. Two types of stress-strain curves are plotted.

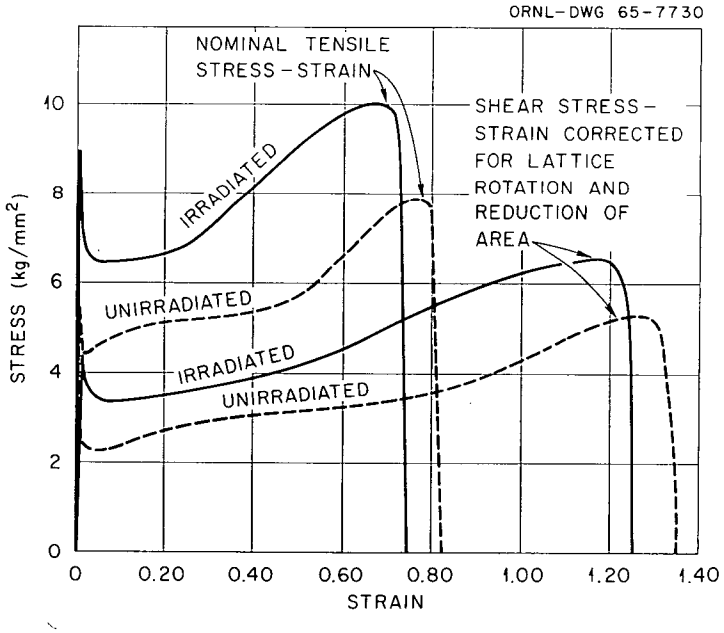

Fig. 6.25. Stress-Strain Curves for Single-Crystal Niobium, Neutron Irradiated to 3.9×10^{17} neutrons/cm^2 (E > 1 Mev) at 135°C.

The first gives the nominal tensile stress, σ, vs tensile strain, ϵ, where

$$\sigma = \frac{L}{A_o}$$

where L is the applied load and A_o is the initial cross sectional area, and

$$\epsilon = \frac{\ell - \ell_o}{\ell_o}$$

where ℓ and ℓ_o are the gage lengths during deformation and initially. The second type of stress-strain curve gives the shear stress, τ, corrected for lattice rotation and reduction in area (assuming only primary slip) vs the shear strain, γ, on the primary system. These quantities are given by[34]

$$\tau = \frac{L}{A_o} \cos \phi_o \sqrt{1 - \left(\frac{\sin \lambda_o}{\ell/\ell_o}\right)^2} \quad , \tag{25}$$

and

$$\gamma = \frac{1}{\cos \phi_o} \left[\sqrt{\left(\frac{\ell}{\ell_o}\right)^2 - \sin^2 \lambda_o} - \cos \lambda_o \right] . \tag{26}$$

As was pointed out in connection with Fig. 6.22, secondary slip starts at about $\epsilon = 0.4$, which corresponds to $\gamma = 0.7$. Therefore, the dashed τ vs γ curve is not strictly correct for shear strains greater than 0.7. We note that at $\gamma = 0.7$ or $\epsilon = 0.4$, the rate of work hardening increases perceptively for the unirradiated sample. Since Fig. 6.22 shows the onset of secondary slip at about $\epsilon = 0.4$, the increase in the apparent rate of work hardening (end of easy glide) is correlated with duplex slip.

As concerns the effect of the irradiation to 3.9×10^{17} neutrons/cm^2 ($E > 1$ Mev), the curves in Fig. 6.25 show an increase in lower yield

stress of about 50%, an increase in the magnitude of the yield drop, an increase in flow stress, and a decrease in the uniform and fracture strains. However, the irradiated sample exhibited full reduction in area at fracture (chisel-edge fracture), as was true of the control sample. The curves also suggest a decrease upon irradiation in the strain at which secondary slip starts. This will be investigated further by a study upon an irradiated sample similar to that illustrated in Fig. 6.22.

In the second test on an irradiated sample, the strain rate sensitivity at room temperature was investigated by pulling the sample alternately at crosshead speeds of 0.05 and 0.5 cm/min. The results were analyzed in terms of the inverse strain-rate sensitivity parameter, m', given by

$$m' = \frac{\partial \ln \dot{\gamma}}{\partial \ln \tau} = \frac{\ln (\dot{\gamma}_2/\dot{\gamma}_1)}{\ln (\tau_2/\tau_1)} \qquad (27)$$

where the subscripts refer to values at a given strain for the two crosshead speeds. From Eqs. (25) and (26) it may be seen that since each value of m' refers to a given strain, m' may be evaluated simply from the crosshead speeds, v_1 and v_2, and the loads, L_1 and L_2, at the strain at which the crosshead speed is changed. Hence,

$$m' = \frac{\ln (v_2/v_1)}{\ln (L_2/L_1)} \quad .$$

The results of the change-in-strain-rate tests are given in Fig. 6.26. There is some suggestion of an increase in m' upon irradiation for the lower strains, but the effect is not great. Also, the curves appear to cross near the strain value, $\tau = 0.7$, at which secondary slip starts. The rather slight effect of irradiation on m' at room temperature is perhaps not surprising, since measurements of yield and flow stresses

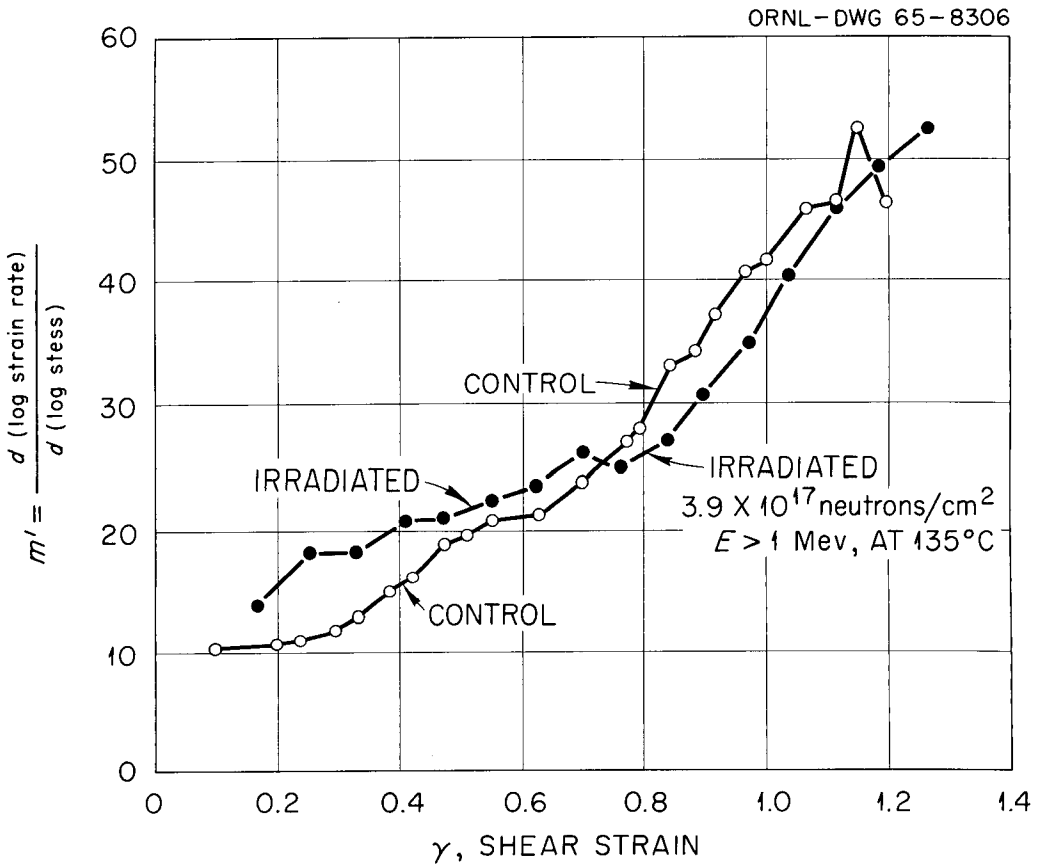

Fig. 6.26. Inverse Strain Rate Sensitivity, m′, vs Shear Strain Calculated for Single Slip for Niobium Single Crystals. Crosshead speeds: 0.05 and 0.5 cm/min; room temperature tests.

in single crystals of niobium have indicated that there is little thermal activation of slip at room temperature and above.[35]

In the immediate future our work on irradiated niobium single crystals will include tensile tests as a function of test and annealing temperatures and measurements of stress relaxation.

---

[35]T. E. Mitchell, R. A. Foxall, and P. B. Hirsch, "Work Hardening in Niobium Single Crystals," Phil. Mag. 8, 1895 (1963).

Dislocation Etch Pits in Niobium

H. D. Guberman

The efforts in this area are directed towards a more fundamental understanding of the underlying processes governing plastic deformation and fracture. It is well established that these phenomena may be best understood and interpreted in terms of the behavior of dislocations. Furthermore, an important aspect of these problems is the ability of a dislocation to move through the lattice. It is to this particular problem that we have addressed ourselves, and from the several techniques available, we have chosen an etch-pitting method to study dislocation motion.

Experimental Procedure

Material. Single crystals of niobium purified by a single pass of a molten zone in an electron-beam zone refining apparatus were used in this study. Polycrystalline samples merely experienced a single hot pass for recrystallization and outgassing. Details of the methods of fabrication, degree of purity achieved, and other properties of this material are discussed in the preceding section of this report.

Sample Fabrication. Single-crystal specimens were oriented by usual means employing Laue back-reflection x-ray patterns. They were mounted in a jig which permitted transfer of the specimen to the machining device without removal from the jig. The surfaces of interest were exposed by means of a spark-erosion process using the "Servomet Spark Machine" of Materials Research Ltd., Cambridge, England.

Briefly, the device operates in the following manner. Material is removed from the sample by a series of spark discharges of controlled energy between the sample and a tool fixture. Erosion occurs at a rate determined by the energy and frequency of the electrical discharges. In the present case, the cylindrical samples were mounted horizontally and a vertically mounted flat-surfaced tool descended past it producing a flat, reasonably smooth area on the sample. The resultant flat surface presumably is largely strain free. Laue x-ray patterns

taken immediately after the spark-erosion process showed evidence of a thin disturbed layer on the surface. Polishing away about 0.0005 in. appeared to be sufficient to remove all traces of this disturbed layer.

Polycrystalline samples were mounted and treated as ordinary metallographic specimens.

Polishing and Etching. Both electrochemical and chemical methods were tried. Electrochemical techniques, such as those suggested by Evans[36] for both polishing and etching, were found to be incapable of developing pits in this particular sample material. In every case reported here, a chemical polish followed by a chemical etch was employed.

For polishing, a solution of 70% HNO_3 (70%) and 30% HF (48%) was employed. This reacted vigorously with the sample to produce a highly lustrous surface. The length of time of application (by cotton swab) was, of course, dependent upon the nature of the starting surface, generally requiring several minutes.

Etching was accomplished by means of the etchant suggested by Bakish.[37] This consists of H_2SO_4 (95%), HNO_3 (70%), HF (48%) in the ratio 5:2:2. This too was applied with a cotton swab; however, only 15 to 60 sec were required to reveal the pits. Total immersion of the sample in either the polishing or etching medium marred the surface of interest considerably because of the vigorous reaction and attendant profuse bubble formation.

Experimental Results and Discussion

Employing the simple techniques outlined above, polycrystalline samples were found to exhibit pits of many different shapes, though within each grain the pits were identical. Many were found in arrays suggesting low-angle boundaries while others were distributed apparently at random. Pits were revealed in every case without the necessity of an aging treatment.

---

[36]P. R. V. Evans, "Dislocation Etch Pit Studies in Annealed and Deformed Polycrystalline Niobium," J. Less Common Metals 6, 253–265 (1964).

[37]R. Bakish, "On Dislocation Configurations in Rolled Columbium," Trans. AIME 212, 818 (1958).

A number of qualitative tests were performed to ensure that these pits corresponded to the sites of emergent dislocations. Briefly, the tests and results were as follows:

(a) Successive polishing to remove pits and re-etching produced identical patterns.

(b) The number of etch pits increased only a few percent as etching time was increased beyond about 20 sec. The major effect of prolonged etching was to deepen and enlarge the pits.

(c) Plastic deformation increased the number of etch pits monotonically, and furthermore, these pits were frequently arrayed in a manner suggestive of slip on single slip planes.

(d) The etchant was highly selective, producing pits only on planes of certain orientations.

Some of these points are illustrated in Fig. 6.27. In particular, the selective nature of the etchant is evident. The sample had been

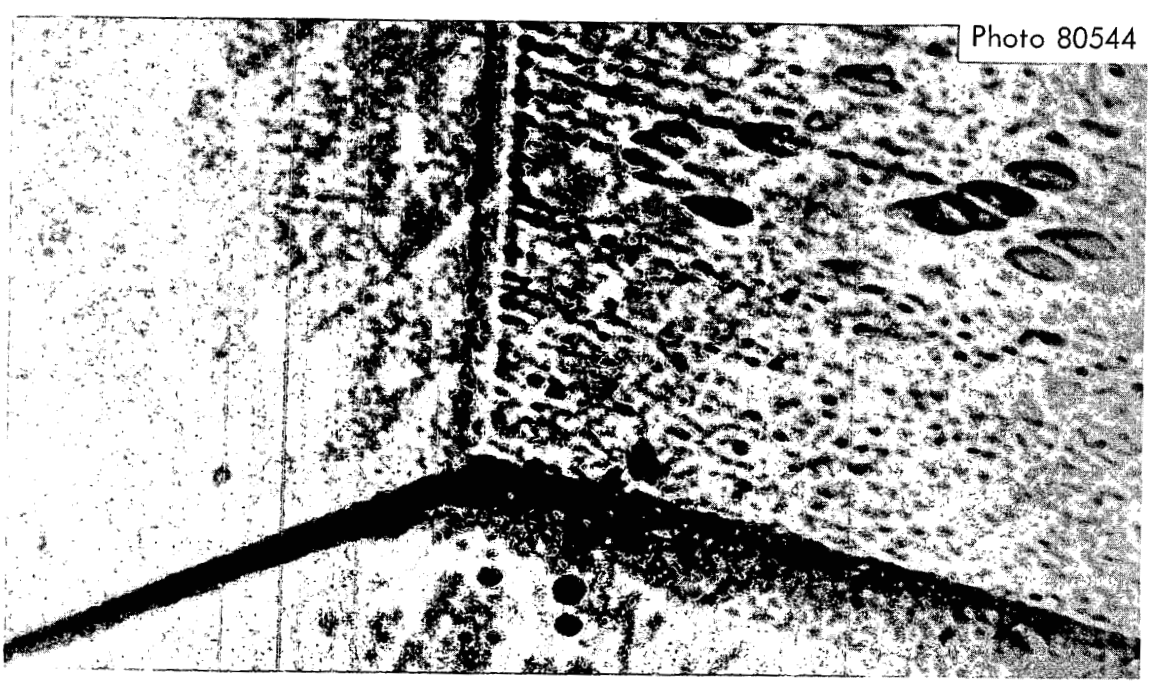

Fig. 6.27. Etch Pits in a Polycrystalline Sample of Niobium Immediately after Almost 5% Deformation in Compression. Etched for 30 sec. 680×.

deformed in compression nearly 5% and immediately etched. The particular plane observed is of an unknown orientation. Two items are of interest: first, there are straight lines of small pits, possibly emanating from the grain boundary which were not present prior to deformation; and second, the groups of much larger pits represent pits present before the deformation which had grown in size during subsequent etching.

From the above considerations, it seems reasonable to conclude that the pits do indeed represent dislocation etch pits. Furthermore, it is noteworthy that no aging or decoration of the dislocation is necessary, and that it is possible to distinguish between "old" and "new" pits successfully.

The techniques were easily extended to single crystals of niobium. Etch pits of characteristic shape were observed on (100) planes, (111) planes (Fig. 6.28), and planes close to (112) (Fig. 6.29). It is significant that planes within 1° of (112) were apparently incapable of being etched by the present techniques. It required a deliberate misorientation of at least 3° to produce pits.

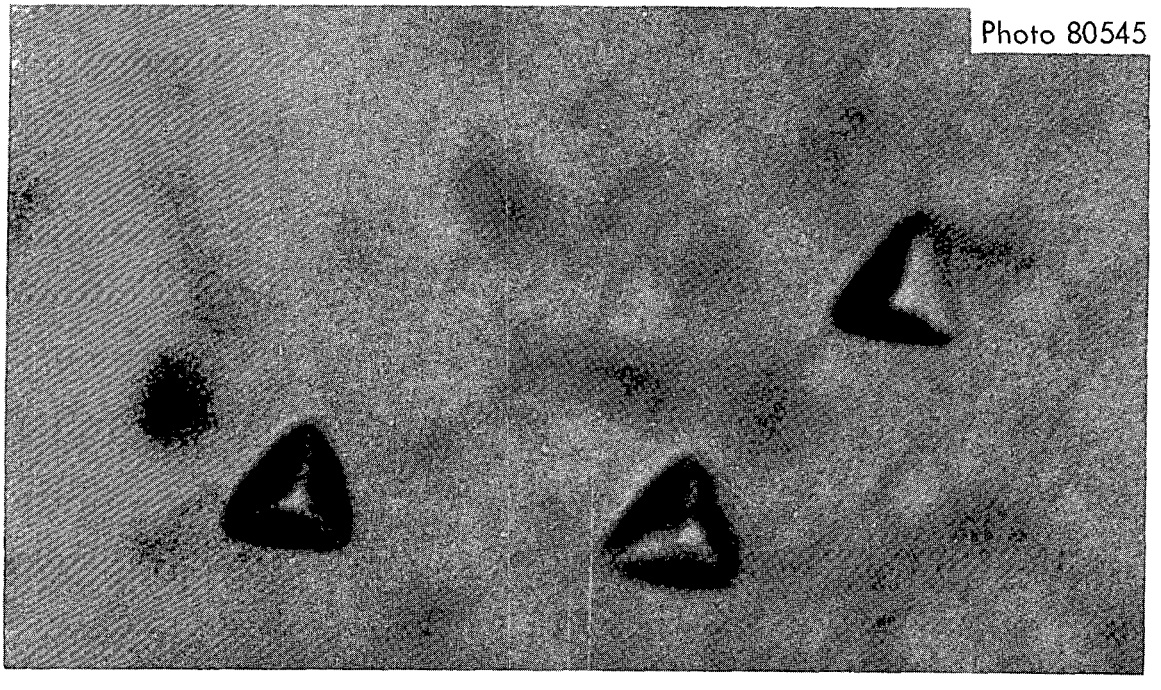

Fig. 6.28. Etch Pits on the (111) Plane of an Undeformed Single Crystal. Etched for 30 sec. 3400×.

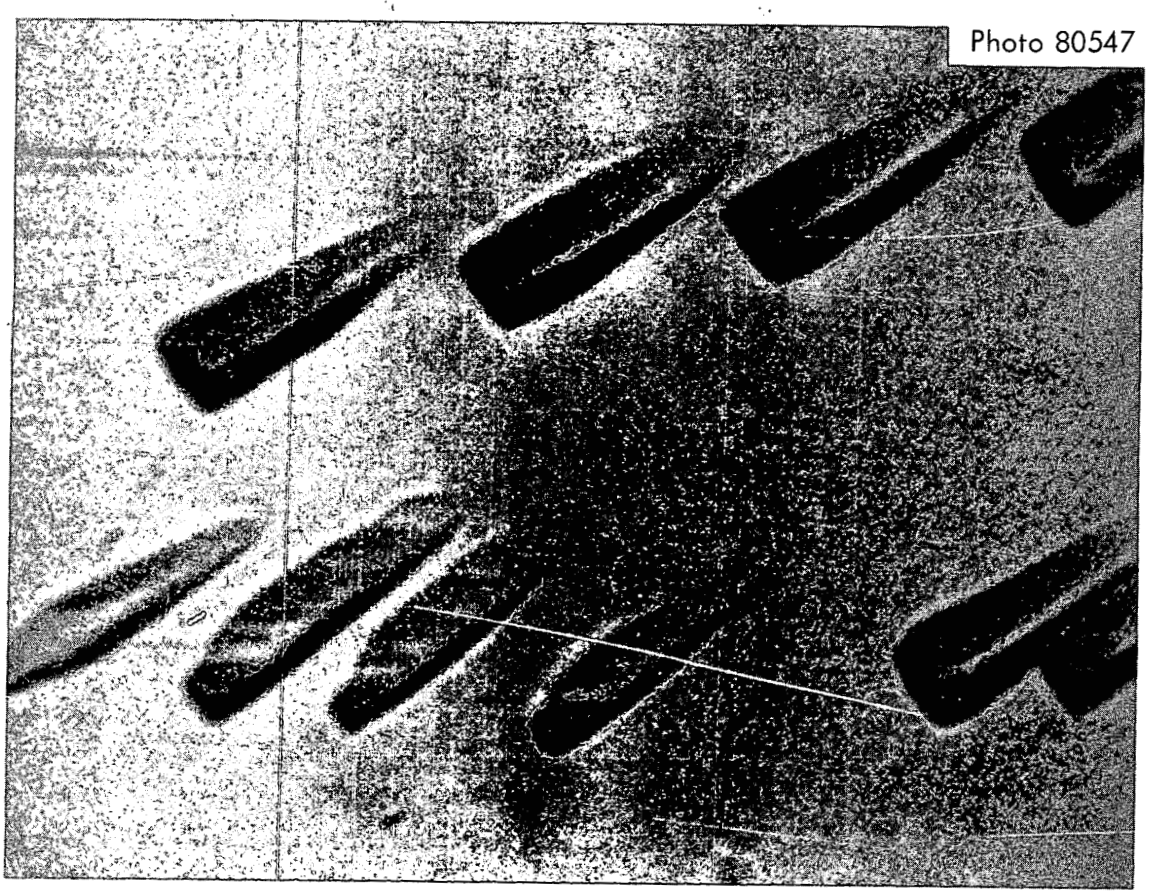

Fig. 6.29. Etch Pits Aligned in a Small Angle Boundary on a Plane Approximately 3° from the (112) Plane in an Undeformed Single Crystal. Etched 60 sec. 1700×.

The dislocations in the single-crystal samples were apparently much easier to move than in the polycrystals. Some inadvertent deformation between applications of the etchant produced the results shown in Fig. 6.30. One can easily distinguish the fresh pits in the new positions and the larger, flat-bottomed pits denoting the initial position. Figure 6.31 exhibits similar behavior on the almost-(112) plane in a crystal oriented for single glide that had been deliberately deformed by dropping from a known height.

An etch-pit count was made on an almost-(112) surface of a crystal that had not been deformed in any manner after growth. Samples from various parts of the crystal indicated that the average density lay

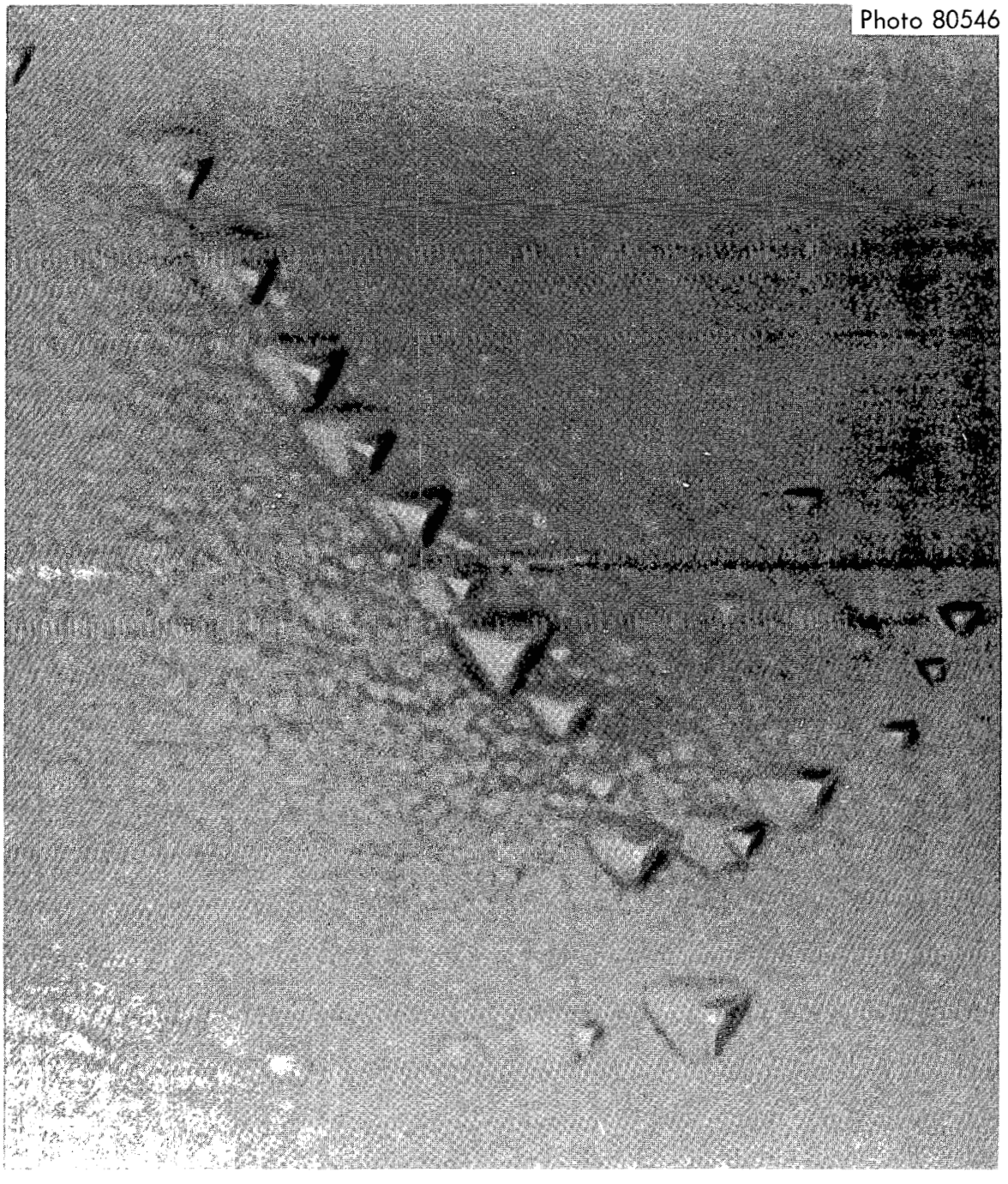

Fig. 6.30. Etch Pits on a (111) Plane in a Crystal Deformed by Handling, Exhibiting both New and Old Positions. Etched 30 sec before and 30 sec after deformation. 1700×.

Fig. 6.31. Etch Pits on a Plane Approximately 3° from a (112) Plane in a Lightly Deformed Single Crystal. The field of view is approximately the same as Fig. 6.29. Total etching time is approximately 60 sec. 1700×.

somewhere between 4 and 9 × 10^4 cm^{-2}. This is a rather low figure, if associated with the dislocation density. However, it is of approximately the same order of magnitude determined by an x-ray technique[38] for a similar crystal.

The work reported above represents the preliminaries necessary in order to study the problems of primary concern, namely dislocation mobility and the effects thereon of radiation. The method used by

---

[38]R. E. Reed, private communication.

Stein and Low[39] will be applied in this study. By this means one can determine the stress-velocity relationship for individual dislocations. In order to do this, it is necessary to introduce a surface source of dislocations in a crystal properly oriented for single glide. A given stress is then applied for a specified time and the distance traveled by the dislocations is inferred from the differences in the etch patterns before and after application of the stress. The dislocation velocity in silicon iron has been found to be an extremely sensitive function of the applied stress and presumably this may also be true for niobium. By this method it will be possible to observe the effects of radiation, temperature and other variables on the motion of dislocations in a fairly sensitive manner.

Tensile Properties of Irradiated Type 330 and 270 Nickel Alloy and Type 410 Stainless Steel

R. G. Berggren W. J. Stelzman
M. S. Wechsler

The work described in this report was initiated at the request of the High Flux Isotope Reactor Project, in connection with the possible use of nickel as a control rod material. Commercial types 330 and 270 nickel and type 410 stainless steel were used. Chemical analyses, irradiation conditions, and some tensile test results for the two heats of type 330 nickel alloy were reported previously.[40] Characterization of the type 270 nickel and type 410 stainless steel is in progress. Tensile tests have been conducted on the type 270 nickel and the type 410 stainless steel, in both unirradiated and irradiated conditions. All specimens were sheet tensile samples (1/16 in. thick, 0.180-in. gage width). Specimens were of two types: smooth tensile specimens of 3/4-in. gage length, and deeply edge-notched specimens. The specimens

[39]D. Stein and J. Low, "Mobility of Edge Dislocations in Silicon-Iron Crystals," J. Appl. Phys. 31, 362 (1960).

[40]R. G. Berggren, W. J. Stelzman, and T. N. Jones, Solid State Div. Ann. Progr. Rept. May 31, 1963, ORNL-3480, pp. 119–24.

were irradiated in a partial fuel element in the C-7 position in the Oak Ridge Research Reactor for periods of up to 1/2 year. The specimens were in contact with the reactor coolant water. The temperature of the samples was not measured directly, but heat transfer calculations indicated a maximum temperature of 100°C. Fast neutron exposures were estimated from radiochemical analyses of nickel wires irradiated with each group of specimens.

Postirradiation annealing studies have been conducted on each of the alloys. The notched sheet-tensile specimens were given single anneals at temperatures from 260 to 480°C. The smooth sheet-tensile test specimens were given isochronal annealing treatments at temperatures ranging from 200 to 500°C.

The results of tensile tests on the type 270 nickel and type 410 stainless steel are summarized in Table 6.3. Yield strengths of smooth specimens were doubled by the irradiation and total elongations were sharply reduced. All specimens deformed plastically before fracture.

Irradiated notched specimens of type 330 nickel containing 0.03% C showed 20 to 40% greater yield strengths after being annealed at 316 and 427°C than similar specimens in the as-irradiated condition (Table 6.4). Similar studies of the type 330 nickel containing 0.15% C, the type 270 nickel, and the type 410 stainless steel showed either no increase in yield strength or a marked reduction in yield strength due to the annealing treatment.

An investigation of possible anneal-hardening of irradiated smooth samples, similar to that observed for the irradiated notched type 330 nickel with 0.03% C, was conducted using an isochronal annealing treatment. Specimens of the four alloys were given a sequence of load-unload tests with 2-hr anneals in helium applied during the unload portions of the sequence. The irradiated type 330 nickel with 0.03% C exhibited an increase in flow stress after 2 hr at 300°C (Fig. 6.32), but the anneal-hardening was much less than that observed for the corresponding notched samples (Table 6.4). It is also noted in Fig. 6.32 that some recovery was observed in the

Table 6.3. Tensile Properties of Irradiated Type 270 Nickel and Type 410 Stainless Steel

Specimen Type[a]	Irradiation Dose[b] (neutrons/cm^2)	Yield Strength (psi)	Ultimate Tensile Strength (psi)	Total Elongation (%)	Number of Tests
	$\times 10^{20}$				
		Type 270 Nickel			
S	None	26,100	43,400	50	2
S	2.5	64,100	(d)	6	1
N	None	(c)	55,700	14	2
N	2.5	(c)	73,600	3	1
		Type 410 Stainless Steel			
S	None	38,000	70,000	34	2
S	2.5	82,400	(d)	0.4	2
N	None	(c)	100,000	6	1
N	2.5	(c)	115,000	3	1

[a] S indicates smooth specimens; N indicates deep edge-notched specimens.

[b] Based on the ^{58}Ni (n,p) ^{58}Co reaction, assuming σ_i = 390 mb, E_i = 2.9 Mev, and fission spectrum. Corrections were applied for ^{58}Co burnup. Values listed are for energies >1 Mev.

[c] Gage length unknown for notched specimens.

[d] Maximum load was yield point load.

Table 6.4. Annealing of Irradiated Type 330 Nickel (Edge-Notched Specimens)

Heat Number[a]	Irradiation Dose[b] (neutrons/cm^2)	Annealing Temperature[c] (°C)	Ultimate Tensile Strength (psi)
	$\times 10^{21}$		
N6906A1	1.1	None	108,000
	1.1	316	125,000
	1.1	427	152,000
	1.3	None	106,000
	1.3	427	124,000
N9185A1	1.2	None	163,000
	1.2	316	164,000
	1.2	371	161,000
	1.8	None	161,000
	1.8	427	147,000
	1.8	482	112,000

[a]Heat N6906A1 contained 0.03% C; Heat N9185A1 contained 0.15% C.

[b]Based on the ^{58}Ni (n,p) ^{58}Co reaction, assuming σ_i = 390 mb, E_i = 2.9 Mev, and fission spectrum. Corrections were applied for ^{58}Co burnup. Values listed are for energies >1 Mev.

[c]Four-hour anneal in helium.

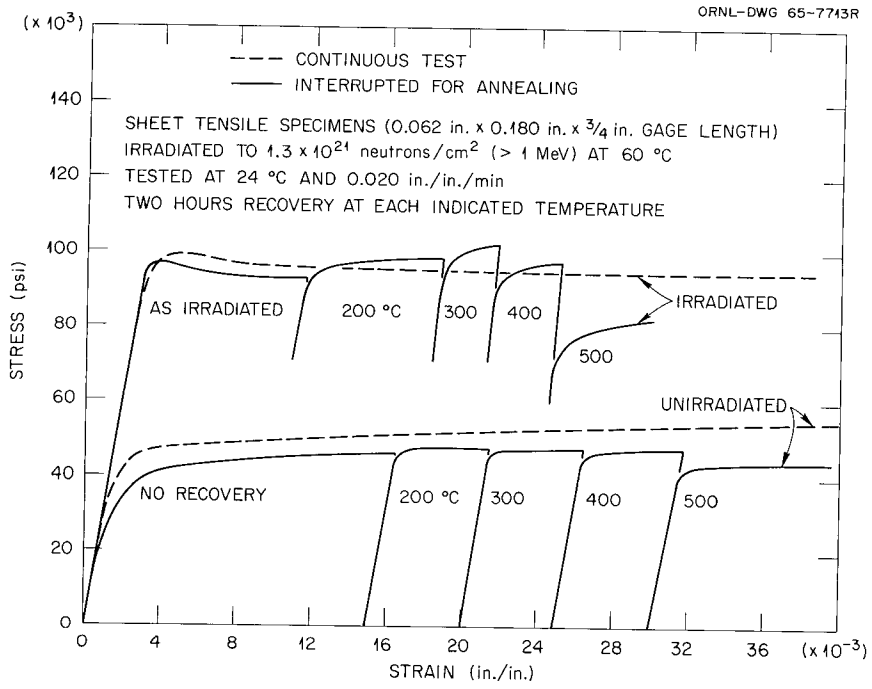

Fig. 6.32. Isochronal Annealing of Irradiated Type 330 Nickel Containing 0.03 wt % C. Smooth sheet tensile samples.

irradiated material after annealing at 400°C and considerable recovery after annealing at 500°C, whereas the unirradiated material recovered slightly (presumably due to annealing of cold work in the as-received condition) only after anneal at 500°C.

Similar isochronal annealing during the course of load-unload tests did not produce any anneal-hardening in the type 330 nickel with 0.15% C. Figure 6.33 shows that after an anneal at 400°C, the flow stress began to recover and reached almost full recovery after annealing at 500°C. The results for the type 270 nickel were quite similar to this, showing no increase in flow stress upon annealing and almost complete recovery after 2 hr at 500°C.

For the type 410 stainless steel, the recovery apparently occurred in two stages: one in the range between 200 and 350°C and a final stage at 500°C.

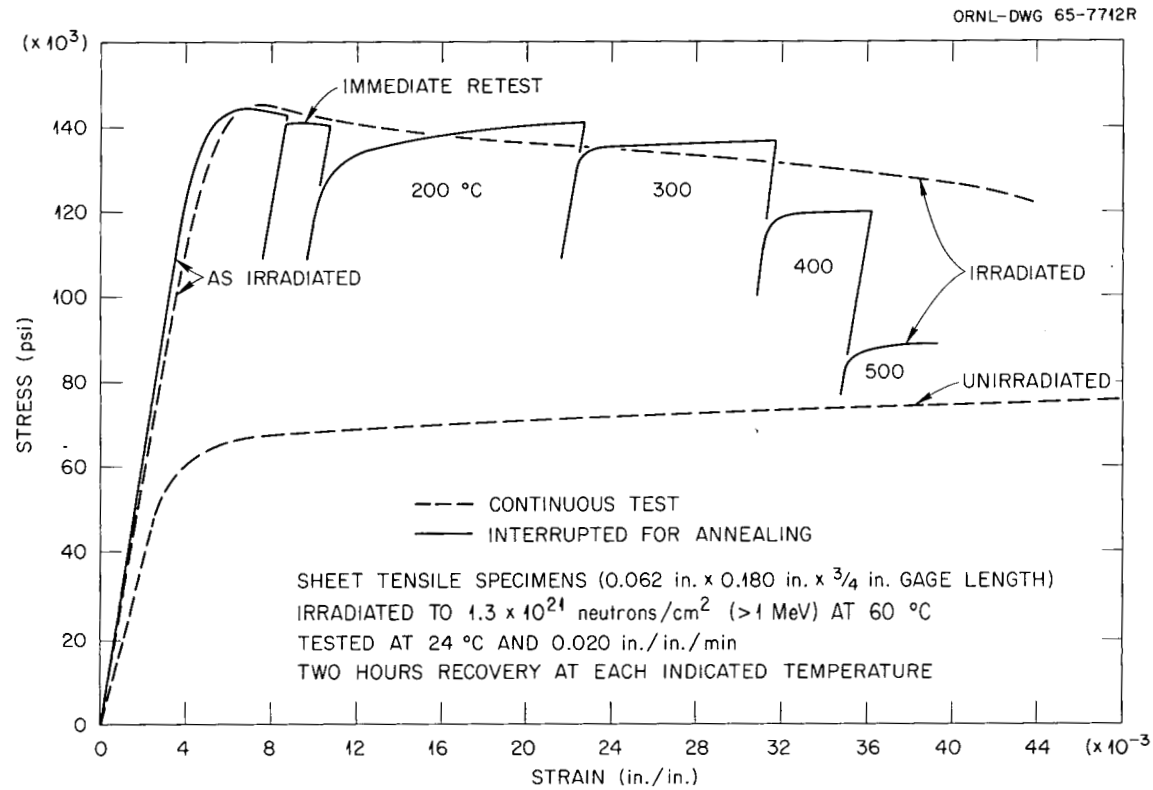

Fig. 6.33. Isochronal Annealing of Irradiated Type 330 Nickel Containing 0.15 wt % C. Smooth sheet tensile samples.

We have indicated that the notched samples of type 330 nickel with 0.03% C exhibited much greater anneal-hardening after irradiation than the smooth samples. Since the gage length for the notched samples is short, the effective strain rate is perhaps several orders of magnitude greater than for the smooth samples. To investigate the possible influence of strain rate on the anneal-hardening after irradiation, several notched samples of the 0.03% C alloy were tested at crosshead speeds one-fiftieth of those previously employed. However, no difference in the results was obtained. Also, the metallographic examination of the samples gave no clue as to the mechanism of the anneal-hardening after irradiation in this alloy.

Pressure Vessel Surveillance Program

R. G. Berggren W. J. Stelzman
T. N. Jones

EGCR Pressure Vessel Surveillance Program

The surveillance program for the Experimental Gas-Cooled Reactor has been described.[41,42] Assembly of the eight surveillance strings has been completed and trial insertions and removals from the EGCR have been attempted. Minor difficulties in removal of the strings from the reactor were experienced due to jamming in the removal cask. Modification of the strings and removal cask is under way.

SM-1 Reactor Pressure Vessel Surveillance Program

The third surveillance capsule, containing subsize Izod impact test specimens, was removed from SM-1 reactor at Fort Belvoir, Virginia, after 25.6 Mwyr of reactor operation. Prior surveillance capsules had been removed and tested after 16.4 and 20.8 Mwyr of reactor operation.[43] Impact tests and metallographic examinations have been completed. The observed increases of subsize Izod notch-impact transition temperatures for the three capsules are presented in Table 6.5. The present results for capsule 3 are in good agreement with the trends observed for capsules 1 and 2.[43] Analysis[44] of neutron flux measurements made in mockups of the SM-1 and SM-1a core and pressure vessel indicated that notch three of capsules 2 and 3 (notch four of capsule 1) were exposed to fast neutrons at a flux nearly equal to that for the pressue vessel. The nil-ductility

---

[41] R. G. Berggren, W. J. Stelzman, and T. N. Jones, Solid State Div. Ann. Progr. Rept. May 31, 1964, ORNL-3676, pp. 148–51.

[42] M. S. Wechsler et al., Solid State Div. Ann. Progr. Rept. May 31, 1965, ORNL-3841, p. 36.

[43] R. G. Berggren, L. D. Schaffer, M. S. Wechsler, and T. N. Jones, Solid State Div. Ann. Progr. Rept. Aug. 31, 1962, ORNL-3364, pp. 147–49.

[44] R. G. Berggren and L. D. Schaffer, Army Reactors Program Ann. Progr. Rept. Oct. 31, 1963, ORNL-3712 (to be published).

Table 6.5. Increases of Notch-Impact Transition Temperatures from Subsize Izod Tests on Pressure Vessel Surveillance Capsules from SM-1 Reactor

Capsule Number	Reactor Operation (Mwyr)	Notch Number[a]	ΔTT, Transition Temperature Increase, °F		
			Minimum	Maximum	Best Fit
1	16.4	1	24	36	33
		2	33	70	50
		3	51	64	58
		4	73	92	84
		5	112	124	118
		6	119	120	120
2	20.8	1	139	169	150
		2	115	143	132[b]
		3	94	101	97
		4	68	81	72
		5	51	75	64
		6	14	28	22[c]
3	25.6	1	152	152	152
		2	152	165	156
		3	118	118	118
		4	85	121	101
		5	73	104	87
		6	53	85	70

[a]Capsule 1 was loaded with notch 6 at the bottom (nearest reactor core); capsules 2 and 3 were loaded with notch 1 at the bottom (nearest reactor core).

[b]Spread of data points was greater than for control samples.

[c]One low-energy data point outside control data band.

temperature of the SM-1 reactor pressure vessel at the end of 25.6 Mwyr is 84°C (183°F), as estimated by methods previously described.[45]

Metallographic examinations of fracture profiles[41] of specimens of capsule 3 have been completed. The results of these examinations are somewhat inconclusive in that there is considerable scatter in the data and some overlap of the data for unirradiated and irradiated specimens. However, the percent cleavage failure observed in cross sections appears to correlate better with the fracture energy than the test temperature. The previously reported[41] observation that the amount of cleavage failure in a fracture in irradiated steel is very nearly that found in the unirradiated steel tested at the same temperature does not hold true for the present study.

High Flux Isotope Reactor Pressure Vessel Surveillance Program

We are also assisting in the planning and execution of a pressure vessel surveillance program for the High Flux Isotope Reactor. Preirradiation characterization Charpy V-notch impact tests of the heats of ASTM A-212, grade B, steel used in the HFIR pressure vessel have been completed.

Hot-Cell Equipment

R. G. Berggren W. J. Stelzman
T. N. Jones

The Charpy V-notch impact test machine for use in the hot cells has been modified for remote specimen handling and test temperature control. The Charpy machine and control console are shown in Fig. 6.34 during calibration and test runs. The calibration tests reported previously[46] were verified by additional tests of Army Materials Research Agency standard specimens after the modifications.

---

[45] R. G. Berggren, L. D. Schaffer, M. S. Wechsler, T. N. Jones, Army Reactors Program Ann. Progr. Rept., Oct. 31, 1962, ORNL-3386, p. 108.

[46] R. G. Berggren, W. J. Stelzman, and T. N. Jones, Fuels and Materials Development Program Quart. Progr. Rept. March 31, 1965, ORNL-TM-1100, p. 86.

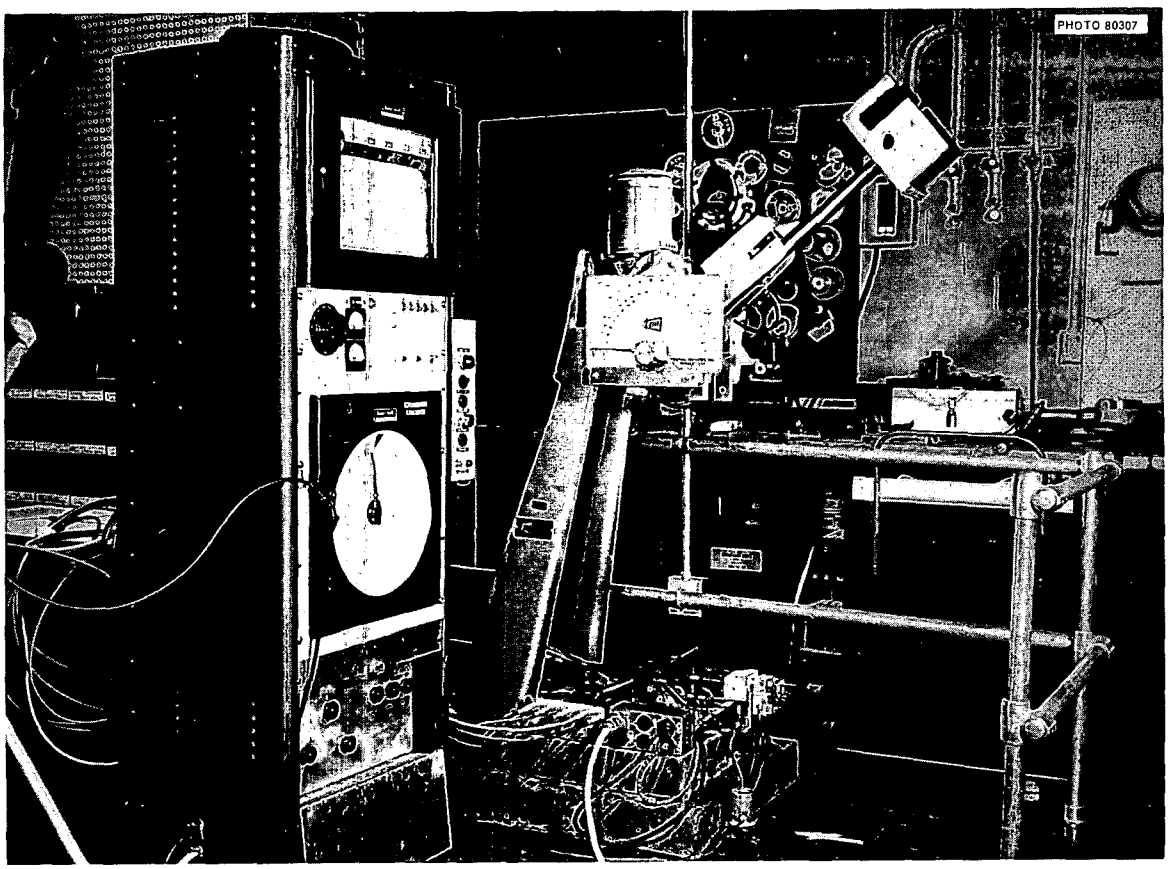

Fig. 6.34. Remote Control Charpy V-Notch Impact Test Machine and Control Console.

Test specimens are brought to test temperature in a chamber (lower right in Fig. 6.35) equipped with two carbon electrodes for resistance heating, a liquid nitrogen line for cooling, and a spring-loaded contact thermocouple for temperature measurement. The specimen is transferred from the temperature conditioning chamber to test position by a pneumatic cylinder (Fig. 6.35) and located in test position by three pneumatic cylinders (Fig. 6.36). Interlocks prevent dropping of the hammer until transfer and locating devices are retracted.

Specimen heating rates of 150°C/min. have been achieved. The contact thermocouple indicates within 1°C the true specimen temperature for heating rates up to 90°C/min. A specimen can be taken from room temperature to 250°C in 3 min. During cooling with liquid nitrogen,

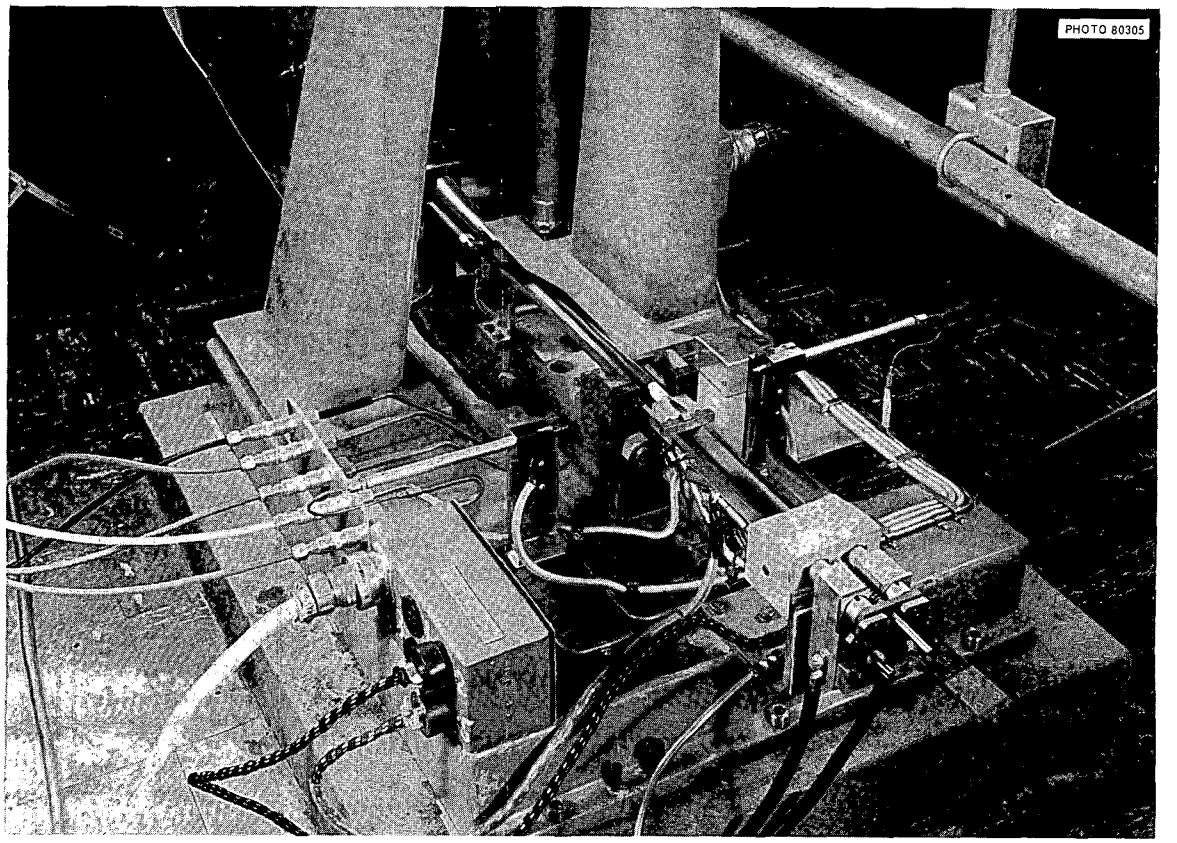

Fig. 6.35. Specimen Conditioning and Transfer Modification of Charpy V-Notch Impact Test Machine.

nitrogen is vaporized before reaching the specimen chamber for specimen temperatures down to about −150°C. Cooling rates of 20 to 30°C/min are achieved. Contact thermocouple errors of 4°C have been observed at maximum cooling rates. Normal operating procedure specifies holding the specimen at desired test temperature for 1 min for tests below room temperature and specifies heating rates for tests above room temperature. Under these conditions, contact thermocouple errors are less than 1°C for specimen temperatures from −180°C to +260°C. Below −180°C thermocouple error approaches 5°C. The maximum test temperature of 260°C is governed by the resilient materials used to support the contact thermocouple.

Elapsed time for transfer of test specimens from the conditioning chamber to the anvil, positioning, and testing is consistently less

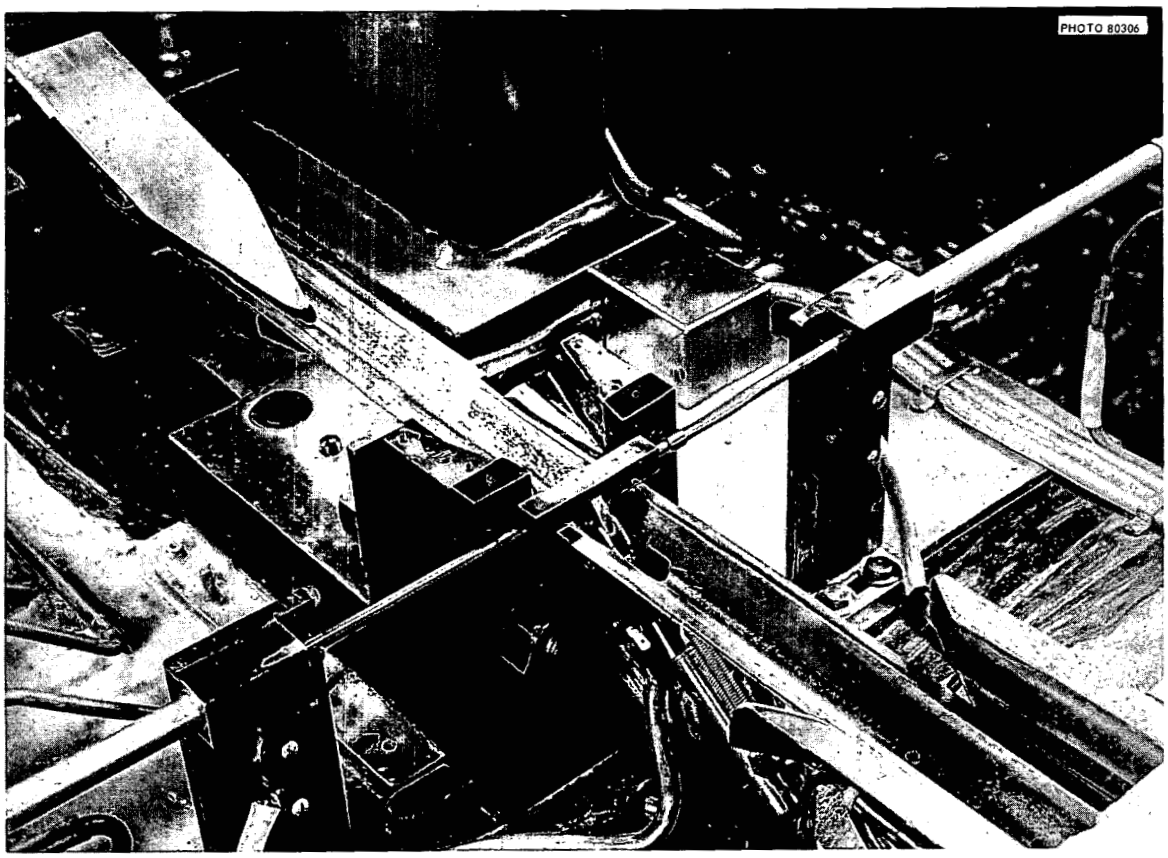

Fig. 6.36. Specimen Positioning on Remote Control Charpy V-Notch Impact Test Machine.

than 3 sec. Temperature measurements during specimen transfer, positioning, and testing demonstrate that, for our normal operating procedure, test temperature is known within 1°C for elapsed times up to 5 sec for temperatures from 260°C to about −100°C. Compensation for heat up is required below −100°C. The possible error in test temperature at −180°C is 4°C.

The Position Five Facility in the Bulk Shielding Reactor

J. M. Williams W. E. Brundage
B. C. Kelley M. S. Wechsler

The ORNL Bulk Shielding Reactor consists of an assembly of MTR-type fuel elements. It is suspended in a pool of water, 40 ft long, 20 ft wide, and 20 ft deep, which acts as the reactor coolant, moderator, shield, and reflector. At present, the maximum power is 1 Mw, although plans are under way to increase the power level to 2 Mw and to provide 24-hr-a-day operation. The current core loading is illustrated in Fig. 6.37.

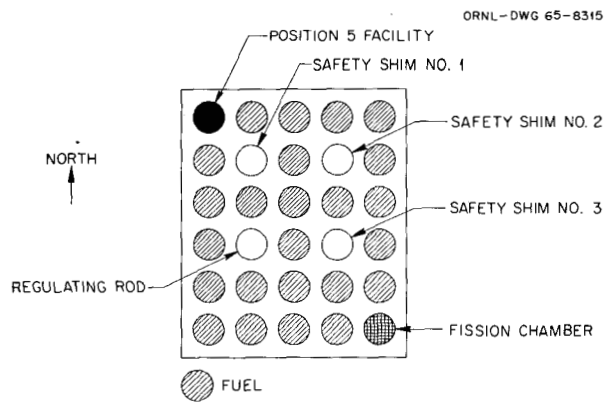

Fig. 6.37. Core Loading of the Bulk Shielding Reactor.

A new facility, the Position Five Facility, has been installed at the BSR to provide an irradiation chamber useful for radiation experiments on materials. As shown in Fig. 6.37, the facility is located at the northwest corner of the reactor. It consists of a curved access tube, 4 in. in outer diameter, which is welded to a hollow core piece having the same outside dimensions as a BSR fuel element, roughly a 3-in.-square cylinder, 2 ft long (Figs. 6.38 and 6.39). The top of the tube is sealed with a plug, which has incorporated in it a port for pressurizing the system and several electrical feed-throughs. There is a neutron and gamma shield plug suspended from the seal plug. A sidearm is also provided for evacuating the system. A lead ballast, sheathed in aluminum,

PHOTO 80372A

Fig. 6.38. Photograph of the BSR Pool Showing the Reactor Core and the Position Five Facility.

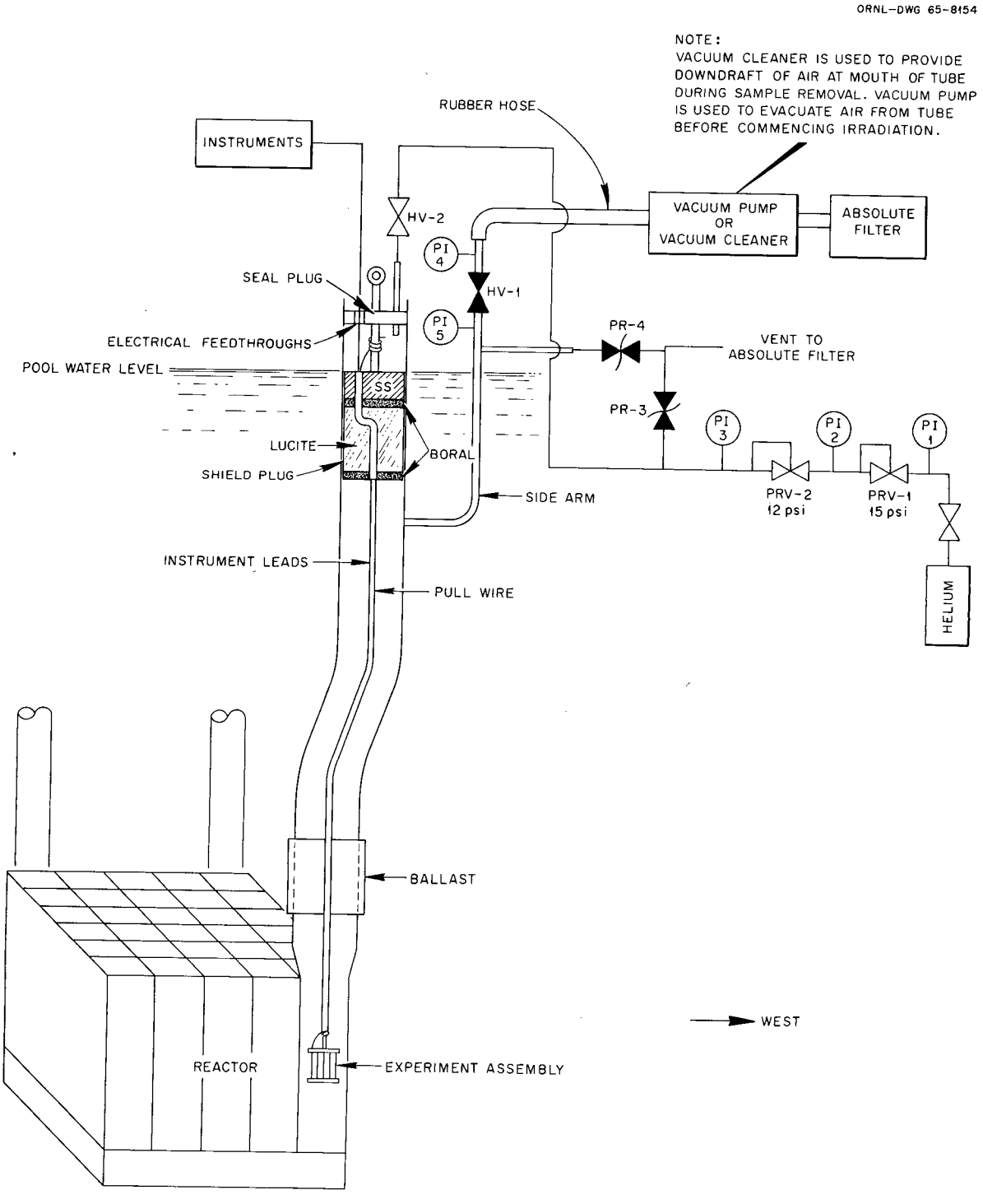

Fig. 6.39. Schematic Drawing of the Position Five Facility.

surrounds the tube near the bottom end to compensate for buoyancy. As can be seen in Fig. 6.38, the top of the tube projects above the surface of the water. A large transfer cask has been constructed that may be lowered around the top end of the tube and into which the irradiated sample assemblies may be removed.

In a preliminary experiment, the gamma heating in the PFF was measured. An aluminum block containing wells for an internal heater and thermocouples was lowered into the tube. The block was prevented from making intimate contact with the inside wall of the tube by set-off rings of Nichrome wire. The total mass of the assembly approximated that of a typical experiment. With the heater power off, the temperature of the block was measured as a function of reactor power. At full power, it reached 150°C. Then, with the reactor off, the electrical power to the internal heater necessary to raise the temperature to 150°C was determined. In this way, the gamma heating at full power was found to be about 0.1 w/g.

The neutron flux in the PFF was measured in conjunction with the irradiation of niobium single-crystal tensile samples described by R. E. Reed and M. S. Wechsler, "Plastic Deformation in Niobium Single Crystals," p. 98 in this chapter. Cobalt in the form of aluminum-cobalt wires was used to measure the thermal flux, and the fast flux was measured by the threshold detectors, ^{237}Np, ^{238}U, ^{58}Ni, and ^{54}Fe. All of the flux monitors were surrounded by 20 mils of cadmium, as was true for the niobium samples. However, the flux monitors were removed after 11.2 hr, whereas the niobium samples were exposed intermittently for 47.65 hr. The monitors and samples were placed at the horizontal midplane of the BSR.

The results of the fast flux measurements are given in Fig. 6.40. The circled points give the integral neutron fluxes above energy E_i calculated from the equation[47]

$$\Phi(E_i) = \frac{A_s}{N_o \sigma_i} \quad , \tag{27}$$

[47]Proposed Tentative Method for Measuring Neutron Flux by Radioactivation Techniques, E 261-T, 1966 Book of ASTM Standards, Part 31, American Society for Testing and Materials, Philadelphia, Pa.

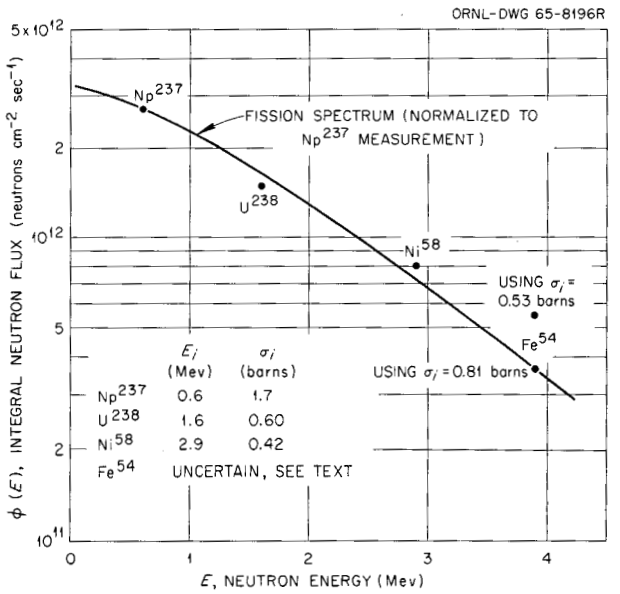

Fig. 6.40. Observed Integral Neutron Fluxes at the Center of the BSR-PFF with the BSR at 1 Mw. The fission spectrum is shown for comparison.

where A_s is the saturated activity,[48] N_o is the original number of detector atoms, and σ_i is the threshold cross section corresponding to the threshold energy E_i. The fission spectrum curve is also plotted. The form used was[47]

$$\Phi_f(E) = A(aE)^{1/2} \exp(-aE) \quad , \tag{28}$$

where $a = 0.775$ Mev^{-1} and A was adjusted to fit the data point for the ^{237}Np monitor. With the use of the values of E_i and σ_i shown in the legend in Fig. 6.40 (which were taken from Ref. 47), the data points for uranium and nickel agree to within about 10% with the fission spectrum.

The data point for iron presents a special problem, since E_i and σ_i for ^{54}Fe are not well established. We have chosen to set E_i for ^{54}Fe as the median energy for the weighted yield curve, $\sigma(E)f_f(E)$, where $\sigma(E)$ is the cross section of the $^{54}Fe(n,p)^{54}Mn$ reaction as a function of energy

[48]We are indebted to W. Harvey and W. T. Mullins for the activity measurements.

and $f_f(E)$ is the normalized fission spectrum obtained by setting $A = 2a/\sqrt{\pi}$ in Eq. (28). Thus, E_i is the energy such that

$$\int_0^{E_i} \sigma(E) f_f(E) dE = \int_{E_i}^{\infty} \sigma(E) f_f(E) dE \qquad (29)$$

and therefore represents the energy for which as many activations occur for neutrons above E_i as below. For $\sigma(E)$ we have used the curve given in Fig. 1 of Ref. 49. The resultant weighted yield curve is shown in Fig. 6.41, which gives a value of E_i from Eq. (29) of 3.9 Mev. Now, if the fission-average cross section $\overline{\sigma}^f = 0.060$ barns given by Passell[50] for ^{54}Fe is used, then from

$$\sigma_i = \frac{\overline{\sigma}^f}{\int_{E_i}^{\infty} f_f(E) dE} , \qquad (30)$$

where $E_i = 3.9$ Mev, we find $\sigma_i = 0.53$ barns. If this value of σ_i is used, the calculated integral flux above 3.9 Mev is about 58% greater than that predicted by the fission spectrum (Fig. 6.40). It is interesting, however, that if the fission-average cross section is calculated directly from Fig. 6.41, the value $\overline{\sigma}^f = 0.091$ barns is obtained, which leads to $\sigma_i = 0.81$ barns, and as shown in Fig. 6.40, this produces good agreement with the fission spectrum.

It can be seen in Fig. 6.37 that one of the three safety shim control rods (shim No. 1) is located diagonally adjacent to the PFF. The question arises as to whether the neutron flux in the PFF is very

---

[49] Proposed Tentative Method for Measuring Fast-Neutron Flux by Radioactivation of Iron, E 263-T, 1966 Book of ASTM Standards, Part 31, American Society for Testing and Materials, Philadelphia, Pa.

[50] T. O. Passell, "The Use of Ni^{58} and Fe^{54} as Integrators of Fast Neutron Flux," p. 501 in Neutron Dosimetry, Proceedings of the Symposium on Neutron Detection, Dosimetry, and Standardization Vol. 1, International Atomic Energy Agency, Vienna, 1963.

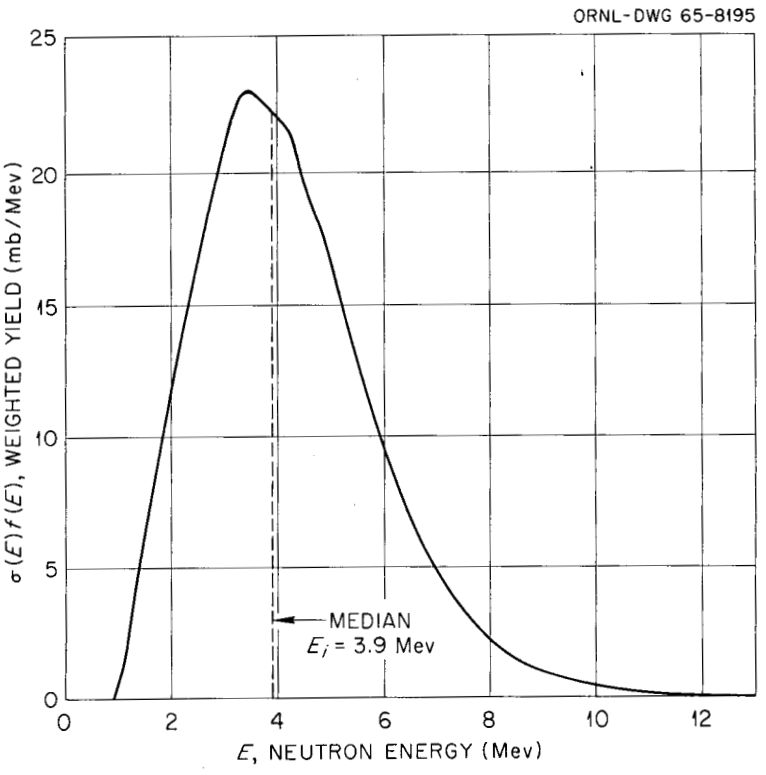

Fig. 6.41. The Weighted Yield Curve for $^{54}Fe(n,p)^{54}Mn$, Based on Cross Section Curve in Ref. 49 and a Fission Spectrum.

sensitive to the position of this control rod. Therefore, a survey was made of the thermal flux (using cobalt monitors) and fast flux above 2.9 Mev (using nickel monitors) as a function of vertical distance in the sample tube for several positions of this control rod. The reactor power level, as indicated by a fission chamber at the south side of the core, was kept constant at 0.1 Mw by adjusting the other control rods and the results were scaled up to 1 Mw. The flux profiles shown in Fig. 6.42 indicate that if shim No. 1 is lowered from 22 to 16 in. from the bottom of the reactor, a change in flux of only a few percent results. For comparison, the operating range of this control rod for the niobium irradiation described above was from 16.8 to 19.0 in. However, if shim No. 1 is dropped to a position 10 in. from the bottom of the reactor, the flux may be decreased as much as 10%. Figure 6.42 also indicates that in the region of the flux peak the flux is uniform to within 10% over a span of 7 or 8 in.

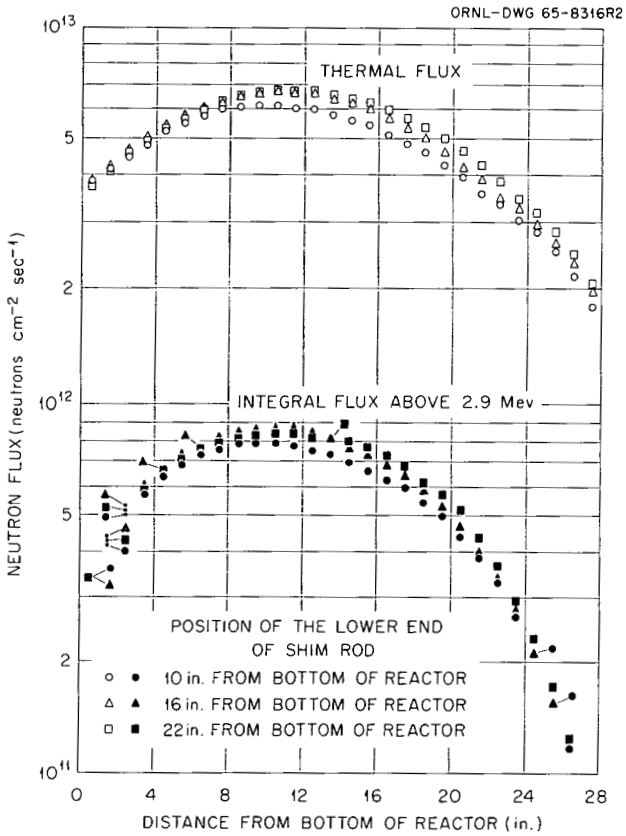

Fig. 6.42. Neutron Flux Profiles in BSR-PFF for Various Positions of No. 1 Shim Rod. The fluxes refer to power level of 1 Mw, as scaled up from measurements at 0.1 Mw.

Criticality Safety Tests on the Converter Facility for the Bulk Shielding Reactor

W. E. Brundage E. B. Johnson[51]

The preliminary design for the Bulk Shielding Reactor Converter Facility has been previously described.[52,53] The facility will use leakage neutrons from one face of the BSR, thermalized by passage through D_2O, to produce fission in a cylindrical sleeve containing ^{235}U surrounding the samples.

---

[51]Neutron Physics Division.

[52]W. E. Brundage, Fuels and Materials Development Program Quart. Progr. Rept. Mar. 31, 1965, ORNL-TM-1100, p. 87.

[53]G. H. Llewellyn, Design Analysis of a Pure Fission Spectrum Facility for the BSR, ORNL-TM-987 (January 1965).

Since the system represented a potential criticality hazard, a test on a mockup was performed at the Critical Experiments Facility. Briefly, the converter will consist of an aluminum-clad 0.25-in.-thick, 3.758-in.-OD, 12-in.-high cylindrical sleeve of U(93% enriched in ^{235}U)-Al alloy lined on the inner surface with 0.060-in.-thick (50% Cd–50% Mg) alloy. The center of the facility, which will receive irradiation samples, will normally be filled with either air or helium. The outside wall of the converter sleeve will be cooled by an annulus of light water circulated through a heat exchanger. This assembly, centered in an air- or helium-filled cavity 7.5 in. in radius and 24 in. high, will, in turn, be centered in a 28- × 15-in. aluminum tank 24 in. deep containing D_2O; light pool water will be adjacent to one side and will cover the top and the bottom of this tank. The entire assembly will be adjacent to another 12-in.-thick, 28-in.-wide, 24-in.-deep D_2O filled tank on one face of the BSR. Because of metallurgical and heat transfer considerations, the converter sleeve cannot contain more than 1.5 kg of uranium.

In order to determine whether a possible criticality hazard would exist under accident conditions (i.e., should the converter sleeve and its surrounding and enclosed "voids" be flooded with either H_2O or D_2O), a mockup was made from available materials and tested for criticality. Four 3-in.-wide, 10-in.-long, and 1/8-in.-thick pieces of U(93.4% enriched in ^{235}U) metal (density = 18.7 g/cm^3) were fastened to the outer surface of a square aluminum tube 3 × 3 in. in outside dimensions with 0.047-in.-thick walls. The assembly contained 4.32 kg of ^{235}U. This assembly was placed in the center of a 30-in.-diam tank and flooded with H_2O and with D_2O in turn. Little source neutron multiplication was observed in either case.

The assembly was then placed in the center of a 13.75-in.-diam cylinder containing D_2O which was reflected with effectively infinitely thick water. Again little neutron multiplication was observed.

Since the assembly contained 2.9 times as much ^{235}U as can be present in the irradiation facility postulated for use with the BSR, it is concluded that the latter can not become critical under reasonable accident conditions.

Previous reports in this series are:

ORNL-TM-920	Period Ending June 30, 1964
ORNL-TM-960	Period Ending September 30, 1964
ORNL-TM-1000	Period Ending December 31, 1964
ORNL-TM-1100	Period Ending March 31, 1965
ORNL-TM-1200	Period Ending June 30, 1965

Internal Distribution

1–3. Central Research Library
4–5. ORNL – Y-12 Technical Library Document Reference Section
6–15. Laboratory Records
16. Laboratory Records, RC
17. ORNL Patent Office
18. G. M. Adamson, Jr.
19. J. C. Banter
20. J. H. Barrett
21. S. E. Beall
22. R. J. Beaver
23. M. Bender
24. R. G. Berggren
25. J. O. Betterton, Jr.
26. D. S. Billington
27. A. L. Boch
28. B. S. Borie
29. G. E. Boyd
30. W. H. Bridges
31. R. B. Briggs
32. W. E. Brundage
33. R. M. Carroll
34. J. V. Cathcart
35. G. W. Clark
36. K. V. Cook
37. J. H. Crawford
38. J. E. Cunningham
39. J. H. DeVan
40. C. V. Dodd
41. D. A. Douglas, Jr.
42. J. I. Federer
43. B. E. Foster
44. A. P. Fraas
45. J. H Frye, Jr.
46. R. J. Gray
47. W. R. Grimes
48. H. D. Guberman
49. J. P. Hammond
50. W. O. Harms
51. R. L. Heestand
52–53. M. R. Hill
54. N. E. Hinkle
55. H. W. Hoffman
56. H. Inouye
57. T. N. Jones
58. G. W. Keilholtz
59. B. C. Kelley
60. J. A. Lane
61. C. F. Leitten, Jr.
62. A. L. Lotts
63. R. N. Lyon
64. H. G. MacPherson
65. R. E. MacPherson
66. M. M. Martin
67. W. R. Martin
68. D. I. Matkin
69. R. W. McClung
70. H. E. McCoy, Jr.
71. H. C. McCurdy
72. R. E. McDonald
73. D. L. McElroy
74. C. J. McHargue
75. F. R. McQuilkin
76. A. J. Miller
77. E. C. Miller
78. F. H. Neill
79. S. M. Ohr
80. M. F. Osborne
81. P. Patriarca
82. F. H. Patterson
83. A. M. Perry
84. S. Peterson
85. M. L. Picklesimer
86. P. L. Rittenhouse
87. W. C. Robinson
88. M. W. Rosenthal
89. G. Samuels
90. H. W. Savage
91. J. L. Scott
92. O. Sisman
93. G. M. Slaughter
94. G. P. Smith, Jr.
95. S. D. Snyder
96. I. Spiewak
97. J. T. Stanley
98. W. J. Stelzman
99. J. O. Stiegler
100. A. Taboada
101. D. B. Trauger
102. J. T. Venard
103. G. M. Watson
104. M. S. Wechsler
105. A. M. Weinberg
106. J. R. Weir, Jr.

107. W. J. Werner
108. G. D. Whitman
109. J. M. Williams
110. R. O. Williams
111. J. C. Wilson
112. H. L. Yakel, Jr.
113. F. W. Young, Jr.
114. C. S. Yust

External Distribution

115–117. F. W. Albaugh, GE, Hanford
118. A. J. Alexander, AEC, CANEL
119. R. J. Allio, Westinghouse Atomic Power Division
120. R. D. Baker, Los Alamos Scientific Laboratory
121. L. Brewer, University of California, Berkeley
122. V. P. Calkins, GE, NMPO
123. W. Cashin, Knolls Atomic Power Laboratory
124. S. Christopher, Combustion Engineering, Inc.
125. R. M. Cilimberg, Division of Reactor Development, AEC, Washington
126–127. D. F. Cope, AEC, Oak Ridge Operations
128. G. K. Dicker, Division of Reactor Development, AEC, Washington
129. E. A. Evans, GE, Vallecitos
130. W. C. Francis, Phillips Petroleum Company
131. R. G. Grove, Mound Laboratory
132. D. H. Gurinsky, BNL
133. S. Hasko, NBS
134. A. N. Holden, GE, APED
135. J. S. Kane, University of California, Livermore
136. J. H. Kittel, ANL
137. E. J. Kreih, Westinghouse, Bettis Atomic Power Laboratory
138. W. L. Larsen, Iowa State University, Ames Laboratory
139. J. H. MacMillan, Babcock and Wilcox Company
140. R. E. Pahler, Division of Reactor Development, AEC, Washington
141. S. Paprocki, BMI
142. D. Ragone, GA
143. L. M. Raring, Pratt & Whitney, CANEL
144. Division of Research and Development, AEC, ORO
145. A. H. Roberson, U. S. Department of the Interior, Bureau of Mines
146. W. Rostokev, Illinois Institute of Technology Research Institute
147. F. C. Schwenk, Division of Reactor Development, AEC, Washington
148–149. J. M. Simmons, Division of Reactor Development, AEC, Washington
150. L. E. Steele, Naval Research Laboratory
151. R. H. Steele, Division of Reactor Development, AEC, Washington
152. W. F. Sheely, Division of Research, AEC, Washington

153. A. Strasser, United Nuclear Corporation
154. W. R. Voigt, Division of Reactor Development, AEC, Washington
155. C. E. Weber, Atomics International
156. G. W. Wensch, Division of Reactor Development, AEC, Washington
157. M. J. Whitman, Division of Reactor Development, AEC, Washington
158–172. Division of Technical Information Extension